Failure Modeling in an Orthotropic

Plastic Material Model

under Static and Impact Loading

by

Shyamsunder Loukham

A Dissertation Presented in Partial Fulfillment
of the Requirements for the Degree
Doctor of Philosophy

Approved October 2020 by the
Graduate Supervisory Committee:

Subramaniam Rajan, Chair
Narayanan Neithalath
Barzin Mobasher
Christian Hoover
Yongming Liu

ARIZONA STATE UNIVERSITY

December 2020

ABSTRACT

An orthotropic elasto-plastic damage material model (OEPDMM) suitable for impact analysis of composite materials has been developed through a joint research project funded by the Federal Aviation Administration (FAA) and the National Aeronautics and Space Administration (NASA). The developed material model has been implemented into LS-DYNA®, a commercial finite element program. The material model is modular comprising of deformation, damage and failure sub-models. The deformation sub-model captures the rate and/or temperature dependent elastic and inelastic behavior via a visco-elastic-plastic formulation. The damage sub-model predicts the reduction in the elastic stiffness of the material. The failure sub-model predicts when there is no more load carrying capacity in the finite element and erosion of the element from the finite element model. Most of the input parameters required to drive OEPDMM are in the form of tabulated data. The deformation sub-model is driven by a set of tabulated stress-strain data for a given strain-rate and temperature combination. The damage sub-model is driven by tabulated damage parameter-strain data. Two failure sub-models have been implemented – Puck Failure Model and Generalized Tabulated Failure Model. Puck Failure Model requires scalar parameters as input whereas, the Generalized Tabulated Failure Model is driven by a set of equivalent failure strain tabulated data. The work presented here focuses on the enhancements made to OEPDMM with emphasis on the background, development, and implementation of the failure sub-models. OEPDMM is verified and validated using a carbon/epoxy fiber reinforced composite. Two validation tests are used to evaluate the failure sub-model implementation - a stacked-ply test carried out at room temperature under quasi-static tensile and compressive loadings, and

several high-speed impact tests where there is significant damage and material failure of

the impacted panel. Results indicate that developed procedures provide the analyst with a

reasonable and systematic approach to building predictive impact simulation models.

DEDICATION

This work is dedicated to my family and friends.

TABLE OF CONTENTS

LIST OF TABLES

LIST OF FIGURES

1 INTRODUCTION

Over the last few decades, composites have gained wide popularity especially in the automotive and the aerospace industries due to their high strength to weight ratio. In an aircraft, composites are used in tail structures or fuselages to reduce the weight leading to fuel savings. In the case of automobiles, fiber reinforced composites are increasingly being used since they provide multiple advantages over conventional materials – lighter energy absorbing components leading to better fuel efficiency and lower exhaust emissions. In military applications and law enforcements, woven composite fabrics are used in bullet "resistant" vests. In medical applications, thermoplastic and thermoset composites are used as components in MRI scanner, wheelchairs, surgical target tools, orthotic foot inset, and many other devices and products (AZO Materials, 2015). Composites offer several advantages such as design flexibility, resistance to corrosion, and lower maintenance cost. Despite these attractive features, the use of composites has been limited. There are several reasons – structural composites used in high-performance products have a short history, the behavior is complex and the tools available to characterize the behavior either experimentally or numerically are not as mature as those available for competing materials such as metals, and there exists an education gap since most engineers are perhaps not familiar with the knowledge to investigate and use structural composites. One of the primary needs of a design engineer working with composite materials, especially in the aerospace or automotive industry, is the ability to create and execute large finite element models that yield acceptable results in a reasonable amount of time (Shyamsunder et al., 2020a). A designer wishes to have a

predictive tool which would require a smaller number of input parameters and be able to accurately predict the behavior of the composite under a wide variety of loading scenarios such as static, dynamic and impact loadings. For example, in the case of an aircraft engine containment design, a rotor burst or a blade-out scenario is one of several events that are routinely simulated. Building a model to simulate this event requires high-quality experimental data that provides data for the material model and a detailed but efficient finite element model that can predict the response accurately, robustly and efficiently. To meet this growing need, US government agencies have embarked on several long-term research plans. Development of advanced computational analysis methods is an important aspect of the NASA Advanced Composites Project (ACP) which was created with the goal of reducing the development and certification timeline for new composite structures used in aeronautics applications (Melis et al., 2018). Developing a good predictive tool with all these complexities requires putting together multiple components. First is the need for a general constitutive model that is suitable for different composite types and architectures. Second is the requirement for an explicit dynamics finite element program which is versatile and has capabilities for modeling impact events with features to model contact, damage, failure, and stochastic variations. Third is the necessity to have a laboratory-based material characterization process to generate material/structural properties for the constitutive model, and a laboratory setup capable of conducting high energy impacts to create validation data. The advances in hardware and software over the past few years have helped move towards meeting these requirements. However, the process of building an efficient, robust, accurate and reliable predictive tool remains a research challenge. The first and the second components of an explicit

dynamics finite-element based predictive tool can be seen in Figure 1. The green block

contains the constitutive model. The primary focus of this dissertation is on this block -

the development of a constitutive model for static and impact loading scenarios to predict

deformation, damage, and failure of composites. Deformation, damage, and failure are

the basic sub-components of a predictive constitutive model. While these three terms are

intertwined, the most vexing question is to define "failure".
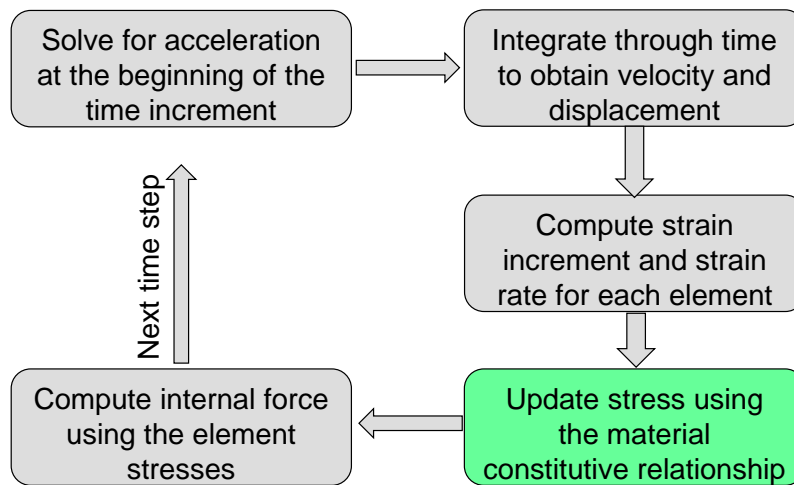
Figure 1. Algorithm in a Typical Explicit Finite Element Analysis

A review of published material on composite modeling shows that it is difficult to

precisely define what failure is. Hinton (2011) provides one definition - "'Failure is the

point beyond which the structure or component ceases to fulfil its function." This

definition is rather difficult to use from a modeling viewpoint. In the context of this

dissertation, the term *failure onset* implies the instant at which there is no further increase

in the load carrying capacity exhibited by the finite element (FE), and the term *erosion*

refers to the deletion of the finite element from further FE calculations. Christensen &

Lonkar (2016) ask a rather provocative but fundamental question - "Is it possible to develop and derive a rational and general failure criterion composed only of basic and standard strength properties of the material and completely devoid of adjustable parameters and/or unjustified assumptions? Essentially this question asks if it is possible to pursue materials failure as a scientific investigation as opposed to a parameters exercise." On top of the complexity involved in accurately simulating the deformation and damage response of composites, predicting the failure is a big challenge in the context of a structural analysis (Shyamsunder et al., 2020a). Some of the earlier research work done in predicting the deformation, damage, and failure of composites are discussed in the next section.

1.1 Background and Prior Art

The continuum mechanics approaches to developing constitutive models for composites can be categorized into the following groups (Vaziri et al., 1991) – (a) nonlinear elasticity theories, e.g. (Petit & Waddoups, 1969), (b) damage theories coupled with elasticity, e.g. (Allen et al., 1987; Chen & Hwang, 2009; Wu & Yao, 2010; Xiao, 2009), (c) classical incremental plasticity theories, e.g. (Griffin et al., 1981; Sun & Chen, 1989; Vaziri et al., 1991), and (d) endochronic plasticity theory, e.g. (Pindera & Herakovich, 1983). Of these approaches, the incremental plasticity theory has the most promising features for static and impact analyses. Griffin et al. (1981) use Hill's orthotropic yield criterion and incremental plastic flow theory to solve for the structural response under mechanical and thermal loading. One of the earliest and accurate plasticity-based material models for composites was developed by Sun & Chen (1989) with a focus on unidirectional, carbon

fiber-based composites under in-plane loading conditions. Later in 1991, Vaziri et al. (1991) developed a rate-independent, plasticity model for fiber reinforced composites (FRC). The model could predict elastic and plastic response of structural systems modeled as a plane stress problem. Other modeling approaches have been developed for a well-defined class of problems such as short-fiber reinforced composites (Notta-Cuvier et al., 2014) or ceramic matrix composites (Rajan et al., 2014). Models can also be created at different length scales to understand the deformation, damage, and failure behavior of composites. For example, in Boutaous et al. (2006), an elastoplastic damage model is developed to model the behavior of laminated composites up until fracture. Damage for each elementary constituent is accounted for at the micro level and a complete model at the meso-scale is obtained by applying a homogenization method such that the model can be implemented in a finite element program. This approach, while attractive to understand the constituent behavior of composites, will require far too much computational effort to model impact problems aside from other limitations in the framework (Hoffarth et al., 2016).

Researchers have defined and examined various measures of material and structural failures associated with composites that are easier to use and can be integrated into a simulation framework (Shyamsunder et al., 2020a). For example, composites fail in compression in a variety of ways – fiber crushing, splitting, elastic microbuckling, matrix failure and plastic microbuckling, buckle delamination, and shear-band formation (Jelf & Fleck, 1992). Knass & Gonzalez (2001) describes composite failures as involving fracture of the material that is brought about by fiber breakage, fiber micro-buckling,

fiber pullout, matrix cracking, delamination, debonding or any combination of these mechanisms. Even one of the simplest composite architectures – a unidirectional laminate composite, poses rather unique challenges. Typically, experiments are conducted at the lamina level to characterize the behavior of the composite. A predictive failure theory must first accurately predict the failure of the lamina under a uniaxial state of static stress. This must be followed by the ability of the failure theory to predict the failure of a laminate that is made up of several lamina at different orientations, first under simple loading conditions and then under a complex three-dimension state of stress. A study of six failure criteria (Sun et al., 1996) shows that at the lamina level the criteria that incorporate separate fiber-based failure modes and matrix based failure modes produce the most accurate results, and as a result the failure criteria that yields the most accurate predictions for multi-ply laminates varies depending on whether the laminate layup and loading is fiber-dominated or matrix-dominated. Camanho (2002) discusses the subject of failure criteria for fiber-reinforced polymer composites and summarizes that the confidence levels of the failure theories used need to be improved and that there is no consensus in the industry on the most adequate failure criterion. A similar sentiment is echoed by Kaddour & Hinton (2012) where they state, "The designers, wishing to use the models benchmarked in World-Wide Failure Exercise-II (WWFE-II), can only expect a few theories to give acceptable correlation (within ±50%) with test data for 75% of the test cases used."

World-Wide Failure Exercises (WWFE), which started in 1991, provide a fascinating look at the evolution of some of the most widely recognized failure theories. In WWFE-I

(1996-2004), 19 theoretical approaches for predicting deformation and failure in 14 test cases have been studied (Hinton et al., 2004). In WWFE-II (2007-2013), 12 groups (involving 12 failure theories) have taken part in predicting the response of 12 test cases (Kaddour & Hinton, 2012). WWFE-III involves 12 methods for modeling damage and failure of 13 test cases (Kaddour et al., 2013; Kaddour & Hinton, 2018). A list of the more popular failure theories is presented next. The purpose of listing these theories is not to present a detailed summary (those can be found in other publications), but to illustrate the fact that there are numerous competing models where the failure definitions are extremely varied. It should be noted that the first three theories have been implemented in commercial finite element codes, a very desirable and attractive feature. The rest have been implemented into in-house codes written in a variety of languages (FORTRAN, MathCad, Visual Basic, Matlab etc.).

Tsai-Ha's Theory (Huang et al., 2012a, 2012b): The model is based on 3D laminate theory and is tied to the use of commercial finite element programs (MD NASTRAN and ABAQUS) via user-supplied subroutines. The failure model is based on micromechanics of failure (MMF) and considers failure in the fiber, matrix, and the fiber-matrix interface. A progressive damage model is used for the matrix. Thermal stresses are also considered in the model.

Pinho's Theory (Pinho et al., 2012, 2013): The model is implemented in a finite element program. The underlying constitutive model is tailored to capture the nonlinear behavior of unidirectional composites. A nonlinear response is considered in shear, and in the

transverse and through-thickness directions. Matrix failure, fiber kinking and fiber tensile failure are handled separately. Fracture energy is used with each failure mode.

Puck's Theory (Deuschle & Kropline, 2012; Deuschle & Puck, 2012): The model is implemented in ABAQUS via a user-supplied subroutine. The failure criteria for fiber fracture and inter-fiber fracture of unidirectional fiber-reinforced polymer composites are suitably modified forms of the Coulomb-Mohr theory of fracture. More details of this theory are presented later in this dissertation.

Huang's Theory (Zhou & Huang, 2012a, 2012b): The model is based on 3D laminate theory and the Bridging Model. The Bridging Model, a micromechanical theory, is modified and applied to laminates. Using the constituent properties as the material data, the model can predict the elastic-plastic behavior of a unidirectional (UD) composite and compute the stresses in the constituent materials. Final failure of the laminate takes place when fiber failure occurs, or the resin has failed in compression. The lamina is assumed to fail if any of its constituents fail, and subsequently the stiffness of the resin is reduced.

Carrere's Theory (Carrere et al., 2012a, 2012b): This is a multi-scale Micromechanical-based Hybrid Mesoscopic (MHM) progressive failure model. The model considers the effect of microdamage on the ply strength parameters. This involves the determination of microdamage in the UD ply using a damage law which is based on continuum damage mechanics. Nonlinear behavior is taken care of by a thermo-viscoelastic constitutive law. The failure criterion at the ply level depends on the effective strength which is a function

of the microdamage and considers fiber-fracture (FF) and inter-fiber fracture (IFF) as modes of failure. The model distinguishes between tension and compression failures. The failure in each mode is then followed by the degradation of the failed ply based on a damage law.

Bogetti's Theory (Bogetti et al., 2012a, 2012b): A laminate theory is used to compute the effective laminate stress-strain response. Nonlinear behavior as well as progressive ply failure are accounted for in the model. The failure theory is based on computing and using the maximum 3D strain. The ply strains are used in nine modes of failure that are connected to strain values in the principal material directions. This is the only model that showed all the failure envelopes to be closed in WWFE-II.

Cuntze's Theory (Cuntze, 2012a, 2012b): The model assumes that the composite at the ply level is transversely isotropic. The failure model is based on the author's Failure Mode Concept and considers five modes of failure – two FF modes and three IFF modes. Furthermore, the interaction of all the modes are considered using a probabilistic based series spring model where the interaction exponent is obtained by curve fitting of experimental data.

Wolfe's Theory (Zand et al., 2012; Doudican et al., 2012): The model assumes that each lamina is an inelastic homogenous orthotropic material. Failure is based on a strain-energy formulation that incorporates the effects of in-plane thermal residual stresses accumulated during the curing of composite laminates and considers the failure of matrix

9

and fiber separately. The failure criterion is described by the ratio of strain energy acquired to the strain energy at failure. The stiffness of the lamina is reduced once the failure criterion in the lamina is satisfied. It should be noted that the test cases which have been used in exercising the eight failure models listed above for WWFE-II, involve only static loading scenarios.

As stated earlier, modeling impact problems presents its own unique challenges (Bhatnagar, 2016; Chen, 2016; Melis et al., 2018; Roberts et al., 2002). Some of these examples include impact simulations of aircraft engine containment systems involving aluminum target and titanium impactor (Ambur et al., 2001), and steel projectile impacting Kevlar dry fabric targets (Stahlecker et al., 2009). Two issues are brought to light in these examples. First, the challenge is to conduct these impact tests in a reliable manner. Some of these include (a) obtaining the velocity as well as the orientation of the impactor as a function of time, (b) using Digital Image Correlation (DIC) hardware and software to obtain the full displacement field that can then be used obtain surface strains, and (c) obtaining rate data (stress-strain curve) from coupon testing using equipment such as Split Hopkinson Bar and DIC. Second, simulating the impact event is a challenge where modeling issues are compounded when used with sophisticated material models that have numerous input parameters all of which cannot be obtained from experiments. Usually these parameters are obtained through numerical calibration, a tedious process that must then be valid for a variety of impact scenarios.

1.2   Current State of Material Models for Composites in LS-DYNA

LS-DYNA® (Ansys-LST, 2020b) is an advanced multi-physics simulation software program which is widely used by the automotive and the aerospace industries for modeling impact events such as vehicle crashworthiness analysis and engine bird strike. Over the past few years, various constitutive/material models for composites have been developed and implemented in LS-DYNA® (Ansys-LST, 2020b). This section discusses some of the commonly used material models used for modeling composites to highlight the required capabilities and the difficulties in obtaining the capabilities.

MAT022 also known as MAT_COMPOSITE_DAMAGE, is an orthotropic material model made for fiber-reinforced laminated composites (Ansys-LST, 2018; Chang & Chang, 1987a, 1987b). The model has two components – deformation and damage. The stress-strain in the material is computed using finite element method based on classical laminate theory. MAT022 considers failure onset in three modes - matrix cracking, fiber-matrix and fiber breakage. If the matrix failure onset criterion is satisfied, the transverse properties are set to zero, and the longitudinal properties are left unaltered. The longitudinal properties are degraded using a Weibull distribution only if either fiber/matrix shearing or fiber breakage takes place. No element erosion can be modeled using MAT022. Another simple composite model is MAT023 or MAT_TEMPERATURE_DEPENDENT_ORTHOTROPIC (Ansys-LST, 2018). It supports orthotropic elastic materials that have temperature dependent properties. The moduli, Poisson's ratios and the coefficients of thermal expansion can be defined for

11

different temperature values in the input deck. These two material models are very simple but perhaps, not suitable for modeling highly non-linear material behavior.

MAT054 and MAT055 (Chang & Chang, 1987a, 1987b) are enhanced versions of MAT022. These two material models are collectively known as MAT_ENHANCED_COMPOSITE_DAMAGE and share the same set of input cards (Ansys-LST, 2018). MAT055 uses Tsai-Wu failure criterion (Tsai & Wu, 1971) for matrix instead of the Chang criterion. These models provide the ability to erode a badly distorted element if the time step falls below a specified value. The erosion of elements creates crashfront elements (which are the elements that share nodes with the eroded elements). The material strength for the crashfront elements can be reduced with a user input parameter. In addition, these models take the in-plane strength quantities as input to drive the progressive damage model as well as account for a rate sensitive composite. The strain rates can be smoothened using a running average technique thus helping avoid sudden change in rates during the simulation. Erosion (failure) in MAT054 is triggered when the effective strain and the transverse shear strain exceed specified values. In the case of solid elements, element erosion can take place due to maximum strain criteria in the matrix in tension, compression, or shear component. Element erosion can also take place due to maximum strain criteria in the tensile and compressive mode in the fiber. For shell elements, element erosion takes place when all the through thickness integration points have satisfied the aforementioned criteria. MAT054 also has parameters to keep the stress constant at a minimum limit after the peak stress has been reached.

MAT058 also known as MAT_LAMINATED_COMPOSITE_FABRIC (Ansys-LST, 2018) is a material model suitable for woven fabrics. This is also used to model composites which are unidirectional laminated composites. This model is based on progressive failure analysis which uses Hashin's failure criteria (Hashin, 1980) for unidirectional composites and a modified failure criterion for woven fabrics. MAT058 has a smooth damage evolution law which is not the case with MAT054 and MAT055. MAT058 has been implemented only for thin and thick shells. Similar to some of the other material models, it can take the moduli as tabulated input as a function of strain rates. MAT058 takes the strength in-plane strength quantities as well as the corresponding strain as input to predict the failure onset. These strengths and the strain parameters can also be defined as functions of strain rate. Strain rate averaging options are available with this model. MAT058 also has a feature to keep the stress constant at a minimum limit after the peak stress (residual strength). Element layers (integration points) can be eroded when the effective strain reaches a specified value which can be defined as a function of strain rate. Elements can also be eroded if the time step falls below a specified value. The erosion of elements creates crashfront elements, the stiffness of which can be reduced by a factor which is an input to MAT058. Non-linear shear behavior can also be modeled using MAT058. MAT158 or MAT_RATE_SENSITIVE_COMPOSITE_FABRIC is the same as MAT058 except that MAT158 is rate sensitive via viscoelastic stress terms. This material is also suitable for modeling unidirectional composites and woven fabrics and has been implemented for shell and thick shells.

MAT059 also known as MAT_COMPOSITE_FAILRUE_SHELL_MODEL, MAT_COMPOSITE_FAILRUE_SOLID_MODEL or MAT_COMPOSITE_FAILRUE_SPH_MODEL (Ansys-LST, 2018) depending on the element type used for modeling, uses either a faceted failure surface or an ellipsoidal failure surface depending on the type of composite to be modeled. Similar to MAT054, the crash front algorithm and the minimum stress limit factor (residual strength) features are available with this model. It has been reported that for lower energy (5 J) impact test cases where the damage is matrix dominated (Rossi et al., 2020), MAT022, MAT54, MAT055, MAT058, MAT059 performs poorly since these models do not consider delamination mode of failure.

MAT116 or MAT_COMPOSITE_LAYUP, MAT117 or MAT_COMPOSITE_MATRIX and MAT118 or MAT_COMPOSITE_DIRECT (Ansys-LST, 2018) are used for modeling elastic responses of composites using shell elements. These material models are based on standard composite lay-up theory. These models are used for the computation of extensional, bending and coupling stiffness components, and stresses are not computed. MAT116 is very efficient for large number of layers. MAT116 is not suitable for foam core or sandwich composites. The only difference between MAT117 and MAT118 is that MAT117 gives the stiffness coefficients in the material coordinate system and MAT118 gives the stiffness coefficients in the element coordinate system.

MAT161 or MAT_COMPOSITE_MSC (Ansys-LST, 2018) is used for progressive failure analysis of unidirectional composites and woven fabrics using solid elements. For

14

a unidirectional composite, the material model considers three fiber failure modes – fiber tension/shear failure, fiber compression and fiber crush failure mode. Two modes of matrix failure are considered- plane parallel to the ply (delamination mode) and the second one where the failure plane is perpendicular to the ply layer (transverse mode) (Matzenmiller et al., 1995; Yen, 2002). MAT162 is based on continuum damage mechanics approach for fiber-reinforced composites. A nonlocal averaging feature is available in the strain-based failure criterion. The non-local averaging technique is useful in the case of modeling damage and failure using non-structured mesh. MAT161 and MAT162 can be used for both solids and shell elements. These models are suitable for studying delamination behavior of composites.

MAT219 also known as MAT_CODAM2 (Ansys-LST, 2018) is a continuum damage mechanics model which is a sub-laminate-based approach for fiber reinforced composites. The model assumes that there is transverse isotropy in the lamina. The non-local averaging feature is available for this model to improve the prediction of damage and crack pattern. This model can be improved (Forghani, 2011) by coupling a plasticity model to it to predict the permanent deformation of a composite. Another improvement which can be made with the model is the capability to predict the delamination behavior.

MAT221 or MAT_ORTHOTROPIC_SIMPLIFIED (Ansys-LST, 2018) is an orthotropic material model having the same elastic model as that of MAT022 for solid elements. The model uses nine damage variables to degrade the material properties distinguishing

between tension and compression. The erosion can be triggered using strain values specified for the material directions.

MAT261 and MAT262 (Ansys-LST, 2018) are continuum damage models which uses Puck's failure criterion for the prediction of failure onset for the inter-fiber mode. MAT261 (Pinho et al., 2006a, 2006b) and MAT262 (Maimi et al., 2007a, 2007b) uses linear softening and linear/bi-linear softening evolution, respectively, based on fracture toughness of the composite. The failure models implemented in both these two models are mesh independent which is a very attractive feature. The models have erosion criterion based on effective strain. It also has a feature where the fracture toughness can be defined as a function of strain rate and characteristic length of the element. The strength parameters are required as input to drive the models. These strength parameters can be defined as a function of strain rate. The in-plane shear properties are taken as input in the form of tabulated stress strain data as a function of strain rate. The carshfront and the strain rate smoothing features are also available with both these models.

Apart from the material models described above, there are additional "add on" material models which can be used as an extension to most of the available LS-DYNA models to support damage, failure, and element erosion. Some of these are MAT_ADD_EROSION, MAT_ADD_DAMAGE_DIEM and MAT_ADD_DAMAGE_GISSMO (Ansys-LST, 2018). Table 1 shows most of the desirable features for modeling composite materials, and Table 2 (Schweizerhof et al., 1998; Ansys-LST, 2020a) summarizes availability of the features for all the aforementioned composite material models. "Y" implies that the

16

feature is available in the material model, "N" implies that the feature is not available, and "S" implies that the feature is partially available and can be used for some of the input parameter.

To overcome the drawbacks of the existing material models, an orthotropic elasto-plastic damage material model (OEPDMM) has been developed. This material model is implemented in LS-DYNA as MAT213 (Goldberg et al., 2016; Hoffarth et al., 2016), also known as MAT_COMPOSITE_PLASTICITY_DAMAGE. OEPDMM is a modular material model with three sub-models – deformation, damage, and failure. The deformation sub-model is based on plasticity theory and predicts the linear and the non-linear behavior of a material. It is driven by a set of at least twelve stress-strain curves. Additional stress-strain curves obtained at different strain-rate and temperature combinations can be used as input. These stress-strain curves can be obtained either through experiments (Khaled et al., 2017) or virtual testing (Harrington et al., 2017). This provides control over the way the hardening/softening evolves as well as handles tension-compression asymmetry both for the linear and the non-linear behavior – a feature which is not available with the other material models. The damage sub-model predicts the reduction in the stiffness of a material and is also driven by tabulated damage parameters (Khaled et al., 2018). With the deformation and the damage sub-models being uncoupled allows for incorporation of permanent deformations while still allowing for unloading (pre-peak regime) and stress degradation (post-peak regime). The prior implementation, however, has limitations in simulating a dynamic event especially involving stress- strain input curves at different strain-rates. Furthermore, the failure sub-models which have

been implemented are not mature enough. The goal of this dissertation is to enhance the deformation and the damage sub-model, and implement two different failure approaches in OEPDMM, to overcome the limitations the current implementation has. The failure sub-models newly implemented are Puck Failure Model (PFC) which is based on Puck theory (Shyamsunder et al., 2020a) and a Generalized Tabulated Failure Model (GTFC) (Goldberg et al., 2018b; Shyamsunder et al., 2020b).

Table 1. Desirable Features in Composite Material Models

Feature	Why is it desirable?
Tabulated Input	Can have any smoothly varying and/or continuous data. Not constrained by the form of any equation.
Tension/Compression asymmetry including pure linear behavior	Composites typically are stronger in tension than compression. Some brittle composites have linear behavior.
Plasticity	The matrix usually exhibits plastic behavior (permanent deformation).
Solid element	Needed for thick composites where shell element modeling would not be appropriate. Whenever through the thickness shear becomes important in the penetration process.
Shell element	Needed for thin composites where in-plane behavior is dominant, but loading can be out-of-plane.
Damage model	Used to model unloading and reloading.
Failure model	Tabulated makes it possible to define any failure surface shape.
Rate effects	Composites may exhibit rate-dependent behavior.
Temperature effects	Composite materials may behave differently at different temperatures. Rapid loading can heat up the composite and thereby changing its properties (Taylor-Quinney effect).
Stochastic	Can study effect of variation in material properties.
Implicit	Modeling slowly loaded structures.

Table 2. Summary of the Features Available in LS-DYNA Composite Material Models

MAT	Tabulated Input	Tension/Compression Asymmetry	Plasticity	Solid Element	Shell Element	Damage Model	In-built Failure Model	Rate Effects	Temperature Effects	Stochastic	Implicit
022	N	N	N	Y	Y	Y	N	N	N	N	Y
023	S	N	N	Y	Y	N	N	N	Y	N	Y
054 /55	N	N	N	Y	Y	Y	Y	Y	N	N	N
058	S	N	N	N	Y	Y	Y	Y	N	N	N
059	N	N	N	Y	Y	Y	Y	N	N	N	Y
116	N	N	N	N	Y	N	N	N	N	N	N
117	N	N	N	N	Y	N	N	N	N	N	N
118	N	N	N	N	Y	N	N	N	N	N	N
158	N	N	N	N	Y	Y	Y	Y	N	N	N
161 /162	N	N	N	Y	Y	Y	Y	Y	N	N	Y
219	N	N	N	Y	Y	Y	Y	N	N	N	N
221	N	N	N	Y	N	Y	Y	N	N	N	N
261 /262	S	N	N	Y	Y	Y	Y	S	N	N	N
213	Y	Y	Y	Y	Y	Y	Y	Y	Y	Y	N

1.3   Research Objectives

The primary focus of this work is to develop, build, program and test new capabilities in OEPDMM to address the additional desirable features listed in Table 1. A summary of the research objectives is listed below.

1. Enhance OEPDMM deformation and damage sub-models to simulate rate dependent composite behavior.

2. Implement Puck Failure model and Generalized Tabulated Failure model.

3. Verify the developed capabilities via single and multiple element test cases.

4. Validate the developed capabilities using statically loaded structural test results from ASU, and impact test results from NASA-GRC.

In Chapter 2, the background on the deformation and the damage sub-models is discussed. The enhancement of the deformation sub-model to take into consideration, the visco-elastic-plastic material behavior is presented. In addition to this, the modifications which are made to the damage sub-model with the consideration of visco-elastic-plastic formulation is also discussed. Item 1 from the list of research objectives is addressed in this chapter.

Chapter 3 is divided into two parts. In the first part, theory and the implementation scheme of the Puck Failure Model is presented followed by the stress degradation technique that is coupled with the Puck Failure Model. In the second part, the development and the implementation of Generalized Tabulated Failure model is presented. Item 2 from the list of research objectives is addressed in this chapter.

In Chapter 4 verification and validation tests are presented. First, single element verification tests are used to demonstrate all the features implemented in OEPDMM. Second, validation test using quasi-statically loaded stacked-ply specimens. Finally, the ballistic impact tests are discussed. Details include processing of experimental data to meet OEPDMM requirements, the finite element model, calibration of failure parameters, and comparison of FE predictions with experimental data. Items 3 and 4 from the list of research objectives are addressed in this chapter.

The dissertation document concludes with Chapter 5. The possible improvements which can be made to the material model are highlighted in this chapter.

2 DEFORMATION AND DAMAGE SUB-MODEL IN OEPDMM

The deformation and the damage sub-models in OEPDMM are briefly discussed in this chapter. The prior formulation (Hoffarth, 2016) has been modified to support rate and temperature dependent data so that impact events can be modeled. The new features include strain-rate smoothing, Poisson's ratio modification, multi-level plastic multiplier computation techniques, and supporting Taylor-Quinney effect.

2.1 Current State of the Art

A plasticity based orthotropic material model had been developed and implemented into the commercial finite element code LS-DYNA® (Ansys-LST, 2020b) as *MAT_COMPOSITE_TABULATED_PLASTICITY_DAMAGE (CTPD) model, or *MAT213. OEPDMM has three sub-models that are user selectable with the primary sub-model for deformation that is always active and can be made to work in conjunction with the sub-models for damage and for failure. Prior publications contain the details of the deformation (Goldberg et al., 2016; Hoffarth et al., 2016, 2017, 2020; Khaled et al., 2017) and damage sub-models (Goldberg et al., 2018a; Khaled et al., 2018).

Classical plasticity theory is used in the deformation sub-model, and the initiation of plasticity is dictated by converting the classical Tsai-Wu failure criterion to a quadratic, orthotropic yield function (Tsai & Wu, 1971),

$$f(\sigma) = a + \begin{pmatrix} F_1 & F_2 & F_3 & 0 & 0 & 0 \end{pmatrix} \begin{bmatrix} \sigma_{11} \\ \sigma_{22} \\ \sigma_{33} \\ \sigma_{12} \\ \sigma_{23} \\ \sigma_{13} \end{bmatrix}$$

$$+ \begin{bmatrix} \sigma_{11} \\ \sigma_{22} \\ \sigma_{33} \\ \sigma_{12} \\ \sigma_{23} \\ \sigma_{13} \end{bmatrix}^T \begin{bmatrix} F_{11} & F_{12} & F_{13} & 0 & 0 & 0 \\ F_{12} & F_{22} & F_{23} & 0 & 0 & 0 \\ F_{13} & F_{23} & F_{33} & 0 & 0 & 0 \\ 0 & 0 & 0 & F_{44} & 0 & 0 \\ 0 & 0 & 0 & 0 & F_{55} & 0 \\ 0 & 0 & 0 & 0 & 0 & F_{66} \end{bmatrix} \begin{bmatrix} \sigma_{11} \\ \sigma_{22} \\ \sigma_{33} \\ \sigma_{12} \\ \sigma_{23} \\ \sigma_{13} \end{bmatrix}$$

(2.1)

The yield function coefficients (F_i's and F_{ij}'s) are computed based on the current yield stresses. In order to track the yield stresses in the various coordinate directions for the given state of stress, the input to the model includes twelve sets of tabulated stress-strain data consisting of stress-strain curves in tension in the 1, 2 and 3 directions (where 1, 2 and 3 are the Principal Material Directions (PMDs)), in compression in the 1, 2 and 3 directions, tensorial shear stress-strain in the shear 1-2, 2-3 and 1-3 planes, and off-axis stress-strain curves in 1-2, 2-3 and 1-3 planes. If the material exhibits rate and/or temperature dependency, the twelve input curves can be defined for as many sets of different strain-rate and temperature combinations as required. These stress-strain curves can be obtained experimentally (Khaled et al., 2017) or by virtual testing (Harrington et al., 2017). The yield stresses need to be such that the yield surface is convex at any point of time so that a converging solution is obtained (Hoffarth, 2016). If for any reason, the yield surface is not convex, convexity is enforced (Hoffarth et al., 2016). The flow law

24

considered in the deformation model is non-associative and is defined in terms of the

plastic potential function given as,

$$h = \sqrt{\begin{aligned} &H_{11}\sigma_{11}^2 + H_{22}\sigma_{22}^2 + H_{33}\sigma_{33}^2 + 2H_{12}\sigma_{11}\sigma_{22} + 2H_{23}\sigma_{22}\sigma_{33} + \\ &2H_{31}\sigma_{33}\sigma_{11} + H_{44}\sigma_{12}^2 + H_{55}\sigma_{23}^2 + H_{66}\sigma_{13}^2 \end{aligned}} \qquad (2.2)$$

where H_{ij} are (nine) constant coefficients that depend on the average value of various

plastic Poisson's ratios. Experimental data are used to calculate the flow rule coefficients

as follows. First, the unidirectional test results from the PMDs are used to calculate six of

the coefficients. For example, Eq. 2.3 shows how the simplified plastic potential function

along with the relationship $\dot{\boldsymbol{\varepsilon}}^p = \dot{\lambda}\dfrac{\partial h}{\partial \boldsymbol{\sigma}}$, can be used to compute the plastic Poisson's

ratios, v_{ij}^p as,

$$
\begin{array}{lll}
\sigma_{11} \neq 0 & \sigma_{22} \neq 0 & \sigma_{33} \neq 0 \\[6pt]
v_{12}^p = -\dfrac{\dot{\varepsilon}_{22}^p}{\dot{\varepsilon}_{11}^p} = -\dfrac{H_{12}}{H_{11}} & v_{21}^p = -\dfrac{\dot{\varepsilon}_{11}^p}{\dot{\varepsilon}_{22}^p} = -\dfrac{H_{12}}{H_{22}} & v_{32}^p = -\dfrac{\dot{\varepsilon}_{22}^p}{\dot{\varepsilon}_{33}^p} = -\dfrac{H_{23}}{H_{33}} \\[10pt]
v_{13}^p = -\dfrac{\dot{\varepsilon}_{33}^p}{\dot{\varepsilon}_{11}^p} = -\dfrac{H_{13}}{H_{11}} & v_{23}^p = -\dfrac{\dot{\varepsilon}_{33}^p}{\dot{\varepsilon}_{22}^p} = -\dfrac{H_{23}}{H_{22}} & v_{31}^p = -\dfrac{\dot{\varepsilon}_{11}^p}{\dot{\varepsilon}_{33}^p} = -\dfrac{H_{13}}{H_{33}}
\end{array} \qquad (2.3)
$$

where, $\dot{\varepsilon}_{ij}^p$ are the plastic strain-rate components. Second, since Eq. 2.3 shows that the

flow rule coefficients are not linearly independent, one of the flow rule coefficients is

assumed – normally a value for the flow rule coefficient corresponding to the direction

with the most plasticity is assumed, after which Eq. 2.3 is used to compute the values of

the remaining coefficients. The stress-strain curve in this direction is denoted as the *master* curve. Third, the final three terms, H_{44}, H_{55} and H_{66}, are computed by fitting the shear curves with the master curve in the effective stress versus effective plastic strain space (Hoffarth et al., 2017).

Assuming strain compatibility in the true (damaged) and the effective (undamaged) stress spaces makes it possible to decouple damage and plasticity. This allows the deformation model, governed by a plasticity algorithm, to account for both elastic and inelastic deformations while the reduction of elastic stiffness in the principal material directions and principal material planes is handled by the damage model (Khaled et al., 2018). The relationship between the true stress space and the effective stress space is captured in the damage sub-model as,

$$
\begin{pmatrix} \sigma_{11} \\ \sigma_{22} \\ \sigma_{33} \\ \sigma_{12} \\ \sigma_{23} \\ \sigma_{13} \end{pmatrix} = \begin{bmatrix} M_{11} & 0 & 0 & 0 & 0 & 0 \\ 0 & M_{22} & 0 & 0 & 0 & 0 \\ 0 & 0 & M_{33} & 0 & 0 & 0 \\ 0 & 0 & 0 & M_{44} & 0 & 0 \\ 0 & 0 & 0 & 0 & M_{55} & 0 \\ 0 & 0 & 0 & 0 & 0 & M_{66} \end{bmatrix} \begin{pmatrix} \sigma_{11}^{eff} \\ \sigma_{22}^{eff} \\ \sigma_{33}^{eff} \\ \sigma_{12}^{eff} \\ \sigma_{23}^{eff} \\ \sigma_{13}^{eff} \end{pmatrix}
\tag{2.4}
$$

where $M_{ii} = M_{ii}\left(\varepsilon_{11}^{p}, \varepsilon_{22}^{p}, \varepsilon_{33}^{p}, \varepsilon_{12}^{p}, \varepsilon_{23}^{p}, \varepsilon_{13}^{p}\right)$. ε_{ij}^{p}'s are the plastic strain components. Unlike other formulations, the damage sub-model accounts for stiffness reduction via the use of both uncoupled and coupled damage parameters. This is evident from the relation

26

between the true stress $\left(\sigma_{ij}\right)$ and the effective stress $\left(\sigma_{ij}^{eff}\right)$ tensor components which are expressed using Eqs. 2.5 and 2.8. The normal (tensile and compressive) components of the stress are related as

$$\sigma_{ii}^{eff} = \begin{cases} \dfrac{\sigma_{ii}}{1-c_i^d} & \text{if } \sigma_{ii} \geq 0 \\[2mm] \dfrac{\sigma_{ii}}{1-c_{i+3}^d} & \text{if } \sigma_{ii} < 0 \end{cases} \tag{2.5}$$

with

$$\begin{aligned} c_i^d = 1 - \Big\{ & \left(1-d_{11_T}^{ii_T}\right)\left(1-d_{11_C}^{ii_T}\right)\left(1-d_{22_T}^{ii_T}\right)\left(1-d_{22_C}^{ii_T}\right) \\ & \left(1-d_{33_T}^{ii_T}\right)\left(1-d_{33_C}^{ii_T}\right)\left(1-d_{12}^{ii_T}\right)\left(1-d_{23}^{ii_T}\right)\left(1-d_{13}^{ii_T}\right) \Big\} \end{aligned} \tag{2.6}$$

$$\begin{aligned} c_{i+3}^d = 1 - \Big\{ & \left(1-d_{11_T}^{ii_C}\right)\left(1-d_{11_C}^{ii_C}\right)\left(1-d_{22_T}^{ii_C}\right)\left(1-d_{22_C}^{ii_C}\right) \\ & \left(1-d_{33_T}^{ii_C}\right)\left(1-d_{33_C}^{ii_C}\right)\left(1-d_{12}^{ii_C}\right)\left(1-d_{23}^{ii_C}\right)\left(1-d_{13}^{ii_C}\right) \Big\} \end{aligned} \tag{2.7}$$

where $i = 1, 2$ and 3. The shear components are given as

$$\sigma_{ij}^{eff} = \frac{\sigma_{ij}}{1-c_k^d} \tag{2.8}$$

with

$$\begin{aligned} c_k^d = 1 - \Big\{ & \left(1-d_{11_T}^{ij}\right)\left(1-d_{11_C}^{ij}\right)\left(1-d_{22_T}^{ij}\right)\left(1-d_{22_C}^{ij}\right) \\ & \left(1-d_{33_T}^{ij}\right)\left(1-d_{33_C}^{ij}\right)\left(1-d_{12}^{ij}\right)\left(1-d_{23}^{ij}\right)\left(1-d_{13}^{ij}\right) \Big\} \end{aligned} \tag{2.9}$$

27

where, ij =12, 23 and 13, and k = 7, 8 and 9, respectively. The parameters, c_i^d, are referred to as the effective damage parameters and are a measure of damage in each component in the principal material direction/plane (Shyamsunder et al., 2020b). As will be shown later, this parameter can also be used in the post-peak regime in the Generalized Tabulated Failure Model since it relates the true and the effective stress tensor components. d_{ij}^{kl} is referred to as the damage parameter and accounts for damage in the kl direction due to loading in the ij direction. If the ij direction and the kl direction are the same, then d_{ij}^{kl} is referred to as *uncoupled* damage parameter; else, it is referred to as *coupled* damage parameter. For example, $d_{22_T}^{22_T}$ is an uncoupled damage parameter obtained by loading the specimen in 2-direction tension and interrogating the reduction in stiffness in the 2-direction tension. Similarly, $d_{22_C}^{22_T}$ is a coupled damage parameter obtained by loading the specimen in 2-direction compression and interrogating the reduction in the stiffness in 2-direction tension.

The algorithm used in the prior implementation (Goldberg et al., 2016, 2018a; Hoffarth et al., 2016, 2017, 2020; Khaled et al., 2017, 2018) is shown in Figure 2 in the form of a flow-chart. The first step which is done once in a simulation is the pre-processing step. During this step, the input stress-strain data is converted into effective stress – effective plastic strain. The strain data is converted into plastic strain, and finally into effective plastic strain. In the subsequent step, the trial stress is corrected back depending on whether the state of trial stress is outside the yield surface or not.
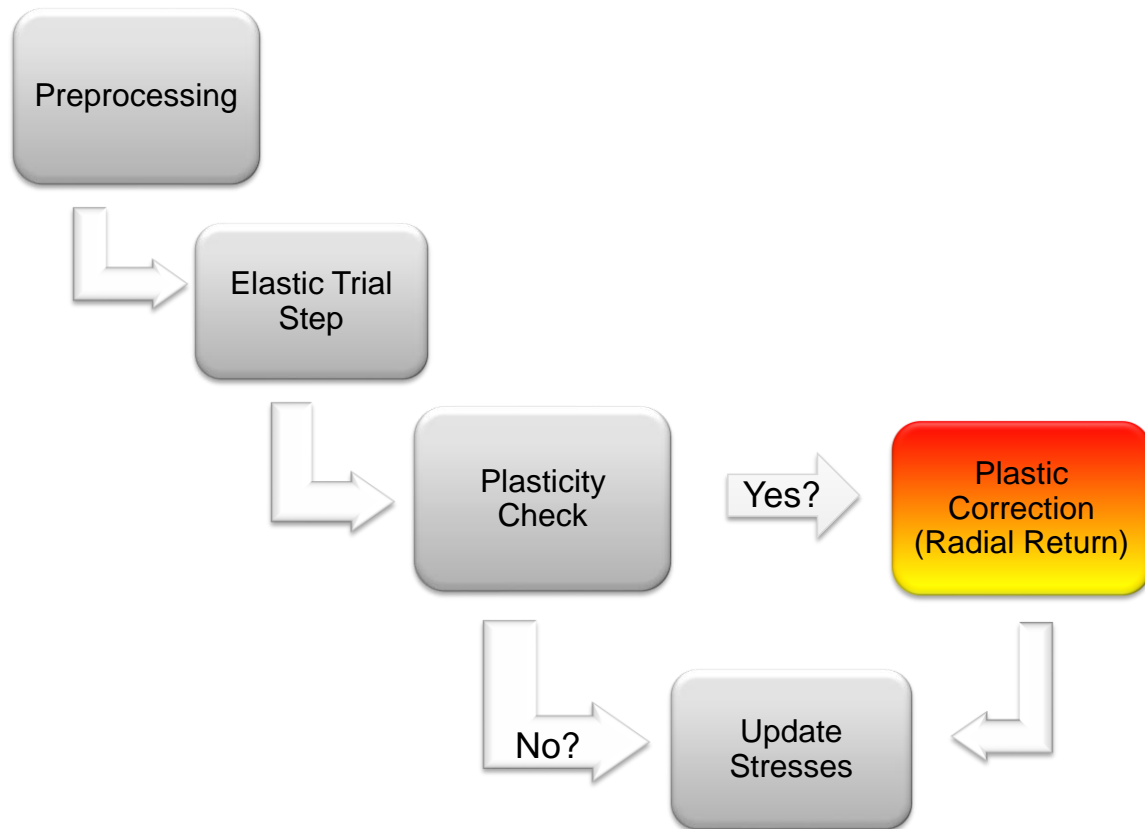
Figure 2. Algorithm Used in the Prior Implementation (Hoffarth, 2016)

2.2   Enhancements made to the Deformation and Damage Sub-models

The prior implementation however has some limitations which are listed below:

1. Noisy strain-rates can develop during an analysis which needs to be smoothed.

2. Convergence issue in the computation of plastic multiplier, especially in a complex loading scenario.

3. The Poisson's ratios used in the analysis can be thermodynamically inadmissible in analysis involving stress-strain input curves specified at multiple strain-rates.

4. Absence of features to model visco-elastic, visco-plastic, and visco-elastic-plastic behavior. The visco-elastic-plastic feature is of importance in modeling a dynamic event for composites.

5. No feature to predict the rise in temperature.

6. Absence of failure sub-models to predict the failure onset and element erosion.

The algorithm based on the new implementation is shown in Figure 3. The green color blocks highlight the enhancements made. Each of the features added other than the failure sub-model implementation is discussed one by one in the following sub-sections.
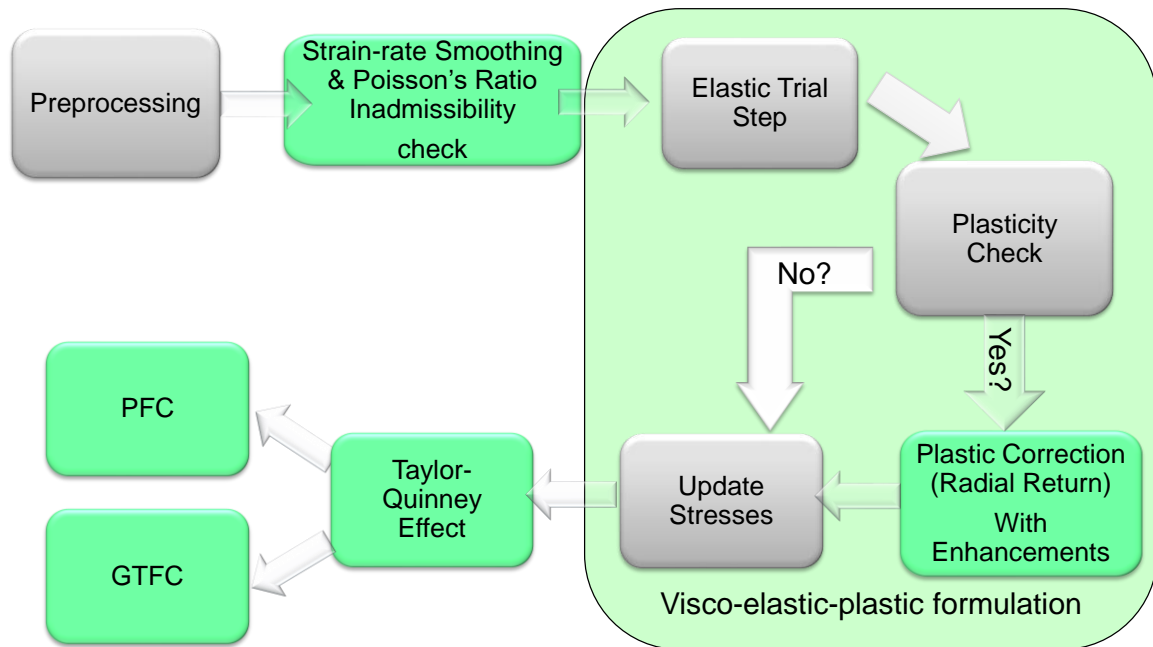
Figure 3. Algorithm Used in the New Implementation

2.2.1 Strain-rate Smoothing

A general three-dimensional constitutive law stiffness matrix formulation is used in the deformation sub-model. The stiffness matrix is given by

$$
\mathbf{C} = \mathbf{S}^{-1} =
\begin{bmatrix}
\dfrac{1}{E_{11}} & -\dfrac{v_{21}}{E_{22}} & -\dfrac{v_{31}}{E_{33}} & 0 & 0 & 0 \\[2mm]
& \dfrac{1}{E_{22}} & -\dfrac{v_{32}}{E_{33}} & 0 & 0 & 0 \\[2mm]
& & \dfrac{1}{E_{33}} & 0 & 0 & 0 \\[2mm]
& & & \dfrac{1}{2G_{12}} & 0 & 0 \\[2mm]
& Sym & & & \dfrac{1}{2G_{23}} & 0 \\[2mm]
& & & & & \dfrac{1}{2G_{13}}
\end{bmatrix}
\tag{2.10}
$$

The moduli are computed internally in OEPDMM using the input stress-strain curves interpolated for a given strain rate and temperature at a given point of time during the simulation. In order to avoid numerical instability due to sudden changes in moduli caused by sudden large changes in the strain rate, the strain rate components are smoothed using an exponential averaging technique,

$$
\dot{\boldsymbol{\varepsilon}}_{n+1}^{avg} = (1-s) \times \dot{\boldsymbol{\varepsilon}}_{n+1} + s \times \dot{\boldsymbol{\varepsilon}}_{n}^{avg}
\tag{2.11}
$$

where n represents the previous time step. s is a user-specified parameter with a value between 0 and 1. The average strain rate at the current time step, $\dot{\varepsilon}_{n+1}^{avg}$ is computed as a function of the non-smooth strain rate at the current time step, $\dot{\varepsilon}_{n+1}$ and the averaged strain rate from the previous time step, $\dot{\varepsilon}_{n}^{avg}$.

2.2.2 Poisson's Ratio Thermodynamic Inadmissibility

Eq. 2.10 is used assuming that Poisson's ratios are not rate and temperature dependent. The moduli, on the other hand, can be rate and temperature dependent. With the use of rate and/or temperature dependent stress-strain curves, it is possible that the user-input Poisson's ratios are not thermodynamically inadmissible with the orthotropy energy criteria (Lempriere, 1968). In order to eliminate this inadmissibility, the Poisson's ratio(s) is/are modified internally in OEPDMM. The following checks and corrections are done for each time step and at every Gauss point:

Step 1: Input - v_{21}, v_{32}, v_{31}, E_{11}, E_{22}, E_{33} and correction factor, $c_{prf} = 0.95$.

Step 2: If $|v_{21}| \geq \sqrt{\dfrac{E_{22}}{E_{11}}}$, go to Step 3, else go to Step 4.

Step 3: Set $v_{21} = c_{prf}\sqrt{\dfrac{E_{22}}{E_{11}}}$ and set FLAG21 = 1.

Step 4: If $|v_{32}| \geq \sqrt{\dfrac{E_{33}}{E_{22}}}$, go to Step 5, else go to Step 6.

Step 5: Set $v_{32} = c_{prf}\sqrt{\dfrac{E_{33}}{E_{22}}}$ and set FLAG32 = 1.

Step 6: If $|v_{31}| \geq \sqrt{\dfrac{E_{33}}{E_{11}}}$, go to Step 7, else go to Step 8.

Step 7: Set $v_{31} = c_{prf} \sqrt{\dfrac{E_{33}}{E_{11}}}$ and set FLAG31 = 1.

Step 8: Compute, $\det 2 = 1 - v_{21}^2 \dfrac{E_{11}}{E_{22}} - v_{32}^2 \dfrac{E_{22}}{E_{33}} - v_{31}^2 \dfrac{E_{11}}{E_{33}}$

Step 9: If $\left(v_{21}v_{32}v_{31}\dfrac{E_{11}}{E_{33}} \geq \dfrac{1}{2} \right)$ or $\left(v_{21}v_{32}v_{31}\dfrac{E_{11}}{E_{33}} \geq \dfrac{\det 2}{2} \right)$ or $\left(\dfrac{\det 2}{2} \geq \dfrac{1}{2} \right)$, go to Step 10a,

else continue with stiffness matrix formulation.

Step 10a: If FLAG21 = 1 Set $v_{21} = c_{prf}v_{21}$, and go to Step 10b.

Step 10b: elseif FLAG32 = 1 Set $v_{32} = c_{prf}v_{32}$, and go to Step 10c.

Step 10c: elseif FLAG31 = 1 Set $v_{31} = c_{prf}v_{31}$, and go to Step 10d.

Step 10d: else Set $v_{21} = c_{prf}v_{21}$, $v_{32} = c_{prf}v_{32}$ and $v_{31} = c_{prf}v_{31}$, and go to Step 8.

The default value of c_{prf} is taken as 0.95 (5% change) and this ensures that the correction

needed to satisfy the material relationships is as small as possible. In the next time step

and for a given Gauss point, the original Poisson's ratios are used and corrected if

necessary

2.2.3   Visco-elasticity and Visco-plasticity

There are at least three different approaches to visco-plasticity (Wang et al., 1997) –

overstress visco-plastic models of Perzyna and Duvaut-Lions, and the consistency visco-

plastic approach. In the present work, the consistency approach is used since only with this approach it is possible to use the Kuhn-Tucker form of the loading-unloading conditions in the visco-plastic case. Accordingly, the stress is divided into equilibrium, $\boldsymbol{\sigma}_{n+1}^{e,eff}$ and viscous, $\boldsymbol{\sigma}_{n+1}^{v,eff}$ components (Achstetter, 2019; DuBois et al., 2017) that are computed as,

$$\boldsymbol{\sigma}_{n+1}^{e,eff} = \boldsymbol{\sigma}_{n}^{e,eff} + \mathbf{C}_{\infty}\dot{\boldsymbol{\varepsilon}}_{n+1}^{avg}\Delta t \tag{2.11}$$

$$\boldsymbol{\sigma}_{n+1}^{v,eff} = \boldsymbol{\sigma}_{n}^{v,eff} \circ \boldsymbol{\beta} + \left[\left(\mathbf{C}-\mathbf{C}_{\infty}\right)\circ\mathbf{B}\right]\dot{\boldsymbol{\varepsilon}}_{n+1}^{avg}\Delta t \tag{2.12}$$

where $\circ$ denotes Hadamard product between the matrices or vectors. These computations take place in the effective stress space (Khaled et al., 2018) and hence the superscript *eff* is used. $\mathbf{C}_{\infty}$ is the equilibrium stiffness matrix generated using the moduli corresponding to the quasi-static stress-strain curves while $\mathbf{C}$ is the total stiffness matrix generated using the moduli corresponding to the current strain rate. $\boldsymbol{\beta}$ and $\mathbf{B}$ are a vector and a matrix containing among other parameters exponential functions of decay constants (Achstetter, 2019),

$$\boldsymbol{\beta} = \left[e^{-\beta_{11}\Delta t} \quad e^{-\beta_{22}\Delta t} \quad e^{-\beta_{33}\Delta t} \quad e^{-\beta_{44}\Delta t} \quad e^{-\beta_{55}\Delta t} \quad e^{-\beta_{66}\Delta t}\right]^{T} \tag{2.13}$$

$$
\mathbf{B} = \begin{bmatrix}
\dfrac{1-e^{-\beta_{11}\Delta t}}{\beta_{11}\Delta t} & \dfrac{1-e^{-\beta_{12}\Delta t}}{\beta_{12}\Delta t} & \dfrac{1-e^{-\beta_{13}\Delta t}}{\beta_{13}\Delta t} & 0 & 0 & 0 \\[2.5ex]
\dfrac{1-e^{-\beta_{12}\Delta t}}{\beta_{12}\Delta t} & \dfrac{1-e^{-\beta_{22}\Delta t}}{\beta_{22}\Delta t} & \dfrac{1-e^{-\beta_{23}\Delta t}}{\beta_{23}\Delta t} & 0 & 0 & 0 \\[2.5ex]
\dfrac{1-e^{-\beta_{13}\Delta t}}{\beta_{13}\Delta t} & \dfrac{1-e^{-\beta_{23}\Delta t}}{\beta_{23}\Delta t} & \dfrac{1-e^{-\beta_{33}\Delta t}}{\beta_{33}\Delta t} & 0 & 0 & 0 \\[2.5ex]
0 & 0 & 0 & \dfrac{1-e^{-\beta_{44}\Delta t}}{\beta_{44}\Delta t} & 0 & 0 \\[2.5ex]
0 & 0 & 0 & 0 & \dfrac{1-e^{-\beta_{55}\Delta t}}{\beta_{55}\Delta t} & 0 \\[2.5ex]
0 & 0 & 0 & 0 & 0 & \dfrac{1-e^{-\beta_{66}\Delta t}}{\beta_{66}\Delta t}
\end{bmatrix}
\tag{2.14}
$$

There is no known procedure to obtain β_{ij} values as of now and must be estimated by the user. It should be noted that $ij = 11, 22, 33, 12, 23, 13, 44, 55, 66$ and that these values cannot be negative (Achstetter, 2019). Larger values of β will negate the rate effect. The components of $\boldsymbol{\sigma}_n^{e,eff}$ and $\boldsymbol{\sigma}_n^{v,eff}$ are given by the following equations,

$$\sigma_{11,n}^{i,eff} = \begin{cases} \dfrac{\sigma_{11,n}^{i}}{1-c_1^d} & if\ \sigma_{11,n} \geq 0 \\[2mm] \dfrac{\sigma_{11,n}^{i}}{1-c_4^d} & if\ \sigma_{11,n} < 0 \end{cases} \quad (2.15) \qquad \sigma_{33,n}^{i,eff} = \begin{cases} \dfrac{\sigma_{33,n}^{i}}{1-c_3^d} & if\ \sigma_{33,n} \geq 0 \\[2mm] \dfrac{\sigma_{33,n}^{i}}{1-c_6^d} & if\ \sigma_{33,n} < 0 \end{cases} \quad (2.17)$$

$$\sigma_{22,n}^{i,eff} = \begin{cases} \dfrac{\sigma_{22,n}^{i}}{1-c_2^d} & if\ \sigma_{22,n} \geq 0 \\[2mm] \dfrac{\sigma_{22,n}^{i}}{1-c_5^d} & if\ \sigma_{22,n} < 0 \end{cases} \quad (2.16)$$

$$\sigma_{12,n}^{i,eff} = \frac{\sigma_{12,n}^{i}}{1-c_7^d} \qquad (2.18)$$

$$\sigma_{23,n}^{i,eff} = \frac{\sigma_{23,n}^{i}}{1-c_8^d} \qquad (2.19)$$

$$\sigma_{13,n}^{i,eff} = \frac{\sigma_{13,n}^{i}}{1-c_9^d} \qquad (2.20)$$

where, i can be either e (equilibrium) or v (viscous) and the stress components on the right-hand side are in the true stress space. An assumption is thus made that damage affects the equilibrium and viscous stresses in the same way. The conversion from the true stress space to the effective stress space is done separately for the equilibrium and the viscous components. The components of $\boldsymbol{\sigma}_n^{v,eff}$ are taken as zero if the material is assumed to be purely visco-plastic. The total trial stress is computed using the following equation,

$$\boldsymbol{\sigma}_{n+1}^{t,eff} = \boldsymbol{\sigma}_{n+1}^{e,eff} + \boldsymbol{\sigma}_{n+1}^{v,eff} \qquad (2.22)$$

The total trial stress is corrected back to the yield surface using a radial return algorithm. More detail into the radial return algorithm will be discussed in Section 2.2.4. The yield

function which is a modified version of the quadratic Tsai-Wu failure criterion, which is given by Eq. 2.1 can be re-written as,

$$f(\boldsymbol{\sigma}_{n+1}^{t,eff}) = -1 + \begin{pmatrix} F_1 & F_2 & F_3 & 0 & 0 & 0 \end{pmatrix} \boldsymbol{\sigma}_{n+1}^{t,eff} + \left\{\boldsymbol{\sigma}_{n+1}^{t,eff}\right\}^T \mathbf{F} \boldsymbol{\sigma}_{n+1}^{t,eff} \qquad (2.23)$$

$$\text{where, } \mathbf{F} = \begin{bmatrix} F_{11} & F_{12} & F_{13} & 0 & 0 & 0 \\ F_{12} & F_{22} & F_{23} & 0 & 0 & 0 \\ F_{13} & F_{23} & F_{33} & 0 & 0 & 0 \\ 0 & 0 & 0 & F_{44} & 0 & 0 \\ 0 & 0 & 0 & 0 & F_{55} & 0 \\ 0 & 0 & 0 & 0 & 0 & F_{66} \end{bmatrix}$$

In the new implementation, the yield function coefficients (F_i 's and F_{ij} 's) are computed based on the current yield stresses corresponding to the quasi-static stress-strain curves to predict the onset of plasticity (Hoffarth et al., 2016). The stress tensor in the effective space is updated as,

$$\boldsymbol{\sigma}_{n+1}^{eff} = \boldsymbol{\sigma}_{n+1}^{t,eff} - \left[\mathbf{C}_\infty + \left(\mathbf{C} - \mathbf{C}_\infty\right) \circ \mathbf{B}\right] \Delta\lambda \left.\frac{\partial h}{\partial \boldsymbol{\sigma}}\right|_{\boldsymbol{\sigma}_{n+1}^{t,eff}} \qquad (2.24)$$

where $\Delta\lambda$ is the plastic multiplier increment. It is taken as zero if the material is assumed to be purely visco-elastic. During the simulation, $\Delta\lambda$ is computed as a function of the current yield stress obtained from interpolation using the current plastic multiplier ($\dot{\lambda}$). The highest or the lowest rate curves are used if the current value is greater than or less than the given user input curves. After the stress is updated using Eq. 2.24, the

equilibrium and the viscous stresses need to be updated. In order to ensure that the total stress is equal to the sum of the equilibrium and the viscous stress, these stress tensors are updated as follows:

If $f(\boldsymbol{\sigma}_{n+1}^{e,eff}) \le \delta_{tol}$,

$$\boldsymbol{\sigma}_{n+1}^{e,eff} = \boldsymbol{\sigma}_{n+1}^{e,eff} \tag{2.25}$$

$$\boldsymbol{\sigma}_{n+1}^{v,eff} = \boldsymbol{\sigma}_{n+1}^{v,eff} - \left[\mathbf{C}_\infty + \left(\mathbf{C} - \mathbf{C}_\infty\right) \circ \mathbf{B}\right] \Delta\lambda \left.\frac{\partial h}{\partial \boldsymbol{\sigma}}\right|_{\boldsymbol{\sigma}_{n+1}^{t,eff}} \tag{2.26}$$

else

$$\boldsymbol{\sigma}_{n+1}^{e,eff} = \left(\boldsymbol{\sigma}_{n+1}^{e,eff} - \mathbf{C}_\infty \Delta\lambda \left.\frac{\partial h}{\partial \boldsymbol{\sigma}}\right|_{\boldsymbol{\sigma}_{n+1}^{t,eff}}\right) \tag{2.27}$$

$$\boldsymbol{\sigma}_{n+1}^{v,eff} = \boldsymbol{\sigma}_{n+1}^{v,eff} - \left[\left(\mathbf{C} - \mathbf{C}_\infty\right) \circ \mathbf{B}\right] \Delta\lambda \left.\frac{\partial h}{\partial \boldsymbol{\sigma}}\right|_{\boldsymbol{\sigma}_{n+1}^{t,eff}} \tag{2.28}$$

where δ_{tol} is a numerical tolerance (default value of 10^{-6}). Eqs. 2.25-2.28 show that as long as the yield function value computed from the equilibrium stress is non-positive, the return to the yield surface is achieved by reducing the viscous stresses only. This ensures that the stress does not fall below the equilibrium stress in the effective space. Finally, $\boldsymbol{\sigma}_{n+1}^{eff}$, $\boldsymbol{\sigma}_{n+1}^{e,eff}$ and $\boldsymbol{\sigma}_{n+1}^{v,eff}$ are converted into the true stress space using Eqs. 2.5, 2.8, 2.15-2.20. The updated $\boldsymbol{\sigma}_{n+1}^{e,eff}$ and $\boldsymbol{\sigma}_{n+1}^{v,eff}$ are used in the next time step for computation of the trial stress.

38

2.2.4 Plastic Multiplier Computation

The computation of the plastic multiplier increment, $\Delta\lambda$ (at a given time step and stress Gauss point) is carried out in two stages. The first stage involves bracketing the root with lower bound ($\Delta\lambda_1$) and upper bound ($\Delta\lambda_2$). In the second stage, secant iteration technique is used to find the root. A detail discussion on the second stage including the algorithm used can be found in Hoffarth (2016). The techniques used in bracketing the root is discussed in this sub-section. $\Delta\lambda_1$ is always taken as zero and hence corresponds to trial yield function value (f_{TRIAL}). $\Delta\lambda_2$ corresponds to a value of yield function, f which is negative.

Following are the steps involved in finding $\Delta\lambda_2$:

Step 1: An initial estimate of the plastic multiplier increment ($\Delta\lambda_2^1$) is computed based on the assumption that the time step is perfectly plastic (Hoffarth, 2016) as,

$$\Delta\lambda_2^1 = \frac{\dfrac{\partial f}{\partial \boldsymbol{\sigma}_{n+1}^{t,eff}} : \left(\boldsymbol{\sigma}_{n+1}^{t,eff} - \boldsymbol{\sigma}_{n}^{eff} \right)}{\dfrac{\partial f}{\partial \boldsymbol{\sigma}_{n+1}^{t,eff}} \mathbf{C} : \dfrac{\partial h}{\partial \boldsymbol{\sigma}_{n+1}^{t,eff}}} \tag{2.29}$$

The yield function value is computed based on this estimate ($f(\Delta\lambda_2^1)$). If $f(\Delta\lambda_2^1)$ is negative, it implies that $\Delta\lambda_2^1$ is the upper bound ($\Delta\lambda_2 = \Delta\lambda_2^1$). In this case, follow the secant iteration technique, otherwise go to Step 2.

$f(\Delta\lambda)$

f_{TRIAL}

$\dfrac{\Delta\lambda_2^1}{1000}$ $\dfrac{\Delta\lambda_2^1}{1000}$ $\dfrac{\Delta\lambda_2^1}{1000}$

0 $\Delta\lambda_2^2$ $\Delta\lambda_2^3$ $\Delta\lambda_2^4$ $\Delta\lambda_2^5$ $\Delta\lambda_2^1$ $\Delta\lambda$

$\Delta\lambda_1$ $\Delta\lambda_2$

(a)

$f(\Delta\lambda)$

f_{TRIAL}

0 $\Delta\lambda_2^1$ $\Delta\lambda_2^2$ $\Delta\lambda_2^3$ $\Delta\lambda$

$\Delta\lambda_1$ $\Delta\lambda_2$

(b)
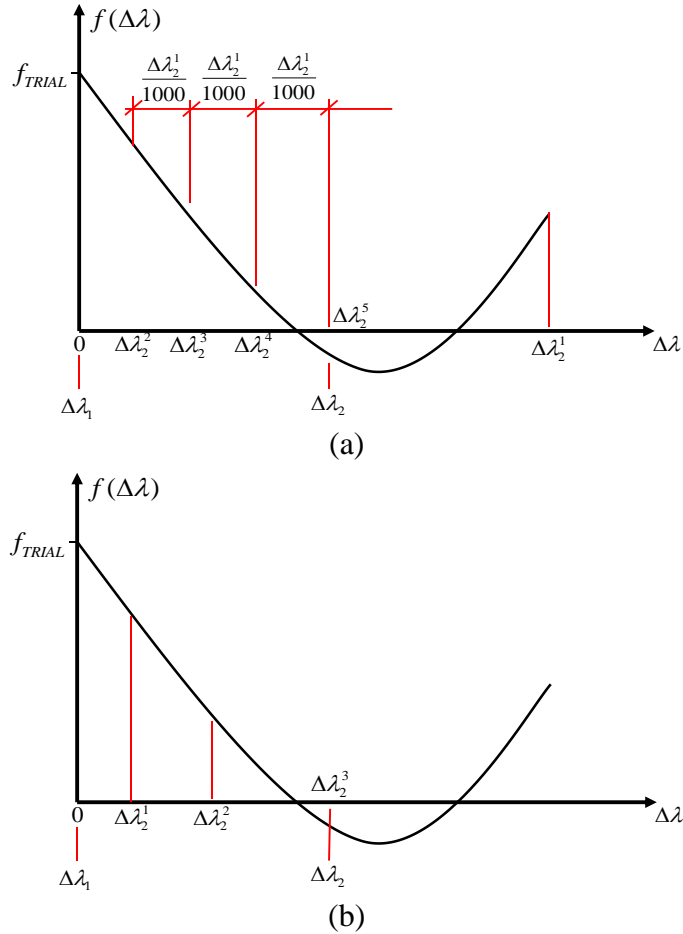
Figure 4. Plastic Multiplier Increment Computation: (a) Bounding the Root from the Left Regime (b) Bounding the Root towards the Right regime

Step 2: If $f(\Delta\lambda_2^1)$ is positive as depicted in Figure 4(a), an exhaustive search is carried out by discretizing the region from 0 to the $\Delta\lambda_2^1$. If a negative f cannot be found, the search is continued to the right of $\Delta\lambda_2^1$ using a geometric sequence as shown in Figure 4(b). Numerical experience with solving tens of problems has shown that discretizing the initial search region into 1000 points, using a multiplier of 1.1 for the second search region, and searching for a maximum of 1000 iterations more often than not yields the

correct $\Delta\lambda_2$ if one exists. If $\Delta\lambda_2$ is found, follow the secant iteration technique, otherwise go to Step 3. Step 3 is skipped if the technique discussed in it has been used before at the given time step and stress Gauss point.

Step 3: There can be cases where finding $\Delta\lambda_2$ using the non-associated flow rule is impossible. In such a case, the flow rule is modified to be associated (Achstetter, 2019). The plastic potential function which appears in the plastic work equation (Hoffarth, 2016) is replaced by the yield function,

$$\dot{W}_p = \boldsymbol{\sigma}_{n+1}^{t,eff} : \dot{\boldsymbol{\varepsilon}}_p = \boldsymbol{\sigma}_{n+1}^{t,eff} : \dot{\lambda} \frac{\partial h}{\partial \boldsymbol{\sigma}_{n+1}^{t,eff}} = \boldsymbol{\sigma}_{n+1}^{t,eff} : \dot{\lambda}^{\mathrm{mod}} \frac{\partial f}{\partial \boldsymbol{\sigma}_{n+1}^{t,eff}} k \qquad (2.30)$$

where, k is a scalar quantity to keep the equations consistent in dimensions; f is dimensionless whereas h has a dimension of stress. $\dot{\lambda}^{\mathrm{mod}}$ is the plastic multiplier corresponding to an associated flow rule and can be assumed to be the same as $\dot{\lambda}$ since the condition is to maintain plastic work compatibility via k. Eq. 2.26 can be re-arranged to as,

$$k = \frac{\boldsymbol{\sigma}_{n+1}^{t,eff} : \dfrac{\partial h}{\partial \boldsymbol{\sigma}_{n+1}^{t,eff}}}{\boldsymbol{\sigma}_{n+1}^{t,eff} : \dfrac{\partial f}{\partial \boldsymbol{\sigma}_{n+1}^{t,eff}}} \qquad (2.31)$$

Eq. 2.30 can be re-written by replacing the expression for k as,

$$\dot{W}_p = \boldsymbol{\sigma}_{n+1}^{t,eff} : \dot{\lambda} \frac{\partial f}{\partial \boldsymbol{\sigma}_{n+1}^{t,eff}} \frac{\boldsymbol{\sigma}_{n+1}^{t,eff} : \dfrac{\partial h}{\partial \boldsymbol{\sigma}_{n+1}^{t,eff}}}{\boldsymbol{\sigma}_{n+1}^{t,eff} : \dfrac{\partial f}{\partial \boldsymbol{\sigma}_{n+1}^{t,eff}}} \tag{2.32}$$

Eq. 2.32 modifies the direction of the return without modifying the plastic multiplier. In cases where the angle between the flow direction and the yield surface makes the plasticity algorithm incapable of correcting the trial state of stress, this modification can help locate a point on the yield surface. As per Eq. 2.32, $\dfrac{\partial h}{\partial \boldsymbol{\sigma}_{n+1}^{t,eff}}$ in Eq. 2.29 is replaced

by the term on the right hand side of Eq. 2.33 and Step 1 and/or Step 2 are/is carried out.

$$\frac{\partial h}{\partial \boldsymbol{\sigma}_{n+1}^{t,eff}} \rightarrow \frac{\partial f}{\partial \boldsymbol{\sigma}_{n+1}^{t,eff}} \frac{\boldsymbol{\sigma}_{n+1}^{t,eff} : \dfrac{\partial h}{\partial \boldsymbol{\sigma}_{n+1}^{t,eff}}}{\boldsymbol{\sigma}_{n+1}^{t,eff} : \dfrac{\partial f}{\partial \boldsymbol{\sigma}_{n+1}^{t,eff}}} \tag{2.33}$$

Step 4: In rare cases, due to the complexity of the state of stress, the plasticity algorithm might not be able to bound the solution even after switching to the associate flow rule. In this case, the state of trial stress is corrected to point towards the origin of the stress space. Eq. 2.24 can be re-written as,

$$\boldsymbol{\sigma}_{n+1}^{eff} = \boldsymbol{\sigma}_{n+1}^{t,eff} - \mathbf{K}\Delta\lambda \left. \frac{\partial h}{\partial \boldsymbol{\sigma}} \right|_{\boldsymbol{\sigma}_{n+1}^{t,eff}} \tag{2.34}$$

where, $\mathbf{K} = \mathbf{C}_\infty + (\mathbf{C} - \mathbf{C}_\infty) \circ \mathbf{B}$. Since, the radial return must be in the direction of the

origin of the trial stress instead of $-\mathbf{K} \left. \dfrac{\partial h}{\partial \boldsymbol{\sigma}} \right|_{\boldsymbol{\sigma}_{n+1}^{t,eff}}$, Eq. 2.34 is further modified as

$$\boldsymbol{\sigma}_{n+1}^{eff} = \left(\boldsymbol{\sigma}_{n+1}^{t,eff} - \Delta\lambda \boldsymbol{\sigma}_{n+1}^{t,eff} n \right) \tag{2.35}$$

or,
$$\boldsymbol{\sigma}_{n+1}^{eff} = \boldsymbol{\sigma}_{n+1}^{t,eff} - \mathbf{K}\Delta\lambda \left(\mathbf{K}^{-1} \boldsymbol{\sigma}_{n+1}^{t,eff} n \right) \tag{2.36}$$

where, n is a quantity to ensure that the plastic multiplier (increment) has the same value

as that of the non-associated case (Achstetter, 2019). Eq. 2.30 can be used to find the

expression for n,

$$\dot{W}_p = \boldsymbol{\sigma}_{n+1}^{t,eff} : \dot{\boldsymbol{\varepsilon}}_p = \boldsymbol{\sigma}_{n+1}^{t,eff} : \dot{\lambda} \frac{\partial h}{\partial \boldsymbol{\sigma}_{n+1}^{t,eff}} = \boldsymbol{\sigma}_{n+1}^{t,eff} : \dot{\lambda} \mathbf{K}^{-1} \boldsymbol{\sigma}_{n+1}^{t,eff} n \tag{2.37}$$

or
$$n = \frac{\boldsymbol{\sigma}_{n+1}^{t,eff} : \dfrac{\partial h}{\partial \boldsymbol{\sigma}_{n+1}^{t,eff}}}{\boldsymbol{\sigma}_{n+1}^{t,eff} : \mathbf{K}^{-1} \boldsymbol{\sigma}_{n+1}^{t,eff}} \tag{2.38}$$

As per Eq. 2.38, $\dfrac{\partial h}{\partial \boldsymbol{\sigma}_{n+1}^{t,eff}}$ in Eq. 2.29 is replaced by the term on the right hand side of Eq.

2.39 and Step 1 and/or Step 2 are/is carried out.

$$\frac{\partial h}{\partial \boldsymbol{\sigma}_{n+1}^{t,eff}} \rightarrow \mathbf{K}^{-1} \boldsymbol{\sigma}_{n+1}^{t,eff} \frac{\boldsymbol{\sigma}_{n+1}^{t,eff} : \dfrac{\partial h}{\partial \boldsymbol{\sigma}_{n+1}^{t,eff}}}{\boldsymbol{\sigma}_{n+1}^{t,eff} : \mathbf{K}^{-1} \boldsymbol{\sigma}_{n+1}^{t,eff}} \tag{2.39}$$

43

All these techniques have been implemented to make the plasticity algorithm more robust since the $f - \Delta\lambda$ behavior is unknown and can take any arbitrary shape. If none of these techniques is able to bound the root, an error message is issued and the analysis is terminated. In such a situation, reducing the time step may fix the problem.

2.2.5   Taylor-Quinney Effect

There can be increase in temperature in a material during a high strain rate deformation (Farren & Taylor, 1925; Taylor & Quinney, 1934). This happens when the plastic work is converted into heat during plastic deformation. This is of utmost importance in case of an impact scenario which would involve high strain rate response (Johnston et al., 2017, 2018; Konieczny, 2018) and a softening of the material around the point of impact. The rise in temperature due to plastic work is given by the following equation,

$$\Delta T = \frac{\beta_t}{c_p \rho} h \Delta\lambda \tag{2.40}$$

where, β_t is the Taylor-Quinney coefficient and c_p is the specific heat. These two parameters are required as input for computing the temperature increase.

3   FAILURE MODELING IN OEPDMM

Theoretical and implementation details of two failure criteria implemented in an orthotropic plasticity model are presented. The well-known Puck Failure criterion and a recently developed Generalized Tabulated Failure criterion are discussed and show how to link a failure sub-model to existing deformation and damage sub-models in the context of explicit finite element analysis.

3.1   Puck Failure Model

Puck's failure model is an action-plane based model for transversely isotropic UD fiber-reinforced composite lamina (Deushle, 2010; Deuschle & Kropline, 2012; Deuschle & Puck, 2012; Shyamsunder et al., 2020a, 2020b). Action plane refers to the plane that develops forces to resist the applied force. The theory considers two modes of failure separately - fiber fracture (FF) and inter-fiber fracture (IFF). Three stresses- σ_n (normal stress), τ_{nt} (shear stress transverse to the fiber direction) and τ_{n1} (shear stress in the direction of the fiber) act on the section plane, and govern the IFF, where the plane that is inclined at an angle of θ to the 3-direction represents the section plane (Figure 5).
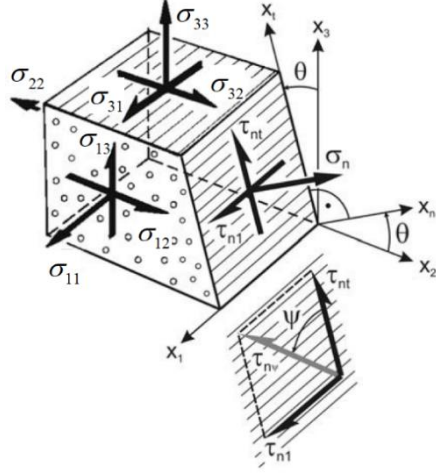
Figure 5. Stresses acting on the Action Plane (Deuschle & Puck, 2012)

These three stress quantities are derived from the stresses acting along the PMDs as,

$$\sigma_n = \sigma_{22} \cos^2 \theta + \sigma_{33} \sin^2 \theta + 2\sigma_{23} \sin\theta \cos\theta \qquad (3.1)$$

$$\tau_{nt} = -\sigma_{22} \sin\theta \cos\theta + \sigma_{33} \sin\theta \cos\theta + \sigma_{23}\left(\cos^2\theta - \sin^2\theta\right) \qquad (3.2)$$

$$\tau_{n1} = \sigma_{13} \sin\theta + \sigma_{12} \cos\theta \qquad (3.3)$$

The orientation of the fracture plane depends on the type of loading. For example, in the case of a pure normal tension loading (Figure 6(a)), the plane perpendicular to the loading direction is the action plane shown by the gray colored plane. For almost all unidirectional laminae, the fracture plane is parallel to the action plane for this loading condition (Figure 6(b)). On the other hand, for the case of pure shear loading transverse to the fiber direction, the action plane (Figure 6(c)) is not parallel to the fracture plane (Figure 6(d)). The inclination of the fracture plane is determined numerically in a

46

material model. The failure criterion for IFF is based on stresses acting on the fracture plane. The fracture in the lamina is assumed to take place when the stress exposure is equal to unity. Since there are two modes of failure, the stress exposure is also defined separately for the FF and IFF denoted as f_{EFF} and f_{EIFF}, respectively.
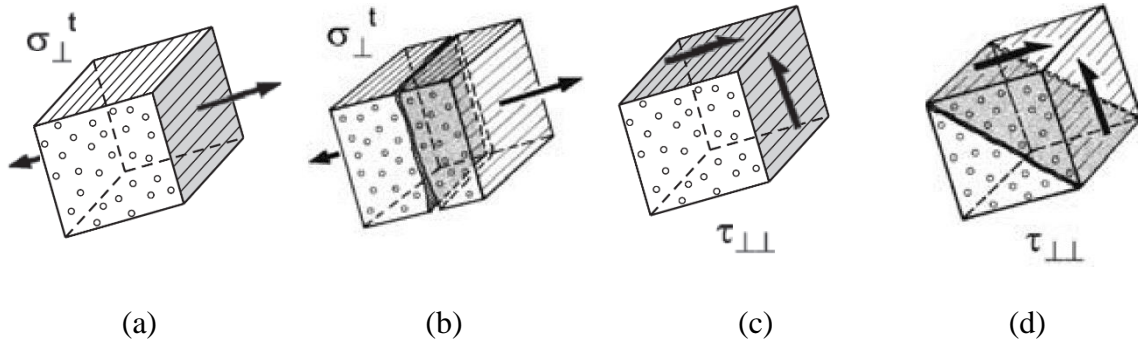
Figure 6. Transverse Single Tensile Stressing (a) Action Plane and the Corresponding (b) Fracture Plane. Pure Shear Stressing (c) Action Plane and the Corresponding (d) Fracture Plane (Deuschle & Kropline, 2012)

In the current work, after the failure criterion (onset of failure) is satisfied at an element's Gauss point, the stresses in the PMDs are gradually brought down to zero using smeared formulation techniques that have been used in other materials such as metals and concrete (Bazant & Oh, 1983). The idea is extended to laminated composites (Pinho et al., 2006b), and is used here with modifications. Puck theory also considers a reduction in IFF strength due to local micro-fractures in the 1-direction. This reduction in the IFF strength is taken care by additional parameters (Deuschle & Kropline, 2012). For example, η_{w1} takes care of the reduction in the IFF strength due to micro-fractures that are due to fiber

47

filaments failing before the FF criterion is satisfied. This arises from the fact that all the fiber filaments do not have uniform strength, and there is statistical variation in the strength of the filaments. The failure of these fiber filaments causes local damage and micro-fractures in the lamina thus reducing the resistance against IFF. Hence, the original f_{EIFF} is modified by scaling it by η_{w1}, where η_{w1} can vary between 0 to 1. This implies that the new f_{EIFF} will satisfy a value of unity sooner. η_{w1} is assumed to be a function of the stress in 1-direction and must be determined experimentally. Deuschle & Kroplin (2012) use an estimate of η_{w1} since adequate experimental data were not available. Another parameter which affects the IFF strength is η_{m+p} that takes care of the effect of non-fracture plane stresses on the IFF. The assumption is that due to micro-damages in the composite caused by flaws, fracture can occur in a plane other than the numerically estimated fracture plane. Hence, the stresses on the fracture plane that causes IFF can be lower than the computed one. To account for this effect, the strength parameters and the inclination parameters are modified based on η_{m+p} based on a function which depends on the standardized stress exposure (ratio of the stress exposure corresponding to an action plane to the stress exposure corresponding to the fracture plane). The effects of η_{w1} and η_{m+p} have not been considered in the current failure implementation based on the assumption that this behavior is taken care of by the deformation and the damage sub-models since the input to those two sub-models are obtained from experiments where the composite exhibits fiber micro-fractures and matrix micro-damages.

Similar to other failure theories (Hashin, 1980; Tsai & Wu, 1971), Puck theory also assumes a failure envelope in the IFF mode called the Master Fracture Body (MFB). A typical MFB is shown in Figure 7 that helps illustrate the use of the strength values as the anchoring points. The notation used for the strength parameters are shown in Table 3. Any strength parameter with a superscript *A* represents the strength in the action plane.

Table 3. Strength Parameters at Lamina Level

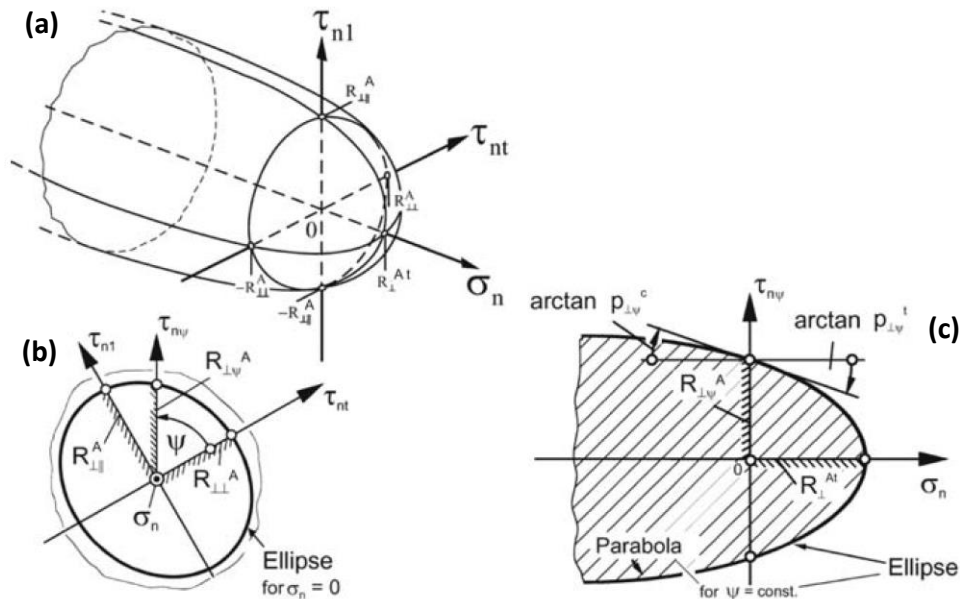| $R_\perp^{At}$	Tensile strength of the composite in the direction transverse to the fiber direction
$R_\perp^{c}$	Compressive strength of the composite in the direction transverse to the fiber direction
$R_{\perp\parallel}^{A}$	In-plane shear strength of the composite
$R_{\perp\perp}^{A}$	Transverse shear strength of the composite
$R_{\perp\psi}^{A}$	See Figure 7(b)

Figure 7. Master Fracture Body (MFB) in the Action Plane-Related Stress Space

(Deuschle & Kroplin, 2012)

49

The inclination parameters, $p_{\perp\psi}^{t,c}$, represent the slope of the master fracture body with respect to σ_n axis (see Figure 7(c)). These parameters are the slope of the Master Fracture Body at $\sigma_n = 0$. At $\psi = 90°$, $p_{\perp\psi}^{t,c} = p_{\perp\|}^{t,c}$, and $p_{\perp\|}^{t,c}$ are determined by generating the fracture body in the (σ_2, τ_{21}) space (Puck et al., 2002). In this case since the fracture plane angle is zero, the action plane stresses are the PMD stresses themselves, i.e. $\sigma_n = \sigma_2$ and $\tau_{n1} = \tau_{21}$. At $\psi = 0°$, $p_{\perp\psi}^{t,c} = p_{\perp\perp}^{t,c}$. However, $p_{\perp\perp}^{t,c}$ cannot be obtained directly from experiment - $p_{\perp\perp}^{c}$ is indirectly determined from transverse compression testing where the fracture angle can be measured, $p_{\perp\perp}^{t}$ is assumed to be the same as $p_{\perp\perp}^{c}$ since there is no established technique to obtain this, and $p_{\perp\|}^{t,c}$ and $p_{\perp\perp}^{t,c}$ are related to $p_{\perp\psi}^{t,c}$ for a given ψ using Eq. 3.17.

3.1.1 Stress Degradation Model

The state of stress in an element needs special attention when the failure criterion is satisfied at any one of the stress Gauss points. In the current work, a Stress Degradation Model (SDM) is implemented as an integral part of the Puck failure model and serves two purposes. First, the stresses in the PMDs are gradually brought down to zero in the post-peak regime to avoid numerical instabilities such as elastic snapback arising from stress redistribution to the adjacent elements (Belyschko et al., 2014). Second, the process to degrade the stresses should be mesh independent (Shyamsunder et al., 2020a). An earlier version of the Stress Degradation Model discussed in Shyamsunder et al. (2020a) has been modified. In the previous implementation, at the element Gauss point under

50

consideration, once failure onset is detected, the deformation and the damage calculations were skipped. The value of true stress corresponding to the failure onset was stored and was scaled down to compute the degraded stress. Sometimes this approach resulted in excessively elongated elements resulting in smaller critical time step, and thereby longer simulation run time. In the improved implementation presented here, the computations related to deformation and damage are carried out even after failure onset is detected. The effective stress is held constant, but the true stress is gradually reduced. This approach provides not only post-peak numerical stability but the ability to control the *residual strength* in the finite element. In the context of this dissertation, residual strength, c^{RS}, is expressed as a fraction of the peak stress that, and the element is eroded when the residual strength value is reached, i.e. $\sigma^f = c^{RS}\sigma^{\max}$, $0 \le c^{RS} \le 1.0$. This gradual degradation of stress is explained in Figure 8(a) with the corresponding effective damage parameter (c^d) shown in Figure 8(b). Let σ^0 and ε^0 represent the stress and strain values at failure onset, respectively. If the FF criterion is satisfied before the IFF criterion, only the stress in the 1-direction is degraded. It is assumed that the material has load carrying capacity in the 2-direction, 3-direction, 1-2 plane, 2-3 plane and 1-3 plane even after FF. The stress components other than the 1-direction stress are degraded only after the IFF criterion is satisfied. Conversely, if IFF is satisfied before FF, it is assumed that the composite has load carrying capacity in the 1-direction. Therefore, the stress is not degraded in the 1-direction till the FF criterion is satisfied. It should be noted that σ^0 is in the true stress space, whereas the corresponding effective stress counterpart is denoted as $\sigma^{eff,0}$. At the onset of failure, the initial value of effective damage parameter,

c_0^d, is computed from the damage parameter d_{kl}^{ij}. As can be seen in Figure 8(a), the effective stress is kept constant at $\sigma^{eff,0}$ since a non-negative slope of the effective stress is required by the plasticity algorithm. The true stress is brought down to the residual strength, σ^f, using the deformation and the damage sub-models with the corresponding strain value of ε^1. σ^f is computed based on the value of Post Peak Residual Damage ($PPRD$) and the corresponding effective damage parameter stays constant at $PPRD$ as shown in Figure 8(b). $PPRD$ is a user input parameter for PFC. The residual strength is maintained constant till the element is eroded at the erosion strain value of ε^f that is computed as

$$\varepsilon^f = \varepsilon^0 + \frac{2\Gamma}{\sigma^0 L} \tag{3.4}$$

where, Γ is the fracture energy in the mode under consideration, and L is the characteristic length of the finite element (taken as cube root of the volume of the element).
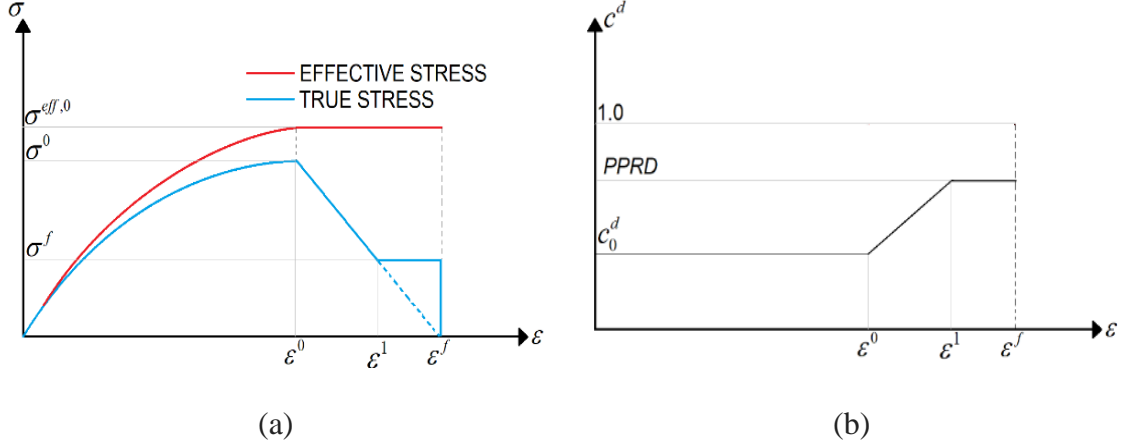
Figure 8. (a) Stress vs Strain Response using PFC (note $\sigma^{max} = \sigma^0$) (b) Effective

Damage Parameter vs Strain using PFC

Eq. 3.4 is based on the assumption that the area under the stress-strain curve between ε^0

and ε^f, ignoring the residual strength, corresponds to fracture energy. The use of the

characteristic length provides the mesh regularization feature in the failure sub-model.

The effective damage parameter after failure onset can be expressed as

$$
c^d = \begin{cases} \left(1 - c_0^d\right)\left(\dfrac{\varepsilon - \varepsilon^f}{\varepsilon^f - \varepsilon^0}\right) + 1 & \varepsilon^0 \leq \varepsilon \leq \varepsilon^1 \\[2ex] PPRD & \varepsilon > \varepsilon^1 \end{cases}
\tag{3.5}
$$

For $\varepsilon < \varepsilon^0$, c^d is computed using Eqs. 2.6, 2.7 and 2.9.

3.1.2 Implementation of Puck Failure Theory

Twenty parameters are used in PFC to detect failure onset, implement the SDM algorithm, and carry out element erosion. Most, not all, can be readily found from experiments. The tensile, compressive and shear strength parameters, $\{R_\parallel^t, R_\perp^{At}, R_\parallel^c, R_\perp^c, R_{\perp\parallel}^A\}$ can be obtained from experiments (Khaled et al., 2017). The procedure to determine the inclination parameters, $\{p_{\perp\parallel}^c, p_{\perp\parallel}^t, p_{\perp\perp}^t, p_{\perp\perp}^c\}$, is discussed in Puck et al., 2002. The magnification factor, m_{σ_f}, is used in the FF criterion and accounts for stress magnification in the fiber due to inhomogeneity in the matrix stress distribution in the vicinity of the fiber (Deuschle & Kroplin, 2012). In addition, in the FF criterion, the fiber Poisson's ratio, $\nu_{\parallel\perp f}$, and modulus of elasticity, $E_{\parallel f}$ are used (Kodagali et al., 2017). Next, the fiber direction fracture energy, Γ_f, can be determined through experiments (Pinho et al., 2006c). However, this value has been estimated in this dissertation since no experimental data is available for the composite. Mode I and Mode II interlaminar fracture energies, $\{\Gamma_I, \Gamma_{II}\}$, are determined through experiments (Khaled et al., 2019). In the absence of experimental data, the tension, compression and shear-related post-peak residual damage parameters, $\{PPRD_{T\parallel}, PPRD_{C\parallel}, PPRD_{T\perp}, PPRD_{C\perp}, PPRD_S\}$, are estimated values.

The algorithm used in PFC with the SDM implementation is as follows.

Input: The strain tensor for the current time step, stress tensor from the previous time step (true stress space), and failure-related parameters for a specific finite element. The

current failure state is also required as input and is one of the following – (a) the Gauss

point has not satisfied any of the failure criterion, or (b) the Gauss point has satisfied a

failure criterion and is undergoing post-failure stress degradation.

Output: Updated effective damage parameters and erosion status of the element.

Step 1.1(a): If the current point is not in FF failure state, update the stresses using the

effective damage parameters c_1^d and c_4^d (Eqs. 2.6 and 2.7).

Step 1.1(b): If the current point is in FF state, update the stresses using the following

effective damage parameters.

If $\sigma_{11} \geq 0$

$$c_{1,t}^d = c_{1,t-1}^d + \Delta c_{1,t}^d \ \ where \ \Delta c_{1,t}^d = \begin{cases} (1-c_{1,t-1}^d)\left(\dfrac{\left|\varepsilon_{11,t}\right|-\left|\varepsilon_{11,t-1}\right|}{\left|\varepsilon_{11}^f\right|-\left|\varepsilon_{11,t-1}\right|}\right) & \varepsilon_{11}^0 \leq \varepsilon_{11} \leq \varepsilon_{11}^1 \\ 0 & c_{1,t}^d > PPRD_{T\|} \end{cases} \tag{3.6}$$

else

$$c_{4,t}^d = c_{4,t-1}^d + \Delta c_{4,t}^d \ \ where \ \Delta c_{4,t}^d = \begin{cases} (1-c_{4,t-1}^d)\left(\dfrac{\left|\varepsilon_{11,t}\right|-\left|\varepsilon_{11,t-1}\right|}{\left|\varepsilon_{11}^f\right|-\left|\varepsilon_{11,t-1}\right|}\right) & \varepsilon_{11}^0 \leq \varepsilon_{11} \leq \varepsilon_{11}^1 \\ 0 & c_{4,t}^d > PPRD_{C\|} \end{cases} \tag{3.7}$$

where ε_{ij} are the strain tensor components. The subscript t is used to denote the current

time step.

55

Step 1.2(a): If the current point is not in IFF failure state, update the stresses using the effective damage parameters, c_2^d, c_5^d, c_3^d, c_6^d, c_7^d, c_8^d and c_9^d (Eqs. 2.6, 2.7 and 2.9).

Step 1.2(b): If the current point is in IFF state, update the stresses using the effective damage parameters as follows.

For i-direction normal components (i=2, 3):

If $\sigma_{ii} \geq 0$

$$c_{i,t}^d = c_{i,t-1}^d + \Delta c_{i,t}^d \quad where \; \Delta c_{i,t}^d = \begin{cases} (1-c_{i,t-1}^d)\left(\dfrac{\left|\varepsilon_{ii,t}\right|-\left|\varepsilon_{ii,t-1}\right|}{\left|\varepsilon_{ii}^f\right|-\left|\varepsilon_{ii,t-1}\right|}\right) & \varepsilon_{ii}^0 \leq \varepsilon_{ii} \leq \varepsilon_{ii}^1 \\ 0 & c_{i,t}^d > PPRD_{T\perp} \end{cases} \quad (3.8)$$

else

$$c_{i+3,t}^d = c_{i+3,t-1}^d + \Delta c_{i+3,t}^d \quad where \; \Delta c_{i+3,t}^d = \begin{cases} (1-c_{i+3,t-1}^d)\left(\dfrac{\left|\varepsilon_{ii,t}\right|-\left|\varepsilon_{ii,t-1}\right|}{\left|\varepsilon_{ii}^f\right|-\left|\varepsilon_{ii,t-1}\right|}\right) & \varepsilon_{ii}^0 \leq \varepsilon_{ii} \leq \varepsilon_{ii}^1 \\ 0 & c_{i+3,t}^d > PPRD_{C\perp} \end{cases} \quad (3.9)$$

For ij shear component (ij=12, 23, 13, k=7, 8, 9):

$$c_{k,t}^d = c_{k,t-1}^d + \Delta c_{k,t}^d \quad where \; \Delta c_{k,t}^d = \begin{cases} (1-c_{k,t-1}^d)\left(\dfrac{\left|\varepsilon_{ij,t}\right|-\left|\varepsilon_{ij,t-1}\right|}{\left|\varepsilon_{ij}^f\right|-\left|\varepsilon_{ij,t-1}\right|}\right) & \varepsilon_{ij}^0 \leq \varepsilon_{ij} \leq \varepsilon_{ij}^1 \\ 0 & c_{k,t}^d > PPRD_S \end{cases} \quad (3.10)$$

56

Step 2.1(a): If the current point is not in FF state, check FF criterion. FF onset is assumed to take place if the stress exposure, f_{EFF} , is equal to or greater than one (Deuschle & Kroplin, 2012):

$$f_{EFF} = \frac{\left|\sigma_{\parallel}^{eq}\right|}{R} \tag{3.11}$$

$$\sigma_{\parallel}^{eq} = \sigma_{11} - \left(v_{\parallel\perp} - v_{\parallel\perp f}\frac{E_{\parallel}}{E_{\parallel f}}m_{\sigma_f}\right)(\sigma_{22} + \sigma_{33}) \tag{3.12}$$

where

$$\begin{cases} R = R_{\parallel}^t, \text{ if } \sigma_{\parallel}^{eq} \geq 0 \\ R = R_{\parallel}^c, \text{ if } \sigma_{\parallel}^{eq} < 0 \end{cases} \tag{3.13}$$

When $f_{EFF} \geq 1$, compute the failure strain as

$$\varepsilon_{11}^f = \varepsilon_{11}^0 + \frac{2\Gamma_f}{\sigma_{11}^0 L} \tag{3.14}$$

Step 2.1(b): If the current point is in FF state, erode the element if one of the following criteria is satisfied:

(i) $\left|\varepsilon_{11}\right| \geq \left|\varepsilon_{11}^f\right|$

(ii) $\left(\sigma_{11}^0\right)\left(\sigma_{11}\right) < 0$

Step 2.2(a): If the current point is not in IFF state, check IFF criterion. IFF onset is assumed to take place if the stress exposure, f_{EIFF}, computed for $\theta = \theta_{fp}$, is equal to or greater than one using Eq. 3.15 (Deuschle & Kroplin, 2012). θ_{fp} is the orientation of the fracture plane with respect to the 3-direction. f_{EIFF} is computed by varying θ from $-90°$ to $90°$. The angle θ which yields the maximum value of f_{EIFF} is denoted θ_{fp}.

$$f_{EIFF} = \begin{cases} \sqrt{\left[\left(\dfrac{1}{R_\perp^{At}} - \dfrac{p_{\perp\psi}^t}{R_{\perp\psi}^A}\right)\sigma_n(\theta)\right]^2 + \left(\dfrac{\tau_{nt}(\theta)}{R_{\perp\perp}^A}\right)^2 + \left(\dfrac{\tau_{n1}(\theta)}{R_{\|\perp}^A}\right)^2} + \dfrac{p_{\perp\psi}^t}{R_{\perp\psi}^A}\sigma_n(\theta) & \sigma_n \geq 0 \\[4ex] \sqrt{\left(\dfrac{\tau_{nt}(\theta)}{R_{\perp\perp}^A}\right)^2 + \left(\dfrac{\tau_{n1}(\theta)}{R_{\|\perp}^A}\right)^2 + \left(\dfrac{p_{\perp\psi}^c}{R_{\perp\psi}^A}\sigma_n(\theta)\right)^2} + \dfrac{p_{\perp\psi}^c}{R_{\perp\psi}^A}\sigma_n(\theta) & \sigma_n < 0 \end{cases}$$

(3.15)

where

$$R_{\perp\perp}^A = \frac{R_\perp^c}{2\left(1 + p_{\perp\perp}^c\right)}$$

(3.16)

$$\left(\frac{p_{\perp\psi}^{t,c}}{R_{\perp\psi}^A}\right) = \left(\frac{p_{\perp\perp}^{t,c}}{R_{\perp\perp}^A}\right)\cos^2(\psi) + \left(\frac{p_{\perp\|}^{t,c}}{R_{\|\perp}^A}\right)\sin^2(\psi)$$

(3.17)

$$\cos^2(\psi) = \frac{\tau_{nt}^2}{\tau_{nt}^2 + \tau_{nl}^2}$$

(3.18)

When $f_{EIFF} = 1$, compute the following failure strains:

$$\varepsilon_{ij}^f = \varepsilon_{ij}^0 + \frac{2\Gamma_I}{\sigma_{ij}^0 L}, \, for \, ij = 22, 33$$

(3.19)

58

$$\varepsilon_{ij}^f = \varepsilon_{ij}^0 + \frac{2\Gamma_{II}}{\sigma_{ij}^0 L}, \; for \; ij = 12, 23, 13 \qquad (3.20)$$

Step 2.2(b): If the current point is in the IFF state, erode the element if at least one of the following criteria is satisfied:

(i) $\quad \left| \varepsilon_{ij,t} \right| \geq \left| \varepsilon_{ij}^f \right|, \; ij = 22, 33, 12, 23, 13$

(ii)
$$
\begin{cases}
if \; \sigma_{22}^0 \geq \sigma_{33}^0 \\
\quad \begin{cases}
if \; \left(\sigma_{22}^0 \geq 0 \; and \; \sigma_{22}^0 \geq F_S \, R_\perp^{At} \right) \\
or \; if \; \left(\sigma_{22}^0 < 0 \; and \; \sigma_{22}^0 \geq F_S \, R_\perp^c \right) \\
erode \; element \; if \; \sigma_{22}^0 \times \sigma_{22} < 0
\end{cases} \\
else \\
\quad \begin{cases}
if \; \left(\sigma_{33}^0 \geq 0 \; and \; \sigma_{33}^0 \geq F_S \, R_\perp^{At} \right) \\
or \; if \; \left(\sigma_{33}^0 < 0 \; and \; \sigma_{33}^0 \geq F_S \, R_\perp^c \right) \\
erode \; element \; if \; \sigma_{33}^0 \times \sigma_{33} < 0
\end{cases}
\end{cases}
$$

(iii)
$$
\begin{cases}
if \; \left(\sigma_{12}^0 \geq \sigma_{23}^0 \right) and \left(\sigma_{12}^0 \geq \sigma_{13}^0 \right) and \left(\sigma_{12}^0 \geq F_S \, R_{\parallel\perp}^A \right) \\
\quad \left\{ erode \; element \; if \; \sigma_{12}^0 \times \sigma_{12} < 0 \right. \\
else \; if \; \left(\sigma_{23}^0 \geq \sigma_{12}^0 \right) and \left(\sigma_{23}^0 \geq \sigma_{13}^0 \right) and \left(\sigma_{23}^0 \geq F_S \, R_{\perp\perp}^A \right) \\
\quad \left\{ erode \; element \; if \; \sigma_{23}^0 \times \sigma_{23} < 0 \right. \\
else \; if \; \left(\sigma_{13}^0 \geq \sigma_{12}^0 \right) and \left(\sigma_{13}^0 \geq \sigma_{23}^0 \right) and \left(\sigma_{13}^0 \geq F_S \, R_{\parallel\perp}^A \right) \\
\quad \left\{ erode \; element \; if \; \sigma_{13}^0 \times \sigma_{13} < 0 \right.
\end{cases}
$$

Sometimes after an element is eroded, the neighboring elements undergoing stress degradation process may experience sudden changes in the strain field due to stress redistribution. This may lead to undesirable stress oscillations (stress reversals) taking place in a very short duration of time. Criteria (ii) and (iii) in Step 2.2(b) erode the

elements in which stress reversal with respect to the stress at the failure onset takes place. Since PFC assumes transverse isotropy, care needs to be taken which stress component (σ_{22} or σ_{33}) has to be chosen to keep track of stress reversal. This is taken care by the criterion in (ii). Similar strategy is used for the shear components. F_S is used here to ensure that the elements in which the stress components are oscillating are eroded. Numerical experimentation has shown that a value of $F_S = 0.8$ has worked reasonably well and is currently used for all the verification and validation tests presented in this dissertation.

Although Puck failure theory has been considered one of the better models in WWFE-I and WWFE-II (Hinton et al., 2004; Kaddour & Hinton, 2012), there are limitations that should be noted. First, the theory is valid for transversely isotropic material at the lamina level. Second, the Master Fracture Body is not a closed envelope (Deuschle & Kroplin, 2012). Third, the failure criteria are not functions of rate and temperature. This is important for unidirectional polymeric composites that exhibit rate and temperature sensitivities and form the impacted structural system.

3.2   Generalized Tabulated Failure Model

A failure model where an arbitrarily shaped failure surface in the stress space can be used to predict the failure of a composite is highly desirable. One would expect the failure surface of a composite to be complex such that a mathematical expression cannot be defined and used as is done with traditional failure criteria (Hashin, 1980; Tsai & Wu,

1971). In the earlier version of GTFC (Goldberg et al., 2018b), the in-plane, the out-of-plane and the combined in-and-out-of-plane failure states were defined in terms of stresses. The current version of GTFC assumes that failure states are strain rather than stress-based so that post-peak behavior can be handled seamlessly. Failure surfaces need to be defined for each of these failure states in the equivalent failure strain and failure angle space (Shyamsunder et al., 2019).
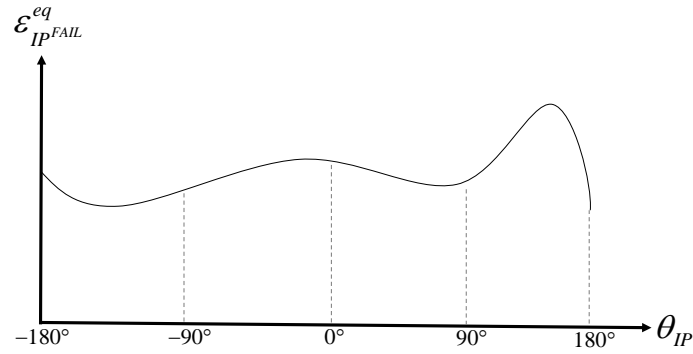

Figure 9. General form of In-Plane Failure Surface.

Figure 9 shows the in-plane failure surface where $\varepsilon_{IP^{FAIL}}^{eq}$ is a function of the failure angle, θ_{IP}, and can take any shape depending on the composite properties. The equivalent strain, ε_{IP}^{eq} and failure angle, θ_{IP} are computed for each time step and element Gauss point as

$$\varepsilon_{IP}^{eq} = \sqrt{\varepsilon_{11}^2 + \varepsilon_{22}^2 + 2\varepsilon_{12}^2} \tag{3.21}$$

$$\theta_{IP} = \cos^{-1}\left(\frac{\sigma_{22}}{\sqrt{\sigma_{22}^2 + \sigma_{12}^2}}\right) \tag{3.22}$$

61

Note that the failure angle is expressed in terms of σ_{22} and σ_{12} as in unidirectional composites, the stress in the 1-direction, σ_{11}, is usually of a magnitude higher than σ_{22} and σ_{12}. Using σ_{11} in the computation of the failure angle (Goldberg et al., 2018b) instead of using σ_{12} may make the points on the failure surface agglomerate as illustrated in Figure 10 where most of the data points are concentrated at θ_{IP} values of $-180°$, $0°$ and $180°$. This is not desirable since the interpolation between unequally spaced points may yield inaccurate equivalent failure strain values.
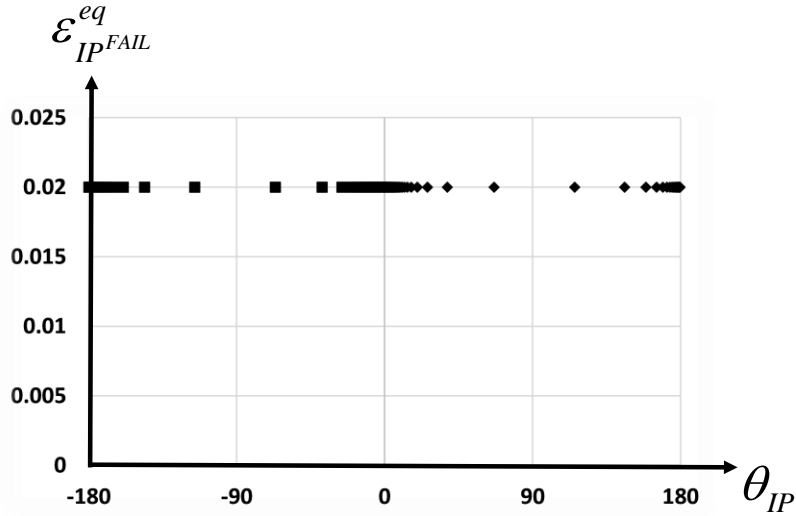

Figure 10. In-Plane Failure Surface where Failure Angle is Computed using σ_{11}

Let the in-plane failure state e_1 be computed as

$$e_1 = \frac{\varepsilon_{IP}^{eq}}{\varepsilon_{IP^{FAIL}}^{eq}} \tag{3.23}$$

An out-of-plane failure surface can be constructed similar to Figure 9 with the failure surface expressed in terms of $\varepsilon_{OOP^{FAIL}}^{eq}$ as a function of θ_{OOP} for a given σ_{33}. ε_{OOP}^{eq} and θ_{OOP} are computed for each time step and element Gauss point as

$$\varepsilon_{OOP}^{eq} = \sqrt{\varepsilon_{33}^2 + 2\varepsilon_{13}^2 + 2\varepsilon_{23}^2} \qquad (3.24)$$

$$\theta_{OOP} = \cos^{-1}\left(\frac{\sigma_{13}}{\sqrt{\sigma_{13}^2 + \sigma_{23}^2}}\right) \qquad (3.25)$$

Similarly, the out-of-plane failure state e_2 is computed as

$$e_2 = \frac{\varepsilon_{OOP}^{eq}}{\varepsilon_{OOP^{FAIL}}^{eq}} \qquad (3.26)$$

An element is eroded if $e \geq 1$ where

$$e = \begin{cases} \max(e_1, e_2) & \text{if } n = 0 \\ \sqrt[n]{(e_1)^n + (e_2)^n} & \text{if } n > 0 \end{cases} \qquad (3.27)$$

where n is a user defined interaction parameter that can be used to couple the in-plane state of stress/strain to the out-of-plane state of stress/strain. GTFC requires two sets of tabulated input - the equivalent failure strain and the corresponding failure angle for in-

63

plane $\left(\varepsilon_{IP^{FAIL}}^{eq},\theta_{IP}\right)$ and the out-of-plane $\left(\varepsilon_{OOP^{FAIL}}^{eq},\theta_{OOP}\right)$ failure modes. In this dissertation, these values are based on data obtained from uniaxial testing (Khaled et al., 2017), though it is desirable to generate a richer set of data either via biaxial/triaxial laboratory tests or virtual testing that has the potential to generate rich and reliable data. A minimum of 21 parameters (9 stress-strain curves that are augmented with post-peak data, 9 uncoupled damage parameter curves, set of in-plane $\left(\varepsilon_{IP^{FAIL}}^{eq},\theta_{IP}\right)$ values and set of out-of-plane $\left(\varepsilon_{OOP^{FAIL}}^{eq},\theta_{OOP}\right)$ values, and n) are used in GTFC to compute the post-peak response including element erosion.

3.2.1   Stress Degradation Model

Unlike PFC, GTFC does not require failure onset to be detected to compute the post-peak response. Each input stress-strain curve has pre-peak and post-peak regions that are used to capture the peak stress via the deformation and damage sub-models, and handle the post-peak behavior via the damage sub-model similar to what is done with the stress degradation model in PFC. Figure 11(a) shows a typical stress-strain input curve for a given component. The portion of the stress data between ε^0 and ε^1 can be artificially generated if experimental data does not exist or is not available. Note that $c_i^{RS}, i=1,..,6$ for the normal tensile (1-3)/compressive (4-6) stresses in the PMDs, $c_i^{RS}, i=7,8,9$ for the three principal shear components. For the deformation sub-model to carry out the plasticity-related computations, the input stress in the effective stress space cannot have a negative slope. To ensure that this condition is satisfied, an effective damage parameter

64

curve is used as input (Figure 11(b)). This damage parameter data is computed for the respective component by keeping the effective stress constant and equal to the peak effective stress. The uncoupled damage parameter is the same as the effective damage parameter as no coupled-damage parameters are used in the post-peak calculations.
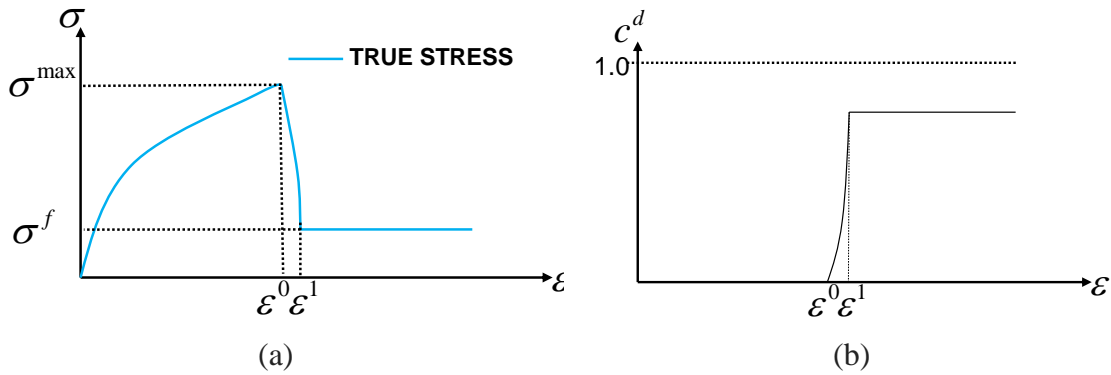

(a)   (b)

Figure 11. (a) Stress-Strain Input Augmented with Post-Peak Data (note $\sigma^{max} = \sigma^0$) (b)

Effective Damage Parameter Input for Handling Post-Peak Behavior.

3.2.2   Implementation of GTFC

The algorithm used in GTFC is as follows.

Input: The strain tensor for the current time step, stress tensor from the previous time step which are in the true stress space, and failure-related parameters.

Output: Element erosion status.

Step 1: For a given time step, update the element Gauss point stress tensor using the deformation and the damage sub-models.

Step 2.1: Compute ε_{IP}^{eq} and θ_{IP} using Eqs. 3.21 and 3.22. Using the interpolation function, obtain $\varepsilon_{IP^{FAIL}}^{eq}$ corresponding to the computed θ_{IP}.

Step 2.2: Compute e_1 using Eq. 3.23.

Step 3.1: Compute ε_{OOP}^{eq} and θ_{OOP} using Eqs. 3.24 and 3.25. Using the interpolation function, obtain $\varepsilon_{OOP^{FAIL}}^{eq}$ corresponding to the computed θ_{OOP}.

Step 3.2: Compute e_2 using Eq. 3.26.

Step 4: Compute e using Eq. 3.27. Erode the element if $e \geq 1$.

Like PFC, the current implementation of GTFC is also not rate and temperature dependent. Obtaining experimentally a rich set of failure surface data is neither easy nor feasible with the current state-of-the-art. The combination of experimental testing along the principal material directions and virtual testing for combined state of stress appears to be a viable option. To alleviate this problem, in this work, the in-plane and out-of-plane responses are computed separately and then combined via the interaction term, n.

4 VERIFICATION AND VALIDATION OF FAILURE MODELS

Verification and validation (V&V) are an integral part of any material model development. The verification tests ensure that the implementation is done correctly. Verification testing can start with as simple as single element tests, whereas the validation tests are used to gage the fidelity and reliability of the developed material model. V&V discussed in this section are based on carbon/epoxy unidirectional composite, T800/F3900 (Toray Carbon Fibers America, 2020). While details of V&V can be found in prior publications (Hoffarth, 2016; Hoffarth et al., 2017, 2020; Khaled et al., 2018, 2019; Shyamsunder et al., 2020a, 2020b), in this chapter a few select cases are used to illustrate the process and discuss the results.

Experiments have been carried out at ASU and The Ohio State University (OSU) to characterize T800/F3900 and obtain parameters to drive OEPDMM. Test coupons have been used to obtain the stress-strain curves in 1-direction tension (T1), 2-direction tension (T2), 3-direction tension, 1-direction compression, 2-direction compression (C2), 3-direction compression (C3), 1-2 plane shear, 2-3 plane shear, 1-3 plane shear, 1-2 plane 45° off-axis tension, 2-3 plane 45° off-axis compression, and 1-3 plane 45° off-axis compression under quasi-static room-temperature (QS-RT)conditions as ASU (Khaled et al., 2017, 2020). At OSU, experiments have been carried out at strain rates higher than the quasi-static rates to obtain the stress-strain data in 2-direction tension at 0.001/s and 325/s, 2-direction compression at 0.001/s, 1/s and 813/s, and 3-direction compression at 800/s (Deshpande et al., 2019). The legends in the graphs in this chapter: (a) *QS-RT*

refers to testing carried out at quasi-static ($\sim 10^{-4}$/s), room temperature conditions, (b) *Model (QS-RT)* or *Model* refers to the curve generated from the average values obtained from at least 3 different test replicates and used as input to the constitutive model, (c) *Exp (X/s)* refers to experimental data from one test coupon at strain-rate of X/s and used as input to the constitutive model, and (d) *Experiment* refers to the experimental data used for validation.

Single element tests carried out to highlight each one of the features discussed in Chapter 2 are presented in Section 4.1. In all the single element finite element (FE) schematics, the Principal Material Directions (PMDs) are marked within the cube with the fiber direction represented by a green line. The slashed red color arrows represent a restraint along the direction of the arrow. All the translational displacements are retrained at the pin support. The black color arrows represent a prescribed displacement. This is followed by V&V for the implemented failure sub-models discussed in Chapter 3. In Section 4.2, the V&V results from simulations run using only the QS-RT stress-strain curves (Khaled et al., 2017) are presented. These include single element verification tests each for both PFC and GTFC to illustrate the significance of the respective failure parameters. Validation is carried out using a stacked-ply composite panel subjected to a quasi-static loading and ballistic impact tests, where both PFC and GTFC are exercised. Additional validation test results can be found in Shyamsunder et al. (2020a). Rate-dependent features of OEPDMM and its integration with GTFC is presented in Section 4.3 using a set of ballistic impact validation tests (Deshpande et al., 2019).

4.1 Single Element Verification using only the Deformation Sub-model

4.1.1 Strain-rate Smoothing

Background: The verification of OEPDMM with the strain-rate smoothing feature is done with T800/F300 unidirectional composite (Toray Carbon Fibers America, 2020). The stress-strain curves obtained from experiments (Khaled et al., 2017) are used to drive OEPDMM deformation sub-model (damage and failure sub-models are de-activated).

Finite Element Modeling: A single element 1-direction tension test model is considered where an eight-noded hexahedron element is used (Figure 12). The displacement is applied to induce a strain-rate of approximately 1/s.

Results: The strain-rate obtained in the normal components for different values of s are shown in Figure 13 where *T1*, *C2* and *C3* represent the strain-rate in the 1-direction tension, 2-direction compression and 3-direction compression components, respectively.
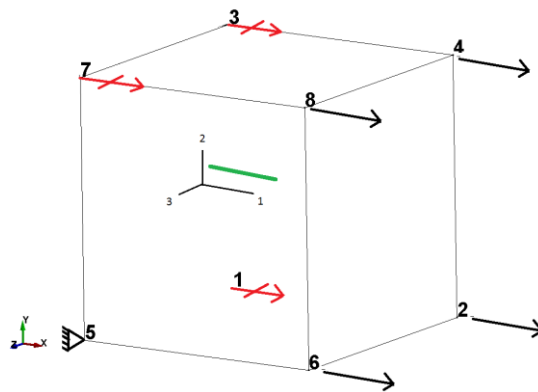

Figure 12. 1-Direction Tension Single Element Schematic

69

Discussions: The oscillations in the 2 and the 3-direction compression components decrease as the value of s increases. Typically, a small value is used only if necessary, with larger values used to control noisy behavior and promote numerical stability.
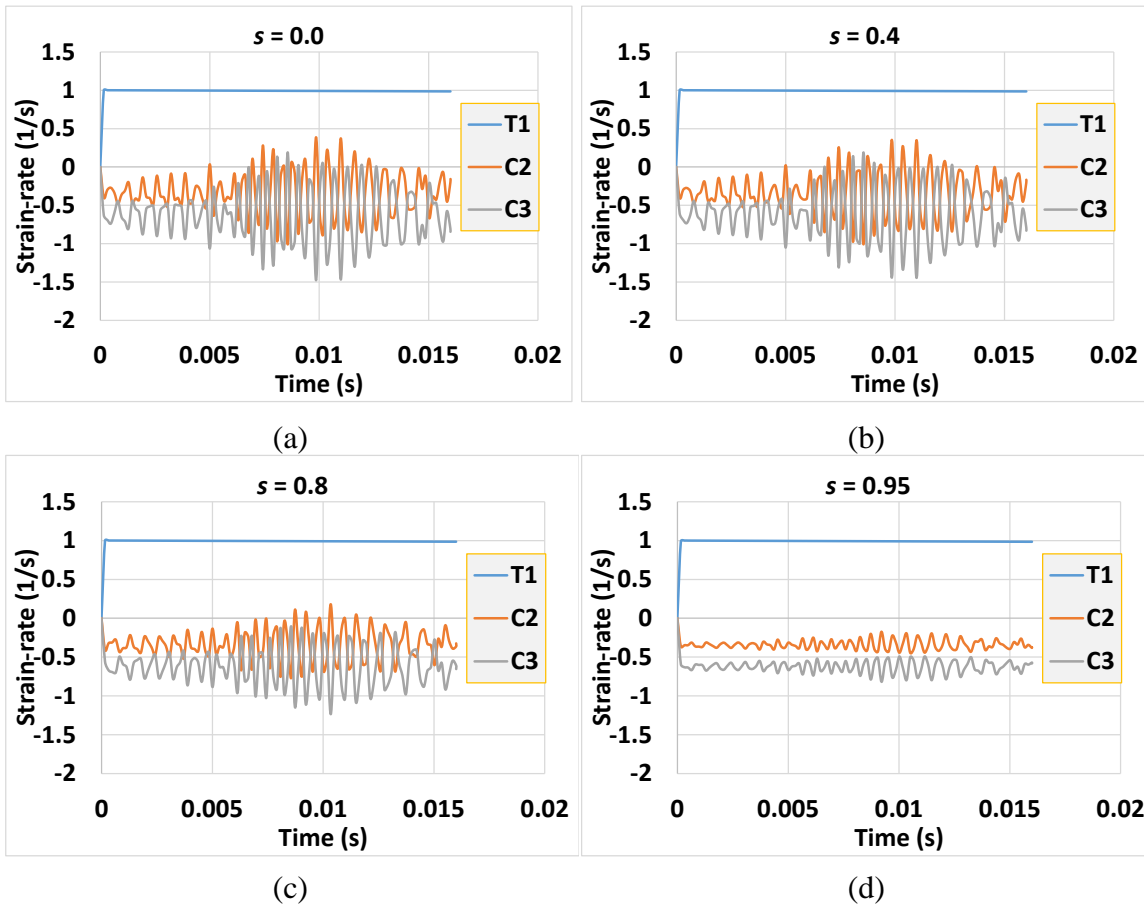

(a)   (b)

(c)   (d)

Figure 13. 1-Diretion Tension Test Strain-Rates in the Three Normal Components for (a)

$s = 0$ (b) $s = 0.4$ (c) $s = 0.8$ (d) $s = 0.95$

4.1.2 Stress-relaxation

Background: The verification of visco-elastic-plastic feature is demonstrated using a stress-relaxation example (Toray Carbon Fibers America, 2020). The QS-RT stress-strain

70

curves (Khaled et al., 2017) are used in the deformation sub-model with the damage and failure sub-models de-activated. In addition, 2-direction compression stress-strain obtained at 1300/s strain-rate is used.

Finite Element Modeling: Figure 14 shows the FE model. A constant compressive strain rate of approximately 1300/s is induced due to the applied displacement till the strain in the element in the 2-direction reaches a value of ~0.04. Thereafter, the strain is held constant at a value of ~0.04 in compression as shown in Figure 15(a).
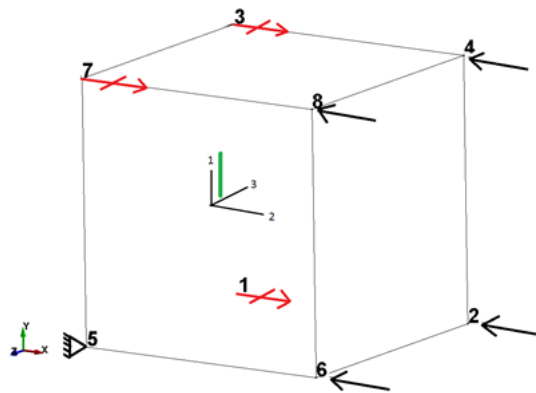

Figure 14. 2-Direction Compression Single Element Schematic

Results: The stress from the simulation is shown in Figure 15(b). *MAT213 (1300/s)* represents the stress-strain response obtained from simulation using OEPDMM in Figure 15(c). The 2-direction compression strain-rate and the effective plastic strain rate with respect to time from the simulation are in Figure 15(d).
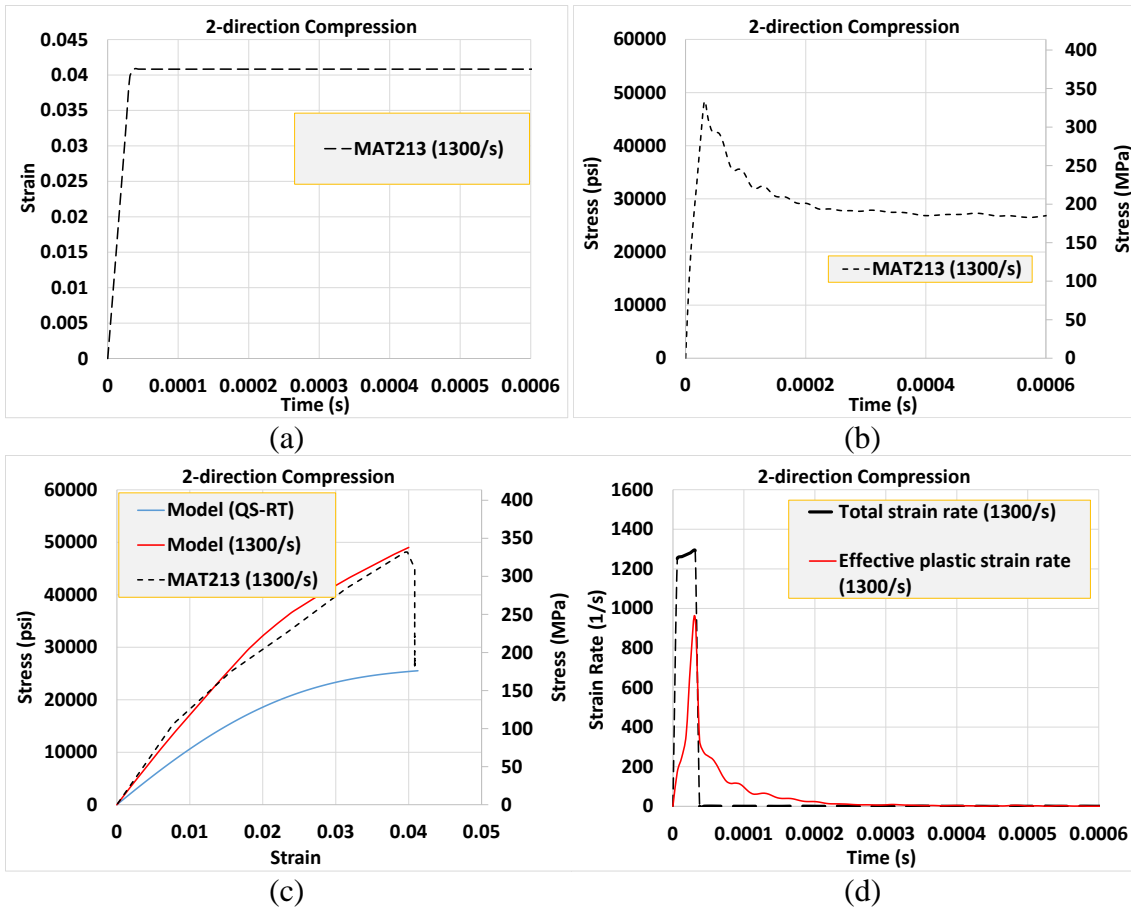
Figure 15. 2-Direction Compression Test Results: (a) Loading Strain-Time History (b) Computed Stress-Time History (c) Input Stress-Strain Curves and Computed Response (d) Computed Rate-Time History

Discussions: The stress gradually reduces to the "peak stress of the QS-RT curve" and stays constant after the strain is held constant. This is because the effective plastic strain rate gradually goes to zero, and so the interpolated flow stress used for the plasticity computation corresponds to the input stress-strain curve with the lowest effective plastic strain rate (QS-RT curve in this case). It should be noted that a sudden drop in the stress value is avoided since the interpolation of the stresses are done using the total strain rate

rather than the effective plastic strain rate (Hoffarth et al., 2016). The sudden drop in the stress is not realistic and would have caused numerical instability.

4.1.3 Taylor-Quinney Effect

Background: The Taylor-Quinney effect verification test case is carried out using synthetic data as there is no experimental data available for the specific heat (C_p) and the Taylor-Quinney coefficient (β_t) for T800/F3900 composite. Specific heat is taken for a similar composite (Achstetter, 2019) and three different values of β_t have been used ($\beta_t = 0.0, 0.75, 1.0$). In Figure 16(a), *Model (20 °C)* is the data obtained from ASU QS-RT test (Khaled et al., 2017). "*Model (30 °C)* and *Model (40 °C)* use synthetic data obtained by scaling down the *Model (20 °C)* curve after the yield point.
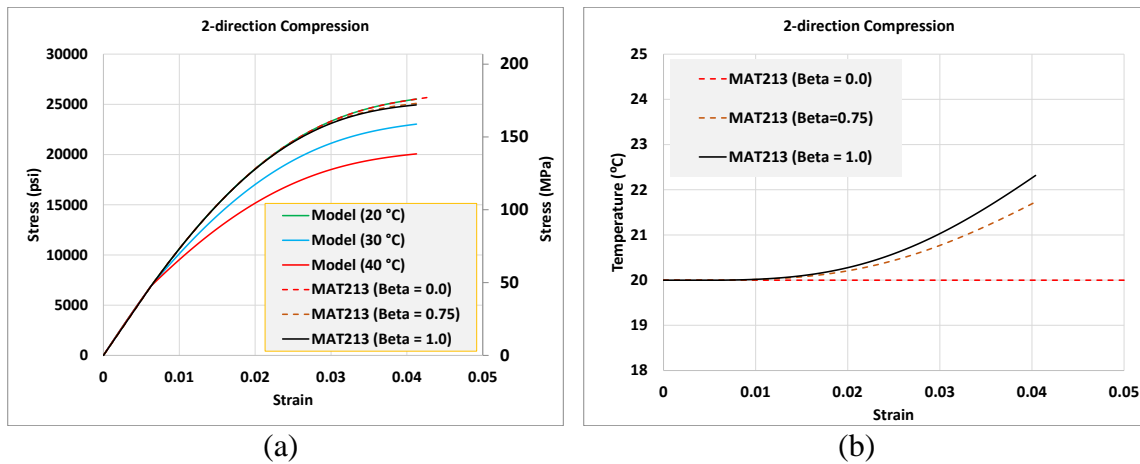

(a)   (b)

Figure 16. 2-Direction Compression Test Results: (a) Stress-Strain Response (b) Temperature-Strain Curve

Results: Figure 16(a) shows the stress-strain curves obtained from simulation for different values of β. Figure 16(b) shows the corresponding temperature profile plotted against time. The reference temperature is 20˚C. Figure 17 shows the stress vs plastic strain from the simulation using $\beta = 1.0$.
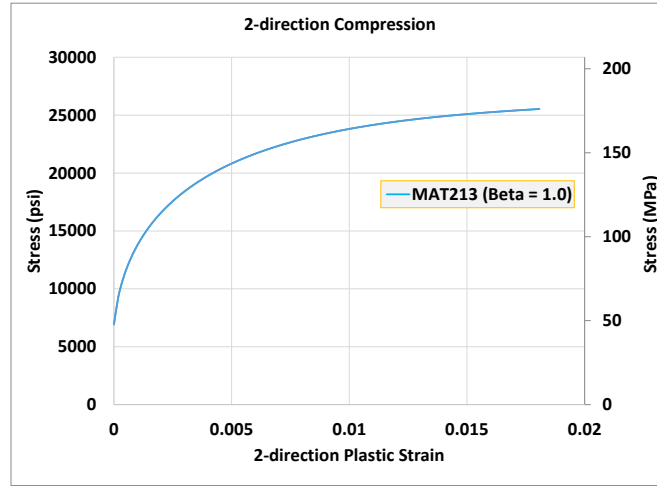

Figure 17. 2-Direction Compression Test Results – Stress-Plastic Strain

Discussions: The rise in temperature for the case where $\beta = 1.0$ is verified using the analytical equation (Eq. 2.40). The plastic work done is obtained from the area under the stress-plastic strain curve:

$$\Delta T = \frac{\Delta W^P}{C_p \rho}$$

$$\Rightarrow \Delta T = \frac{397 \dfrac{lb-in}{in^3}}{1.2 \times 10^6 \dfrac{in^2}{s^2 K} \times 1.4521 \times 10^{-4} \dfrac{lb-s^2}{in^4}}$$

$$\Rightarrow \Delta T = 2.27 K$$

74

As evident from the temperature-strain graph for the case with $\beta = 1.0$, the rise in temperature is about 2.30 K.

4.2   PFC and GTFC Rate-Independent V&V

General Details: This V&V for PFC and GTFC utilizing only the QS-RT stress-strain curves (Khaled et al., 2017) as input are shown. Experiments show that the composite exhibits brittle failure with little or no post-peak strength (Khaled et al., 2020). One-element verification tests are used to explain the implementation nuances of both the failure sub-models. Two validation tests are used to determine the efficiency and accuracy of the failure theories – a stacked-ply test carried out at ASU with loading in the quasi-static regime, and a high-velocity impact test carried out at NASA-GRC. Three different mesh sizes have been used for the stacked-ply validation tests – coarse, medium, and fine with increasing mesh densities to study mesh dependencies and convergence properties. In the impact validation tests, cohesive zone elements (CZE) have been used for modeling the delamination behavior and the details can be found in an earlier publication (Khaled et al., 2019).

PFC Parameters: The same input parameters used in a previous research (Shyamsunder et al., 2020a) are used here: $R_{\parallel}^{t} = 366100 \, psi \, (2524 \, MPa)$, $R_{\perp}^{At} = 6500 \, psi \, (44.8 \, MPa)$, $R_{\parallel}^{c} = 106000 \, psi \, (731 \, MPa)$, $R_{\perp}^{c} = 25500 \, psi \, (176 \, MPa)$, $R_{\perp\parallel}^{A} = 18600 \, psi \, (128 \, MPa)$, $p_{\perp\parallel}^{c} = 0.30$, $p_{\perp\parallel}^{t} = 0.35$, $p_{\perp\perp}^{t} = 0.25$, $p_{\perp\perp}^{c} = 0.30$, $v_{\parallel\perp} = 0.0168$, $v_{\parallel\perp f} = 0.2$, $m_{\sigma_{f}} = 1.1$,

75

$$\Gamma_f = 400\,lb/in\left(7{\times}10^4\,N/m\right), \quad \Gamma_I = 2.15\,lb/in\left(376\,N/m\right), \quad \Gamma_{II} = 10.4\,lb/in\left(1821\,N/m\right),$$

$E_{\parallel} = 2.37{\times}10^7\,psi\left(158\,GPa\right)$ in tension, $E_{\parallel} = 1.7{\times}10^7\,psi\left(117\,GPa\right)$ in compression, and

$E_{\parallel f} = 1.8{\times}10^7\,psi\left(124\,GPa\right)$. The only new input parameters are the $PPRD$ parameters whose values are estimated. First, it is assumed that there is no residual strength in tension and shear based on the observations made from the uniaxial stress experiments conducted on T800/F3900 composite specimens that are loaded until failure (Khaled et al., 2017). Second, $PPRD_{C\parallel}$ is estimated assuming the compressive strength in the 1-direction after the failure onset is approximately equal to the compressive strength in the 2-direction and there is a 50% residual strength in the transverse compressive direction. Composite panels still have some load carrying capacity after failure onset since the loading is in compression. In summary, unless otherwise stated, the following values are used in the FE models: $PPRD_{T\parallel} = 0.99$, $PPRD_{C\parallel} = 0.255$, $PPRD_{T\perp} = 0.99$, $PPRD_{C\perp} = 0.5$, and $PPRD_S = 0.99$.

GTFC Parameters: For all the simulations, it has been assumed that the compression residual strength parameters are equal to the respective peaks in the stress-strain input curves, $c_i^{RS} = 1.0, i = 4,5,6$. The residual strength used for the tension and the shear components are discussed for each test case separately. The equivalent failure strain is a constant function of the failure angle for both the in-plane and the out-of-plane modes. In the absence of experimental data, it is assumed that $\varepsilon_{IP^{FAIL}}^{eq} = \varepsilon_{OOP^{FAIL}}^{eq}$. The interaction term,

76

n is taken as 2 thereby coupling the in-plane and the out-of-plane states of stress that is to be expected in an impact event.

Numerical Calibration of Failure-related Parameters: As stated earlier, there are numerous failure-related parameters that can be calibrated to achieve better predictions. Amongst all failure-related parameters, the following parameters are used to improve the finite element predictions via a few trial-and-error runs: PFC: $R_{\parallel}^c$, Γ_f, Γ_I, Γ_{II},

$PPRD_{T\parallel}$, $PPRD_{C\parallel}$, $PPRD_{T\perp}$, $PPRD_{C\perp}$, and $PPRD_S$. GTFC: $c_i^{RS}, i=1,..,9$, $\varepsilon_{IPFAIL}^{eq}, \varepsilon_{OOPFAIL}^{eq}$.

Nomenclature: The following nomenclature is used in the numerical example graph legends: (a) *MAT213-GTFC* and *MAT213-PFC* imply that the simulation is run with GTFC and PFC, respectively, (b) the post-fixes *-F*, *-M* and *-C* imply that the simulation is run with fine, medium and coarse mesh model, respectively, (c) the post-fix *-Modified Strength* implies that one or more failure-related values have been calibrated, (d) for all *MAT213-PFC* simulations, and (f) for all the *MAT213-GTFC* simulations, *Model* implies that calibrated post-peak stress-strain data is added to the experimentally obtained pre-peak QS-RT data.

4.2.1 PFC Single Element Verification Test

Background: One single-element example (T2) is discussed to illustrate the SDM implementation. The test is executed with two different sets of input parameters that

influence the post-peak behavior (Table 4). Γ_{II} shown in Set 2 column is a fictitious

value and is used to show the significance of the parameter.

Table 4. Input Parameters for Verification

Component	Set 1	Set 2
$PPRD_{T\perp}$	0.5	0.7
Γ_{II}	10.4 lb/in (1821 N/m)	40.4 lb/in (7074 N/m)

Finite Element Modeling: The model involving the 8-noded hexahedral element is shown

in Figure 18. The boundary conditions are applied in order to obtain a uniaxial state of
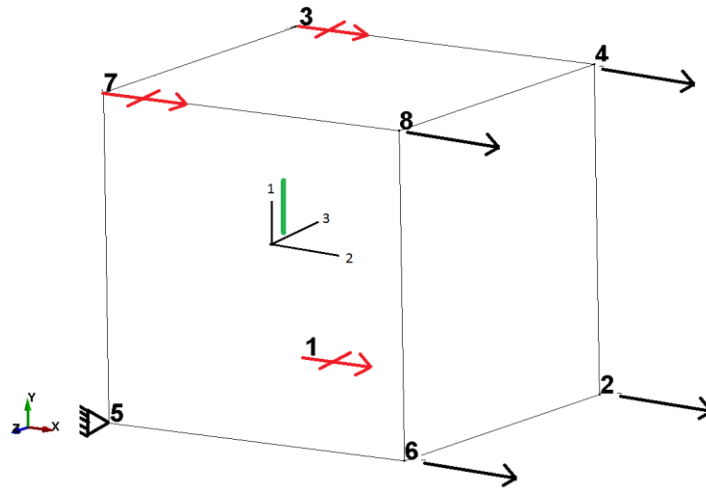
stress in the 2-direction.

Figure 18. 2-Direction Tension Single Element Schematic

Results: The *Model* curve as well as the stress-strain response of the FE models are shown in Figure 19 where the effective damage parameter is shown using the secondary axis.

Discussions: The pre-peak stress-strain responses remain the same for Set 1 and Set 2. The difference is observed in the post-peak regime. Larger the value of Γ_{II}, the larger is the area covered under the curve in the post-peak regime. It can also be observed that, smaller the value of $PPRD_{T\perp}$, the larger the residual strength.
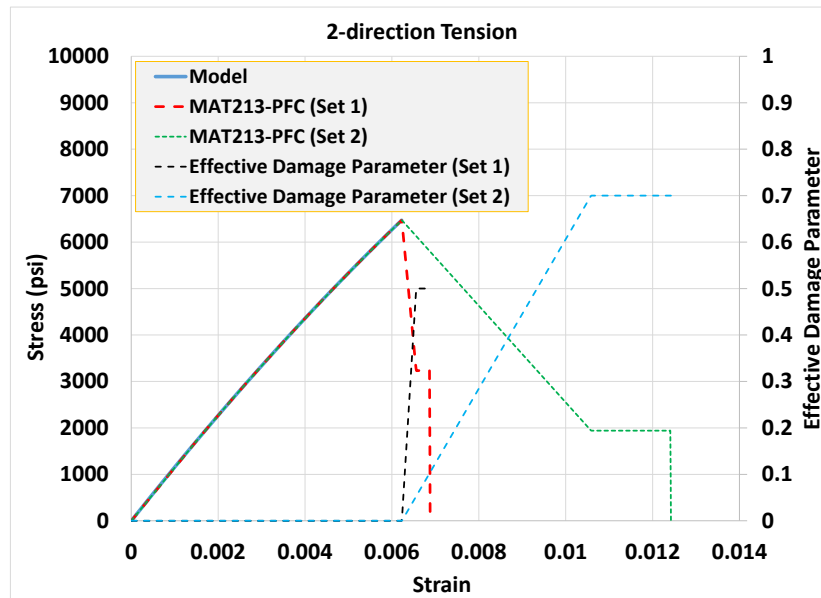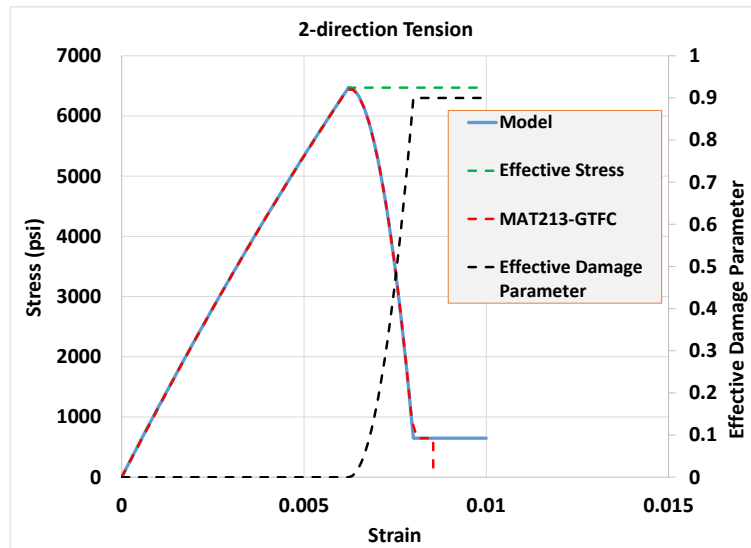

Figure 19. PFC Input and Results: 2-Direction Tension Test Stress and Effective Damage Parameter vs Strain Response.

4.2.2 GTFC Single Element Verification Test

Background: This test is the same single element test used with PFC, but now executed with GTFC.

(a)
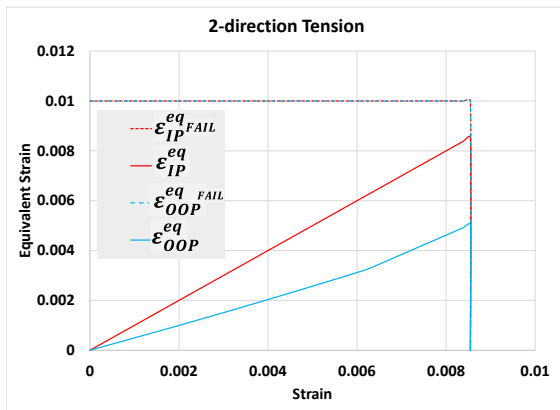
(b)

(c)
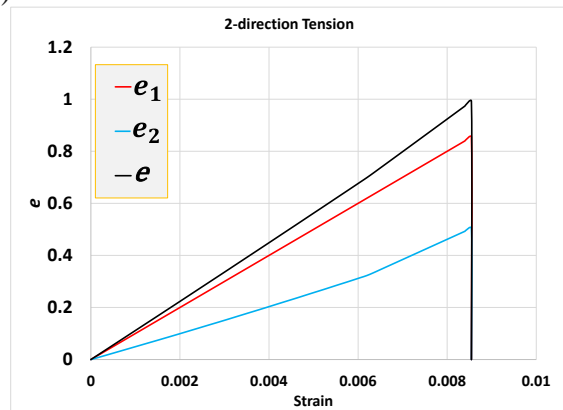
Figure 20. GTFC Input and Results: 2-Direction Tension Test (a) Stress and Effective

Damage Parameter vs Strain Response (b) Equivalent Strain vs Strain (c) e, e_1 and e_2

vs Strain

Finite Element Modeling: Figure 20(a) shows an additional post-peak regime in the *Model* curve. The stress-strain data in the pre-peak regime is obtained from experiments whereas the post-peak regime contains synthetic data that is used to control the post-peak stress degradation behavior. The figure also shows the *effective damage parameter* curve which increases from 0.0 to a value of 0.9 (see secondary axis), and the corresponding e*ffective stress* which remains constant. The residual strength in all the tension and the shear component is 10% of the respective peaks in the stress-strain input curve. The values of $\varepsilon^{eq}_{IP,FAIL} = 0.01$ and $\varepsilon^{eq}_{OOP,FAIL} = 0.01$ are calibrated values that are obtained with the objective to ensure that the element erodes after stress degradation.

Results: The drop in the stress value at a strain of ~0.008 is because of element erosion. Figure 20(b) shows ε^{eq}_{IP} and ε^{eq}_{OOP} increasing with respect to the 2-direction strain with the same trend as e_1 and e_2 shown in Figure 20(c), respectively.

Discussions: The simulation stress-strain response matches the *Model* curve in both the pre-peak and the post-peak regimes. As is evident from Figure 20(c), the element is eroded when $e = 1$.

4.2.3 Validation using Stacked-Ply Composite subjected to Quasi-Static Loading Condition

Background: The first set of validation tests is done using stacked-ply specimens consisting of 8 plies with a lay-up of [0/90/45/-45]$_s$ as shown in Figure 21. Two different

tests are carried out – (a) specimen subjected to tension in the y-direction, and (b) specimen subjected to compression in the y-direction. The grey colored region represents the portion of the specimen containing glass fiber tabs and gripped in the test fixture (Holt, 2018; Shyamsunder et al., 2020a).

(a)

(b)
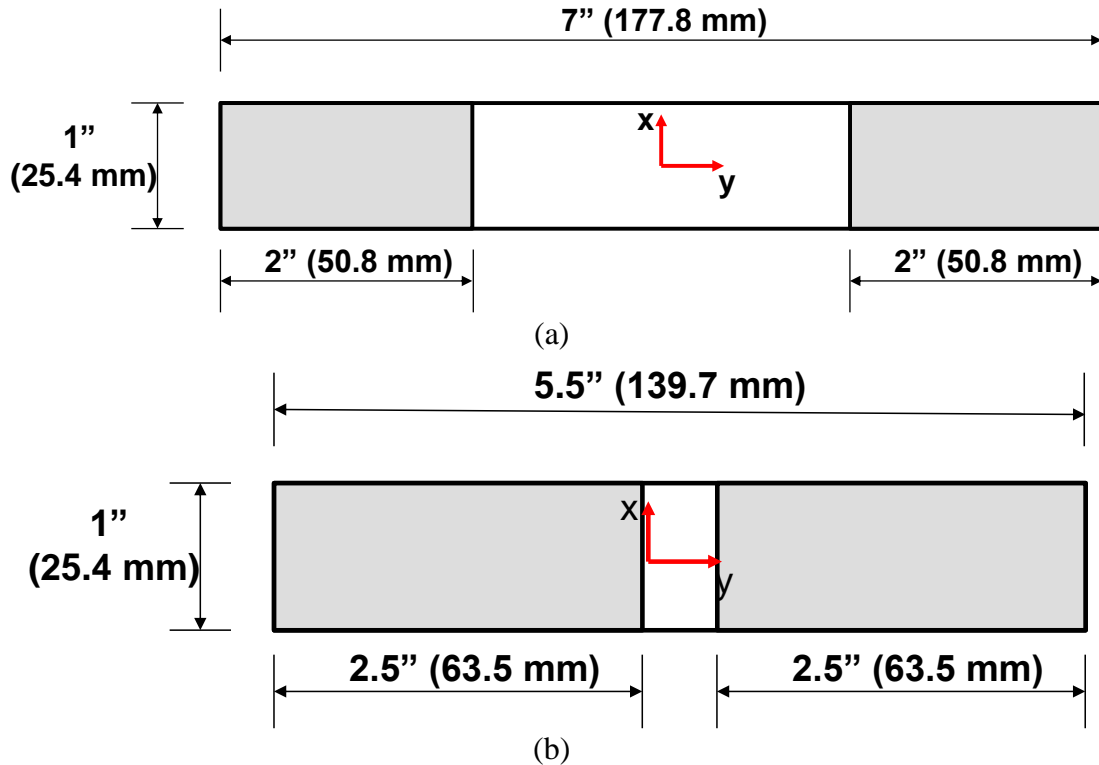
Figure 21. Schematic Diagram (a) Tension Test (b) Compression Test (Shyamsunder et al., 2020a)

Finite Element Modeling: The tabbed regions in the specimen are excluded from the finite element model so as to create a computationally efficient model. Figure 22 shows the FE models with the fine mesh used for the stacked-ply tension test (SPVT) and stacked-ply compression test (SPVC). 8-node hexahedral elements are used. There are eight elements through the thickness corresponding to the eight plies in the experimental

specimen. Table 5 shows FE model details for the fine, medium and the coarse meshes. The SPVT boundary conditions are shown in Figure 23 using the highlighted nodes in the fine mesh model. All the nodes on the support face are restrained from displacement in the y-direction as shown in Figure 23(a). The center line nodes through the z-direction are restrained from displacement in the x-direction as shown in Figure 23(b). This is done to avoid strain localization on the support face. Since only the gage section is modeled, the displacement at the end of the gage section from the experiment is taken from the digital image correlation (DIC) analysis (Holt, 2018) and applied to the FE model along the positive y-direction on the loading face nodes as shown in Figure 23(c). The nodes on the loading face are also restrained in the x-direction. To avoid rigid body motion in the z-direction (out-of-plane), the center line nodes through the x-direction on either end are restrained in the z-direction direction as shown in Figure 23(d). The boundary conditions are similar for both SPVT and SPVC models except for the applied loading. Also, in the case of SPVC, all the nodes at the support face are restrained in displacements in both the x and the y-directions. LS-DYNA's (Ansys-LST, 2020b) reduced integration option has been used with appropriate hourglass control.
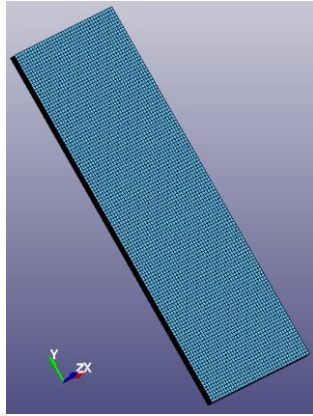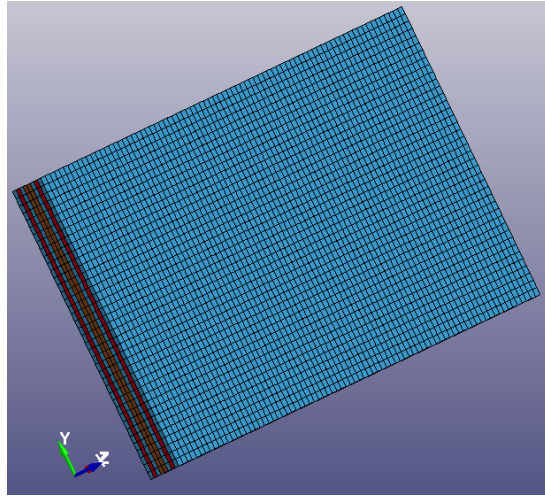
<div align="center">
(a)   (b)

Figure 22. FE Model Used for (a) Stacked-Ply Tension Test (SPVT) (b) Stacked-Ply

Compression Test (SPVC).
</div>

(a)

(b)

(c)

(d)
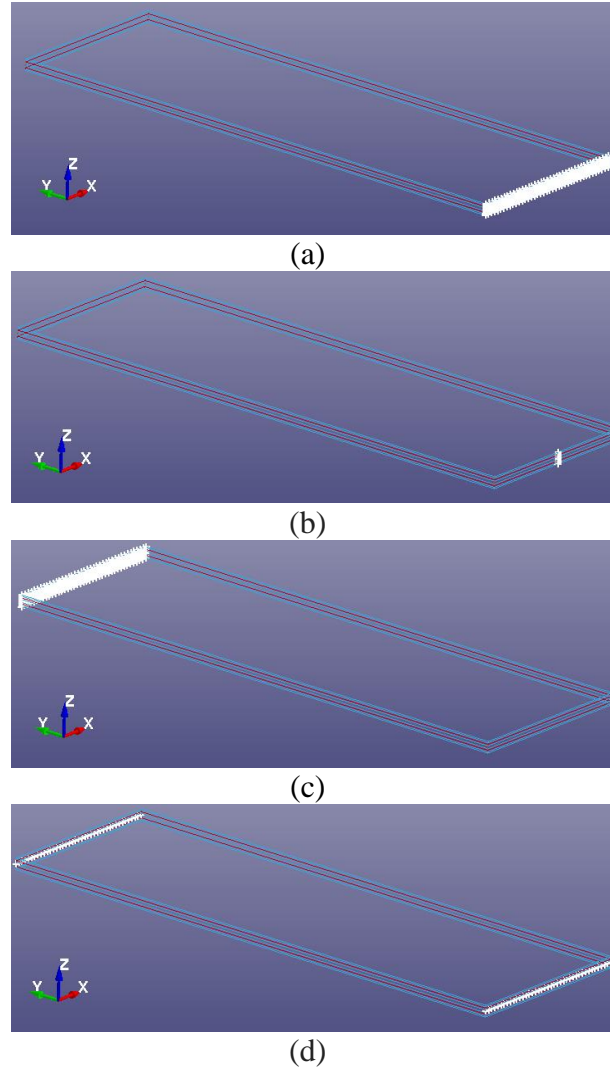
Figure 23. SPVT Boundary Conditions (a) y-Displacement Restraint (b) x-Displacement

Restraint (c) x-Displacement Restraint and Applied Displacement along y-Direction (d)

z-Displacement Restraint.

Table 5. Number of Elements in the FE Models

Test	Number of Elements (Largest Aspect Ratio)		
	Fine	**Medium**	**Coarse**
SPVT	38400 (3.2)	9600 (6.4)	2400 (12.8)
SPVC	25600 (1.6)	6400 (3.2)	1600 (6.4)

Results: The load versus time graph is used to compare FE and experimental results. For the FE model, the nodal reactions at the support face along the loading direction are added to obtain the load value. The experimental values have been obtained from the test frame load cell. The SPVT load vs time graphs with PFC and GTFC are shown in Figure 24(a) and (b), respectively. The energy vs time graph with the fine mesh is shown in Figure 25.

(a)   (b)

Figure 24. Stacked-Ply Tension Test Load vs Time Plot with (a) PFC and (b) GTFC.

(a)   (b)
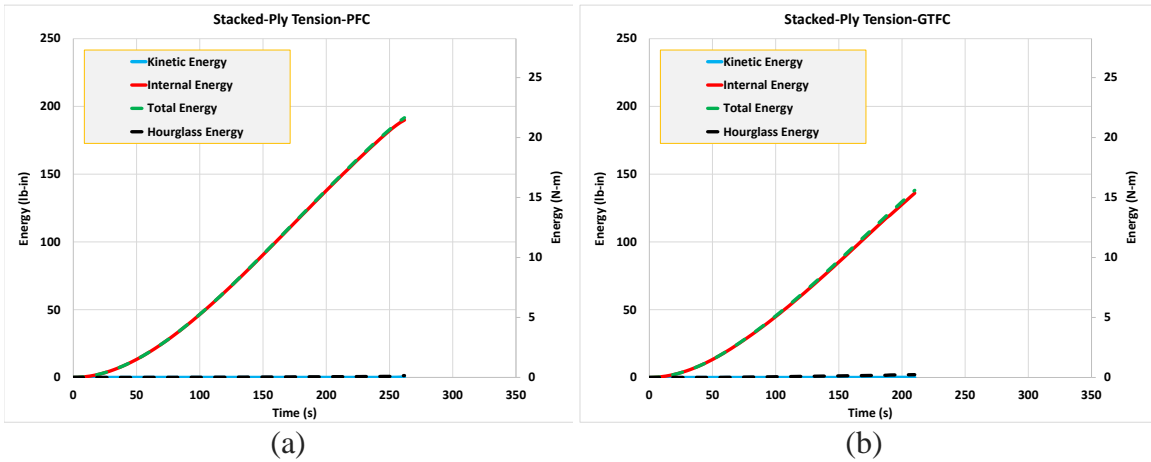
Figure 25. Stacked-Ply Tension Test Energy vs Time Plot (Fine Mesh Model) with (a)

PFC and (b) GTFC

The PFC SPVC fine mesh results are shown in Figure 26(a) before failure-related parameters are calibrated as well as after calibration (tagged as *Modified Strength*). The GTFC results are shown in Figure 26(b). No failure-related parameter calibration has been performed. The corresponding energy plots are shown in Figure 27(a) and (b), respectively.

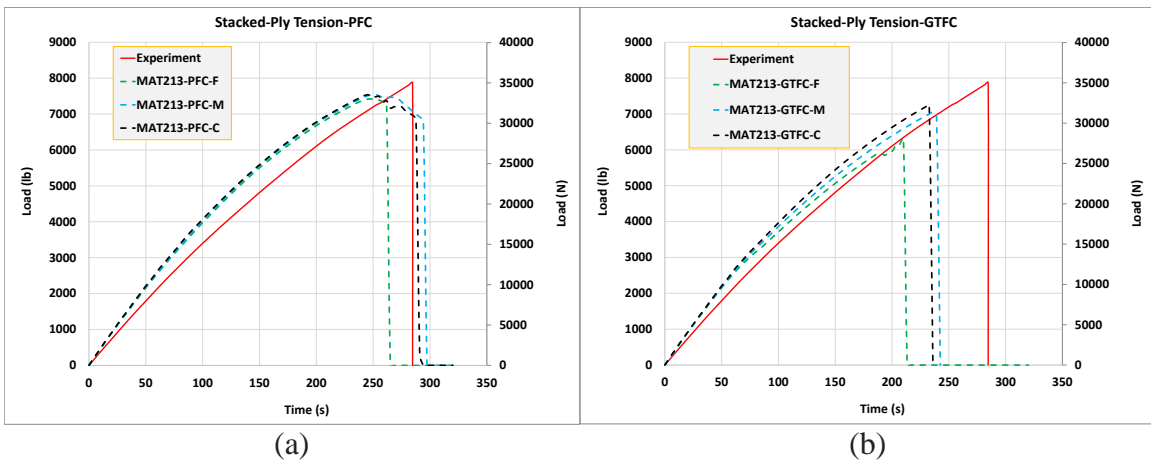(a)   (b)

Figure 26. Stacked-Ply Compression Test Load vs Time Plot with (a) PFC and (b) GTFC

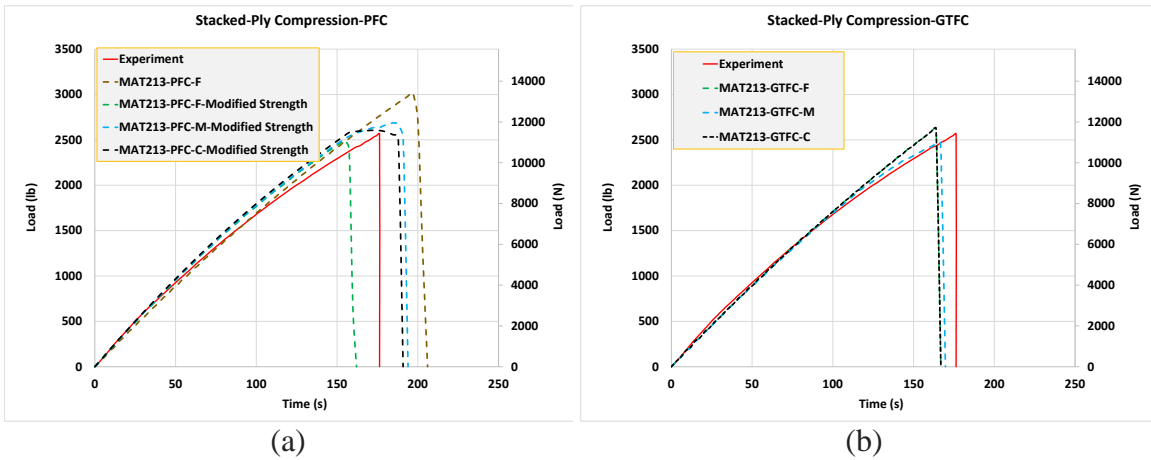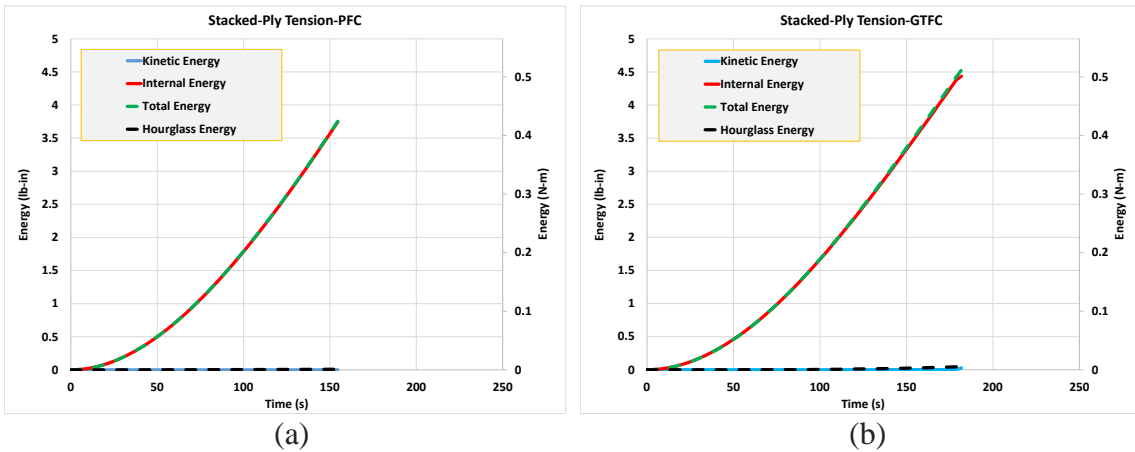(a)   (b)

Figure 27. Stacked-Ply Compression Test Energy vs Time (Fine Mesh Model) with (a)

PFC and (b) GTFC

Discussion SPVT Models: The peak load predicted using PFC agrees well with the experimental results. The overall FE response is a little stiffer. The distribution of the longitudinal stress (y-stress) is uniform in the model. IFF first initiates in the $\pm 45^\circ$ plies, then in the 90° plies, after which FF initiates in the 0° plies. This is immediately followed by a uniform erosion of the elements throughout the entire model. The differences when there is complete loss of load carrying capacity (zero load value) amongst the three mesh sizes is probably due to the different aspect ratios used in these models. The aspect ratios of the element play an important role in element erosion (Eq. 3.4). Overall, the prediction is an improvement compared to results using the earlier implementation of PFC (Shyamsunder et al., 2020a). In the simulations using GTFC, the equivalent failure strain is assumed to be 0.8. The peak load predictions are lower than the experimental values - the coarse and the medium model are about 15% less and the fine model is about 20% less. It should be noted that after the true stress reaches the peak in each component of input stress-strain curves, the true stress starts to degrade. This is in contrast to PFC where the true stress degrades only after the failure criterion is satisfied. The difference in the prediction amongst the different mesh sizes (about 5%) can be attributed to the fact that GTFC is not mesh independent.

Discussion SPVC Models: In the model using the fine mesh with PFC, the peak load prediction is about 20% higher than the experimental result. Subsequently, a few failure-related parameters have been calibrated. The 1-direction compressive strength, $R_\parallel^c$ has been reduced slightly by about 2% to 102899 psi (709 MPa), a value that is within the

experimental coefficient of variation of 9.7% (Khaled et al., 2017). In addition, Γ_f has

been reduced to 20 lb/in (3502 N/m). The value of $PPRD_{C\parallel}$ has been increased to 0.75

since the previously assumed value (0.255) made the FE model too stiff. After

calibration, the predictions agreed with the experimentally obtained value. IFF first

initiates in the $\pm45^{\theta}$ plies and 90° plies, followed by FF in the 0° plies. Like the SPVT

case, difference in the point of time at which the model completely loses its of load

carrying capacity compared to the experimental values can be observed. This can be

attributed to the difference in the aspect ratios of the elements in the three models.

Similarly, the GTFC failure-related parameters have been calibrated. The tension and

shear residual strength components are taken as 10% of the respective peak stress, and

the   equivalent   failure   strains   are   reduced   from   0.8   to

$\varepsilon^{eq}_{IP^{FAIL}} = \varepsilon^{eq}_{OOP^{FAIL}} = 0.016(F), 0.011(M), 0.008(C)$ making the peak load prediction more

accurate but mesh dependent.

In all the stacked-ply simulations, the load is predominantly carried by the 0^0 plies. As

can be seen from the energy plots, as required, the kinetic energy and the hourglass

energy are negligibly small for both PFC and GTFC. It is believed that some

improvements can be made to the models. First, only the gage section of the specimens is

modeled. Modeling the whole specimen with the fiberglass tabs will lead to a much

larger model but may improve the predictions made for the compression test since

boundary effects such as stress concentrations can be avoided. This will also require the

modeling of the interface between the tabs and the composite. In the $\pm45^0$ plies in the FE

model, the edges of the elements are aligned along the loading direction rather than the along the fibers. Modeling the edges of the elements in $\pm45^0$ plies along the fiber direction with the use of tie-break may improve the results as failure of elements is in this case, dependent on element orientation.

4.2.4 Ballistic Impact Validation Test

Background: A set of ballistic impact tests has been conducted at NASA-Glenn Research Center (Melis et al., 2018). These tests are designed to produce validation test data for the developed OEPDMM constitutive model. The experimental set-up which involves a single state gas gun is shown in Figure 28(a) (Hoffarth et al., 2017). In each of the tests, the target is a composite panel impacted with a 50 gm (0.122 lbm) aluminum (Al-2024) projectile at different velocities ranging from 119 ft/s (36.3 m/s) to 530 ft/s (161.5 m/s). These tests are listed in Table 6. The composite (flat) panel is made of 16 plies of T800/F3900 composite with a lay-up of $[(0/90/45/-45)_2]_s$. The dimensions of each panel are 12 in. x 12 in. x 0.122 in. (30.48 cm x 30.48 cm x 0.3099 cm). The composite panels are clamped by a circular frame with an inner diameter of 10 in. (25.4 cm) as shown in Figure 28(b) and Figure 28(c). The photograph of one of the aluminum projectiles used for the tests is shown in Figure 28(d). Digital image correlation (DIC) data gathered from high-speed cameras have been used with the ARAMIS software system (Melis et al., 2018) to obtain both projectile information as well as the displacement of the front and back sides of the impacted panel.
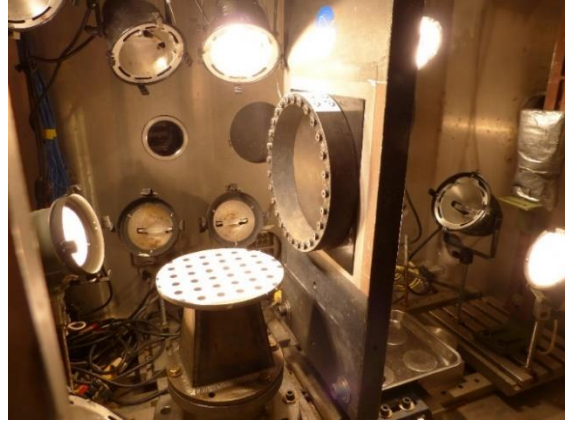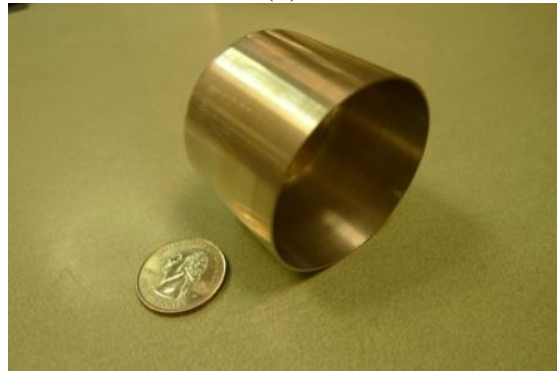
Figure 28. Ballistic Impact Test Set-up: (a) Single State Gas Gun (b) Inside View of Test Chamber Showing the Front of the Composite Panel (c) Inside View of the Test Chamber Showing the Back of the Composite Panel (d) Projectile

Table 6. Ballistic Impact Tests

Test	Projectile Velocity		KE	Contained
	(ft/s)	(m/s)	(J)	
LVG1065	119	36.3	32.8	Yes
LVG1067	154	46.9	54.4	Yes
LVG1071	155	47.2	55.4	Yes
LVG1072	172	52.4	68.1	Yes
LVG1073	172	52.4	68.4	Yes
LVG1069	177	53.9	72.2	Yes
LVG1068	181	55.2	75.6	Yes
LVG1070	181	55.2	75.7	Yes
LVG1066	189	57.6	82.2	Yes
LVG1064	236	71.9	128.1	Yes
LVG1075	385	117.3	341.8	Yes
LVG1074	417	127.1	403.5	No
LVG1076	454	138.4	474.4	No
LVG1063	530	161.5	650.3	No

In this sub-section, the LVG1075 test with the projectile velocity as 385 ft/s (117.3 m/s) is chosen for validating the improved failure sub-models. This test case has been chosen since this test case has the highest projectile impact velocity with the projectile contained and significant damage. The crack pattern is clear and is used as a qualitative metric for comparison with the simulation. Figure 29(a) shows that the panel is clamped and bolted, and Figure 29(b) shows a close-up view showing the rear side of the panel with visible damage. The projectile rebounded after the impact with an average velocity of 46.4 ft/s (14.15 m/s).

(a)   (b)
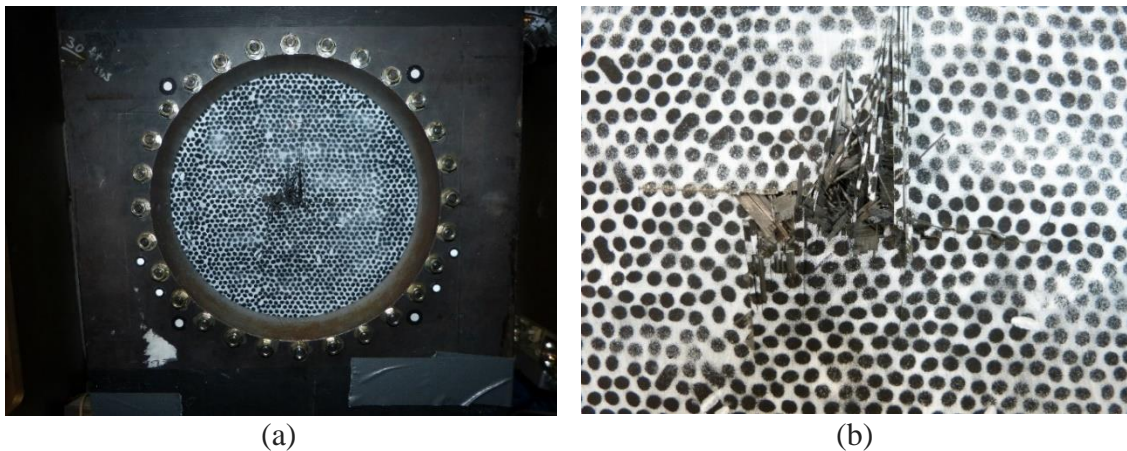
Figure 29. (a) Back View of the Composite Panel after the Test Clamped (b) Zoomed in Picture of the Cracks Formed on the Back Side of the Panel (Shyamsunder et al., 2020a). Closer Examination Shows a Through Crack

Finite Element Modeling: A detailed mesh study has been carried out to find an optimal mesh with a view to satisfactorily balance accuracy and computations (Achstetter et al., 2020). For a number of impact models, the element aspect ratio, number of elements in the through thickness direction, hourglass control, and the element integration order have

been varied to gage the effect of each parameter on the maximum out-of-plane displacement and the time at which the maximum displacement occurred. These two computed values have been compared against the experimental results. Based on the study, the FE model shown in Figure 32 is used for this work. Table 7 shows the details of the FE model. 8-node hexahedral elements are used in the FE models. The panel is modeled using 16 elements through the thickness with a one-element layer for each ply. In between the plies, cohesive zone elements are used. There are 15 CZE layers modeled using LS-DYNA's MAT186. The aluminum projectile is modeled using LS-DYNA's MAT024. The nodes at the location of the bolts are restrained in-plane, and the nodes at the clamps are restrained in the out-of-plane direction. Figure 33 shows the boundary conditions used for the simulation.

Table 7. FE Model Details

Number of Elements			Number of Nodes
MAT213 (plies)	MAT186 (between plies)	MAT024 (projectile)	
373184	349860	17040	775238

Numerical calibration is carried out with the PFC model. The post-peak residual damage parameters used are: $PPRD_{T\|} = 0.64,\ PPRD_{C\|} = 0.0,\ PPRD_{T\perp} = 0.64,\ PPRD_{C\perp} = 0.0,$ and $PPRD_S = 0.64$. The fracture energies have also been calibrated, and the values used are:

$$\Gamma_I = 400.0\,lb/in\left(7 \times 10^4\ N/m\right) \quad \text{and} \quad \Gamma_{II} = 400.0\,lb/in\left(7 \times 10^4\ N/m\right).$$ Numerical

calibration has also been carried out with the GTFC model. It is assumed that the in-plane

residual strengths in the 1-direction tension, 2-direction tension and 1-2 shear components are 30%. The through thickness residual strengths (3-direction tension, 2-3 shear and the 1-3 shear components) are assumed to be 34%. The equivalent failure strain has been assumed to be 0.8.

Results: Figure 32(a) shows the last frame from the LVG1075 simulation run with PFC and Figure 32(b) with GTFC. The simulations are terminated when the projectile rebound velocity becomes constant. Node identified as N402688 in Figure 32(b) is used to track and compare the out-of-plane displacement (Figure 33(a)). Figure 33(b) shows the projectile velocity as a function of time. It should be noted that (a) negative velocity indicates projectile rebound, and (b) the average rebound velocity of the projectile obtained from the experiment is shown as an average value.
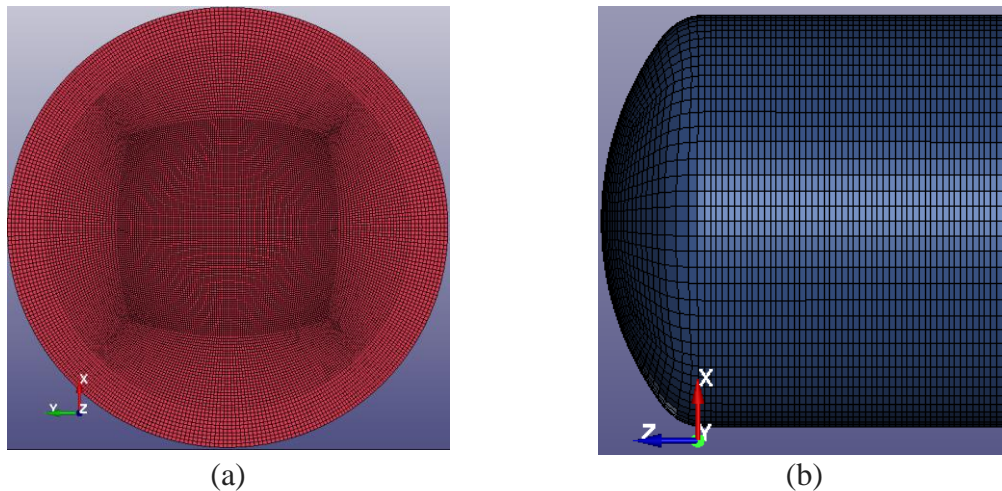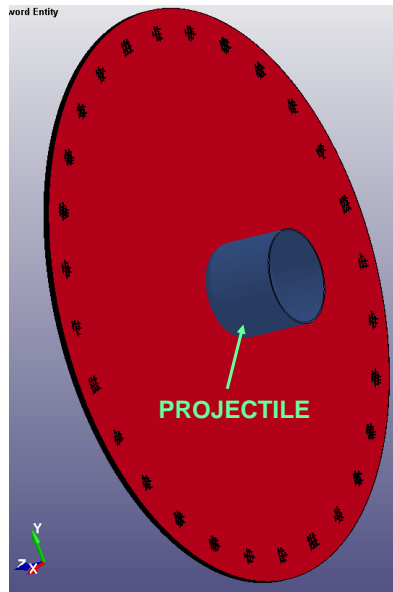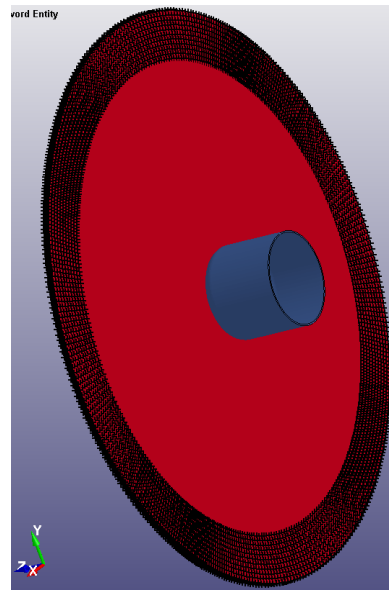

| (a) | (b) |
Figure 30. FE Model Mesh Used for: (a) Panel (b) Projectile
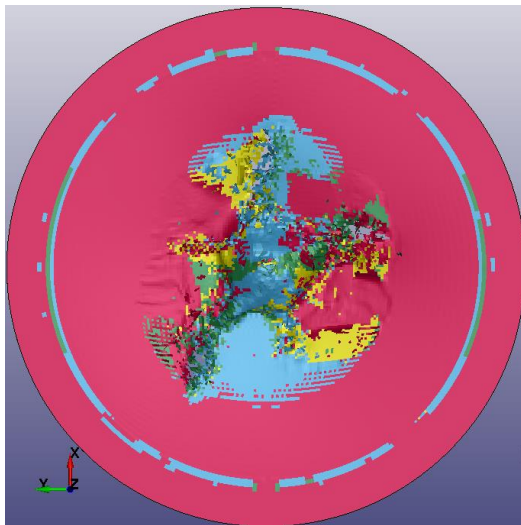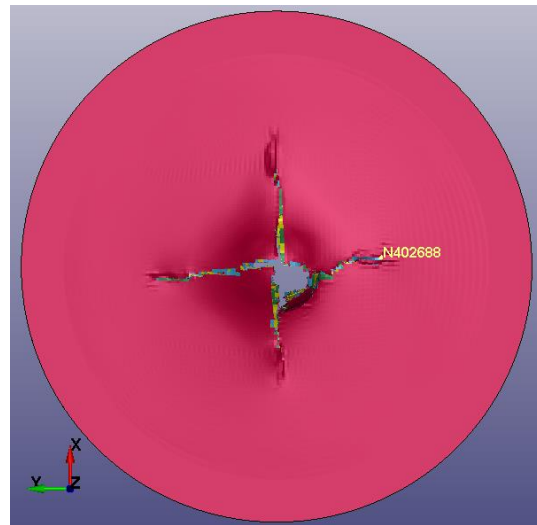
(a)   (b)

Figure 31. Nodes which have Translational Restraints: (a) In-Plane Displacement (b)

Out-Of-Plane Displacement

(a)   (b)

Figure 32. LVG1075 Simulation Showing Impacted Panel at the Final Time Step with the

Projectile Hidden from View (a) Using PFC (b) Using GTFC
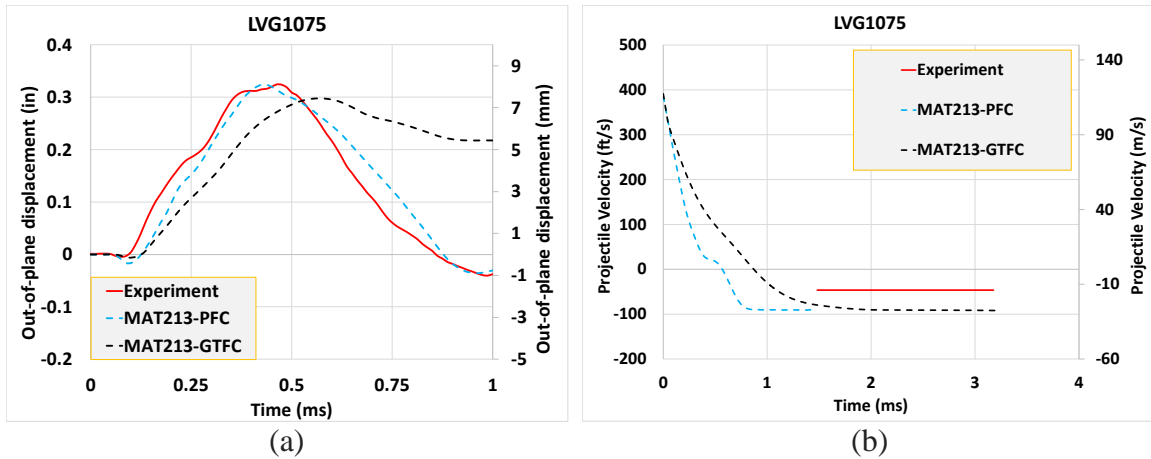
Figure 33. (a) Out-Of-Plane Displacement at Node 402688 (b) Projectile Velocity Plotted

Against Time. Experimental Rebound Velocity Estimated and Averaged Over a Period of

1.5 ms

Discussions: As can be seen from Figure 32(a), there is widespread surface damage

including elements eroded around the clamped region in the FE model contrary to the

experimental results (Figure 29). The element erosion is due to the combination of both

FF and IFF. The out-of-plane displacement is captured very well for the first 1 ms that

includes both the first positive and the first negative peaks. It should be recognized that

node 402688 in the region with considerable surface damage starting around 1 ms and

hence both the FE computed response and the experimental values are reliable only for

that time duration. The calibration of the six failure-related parameters yields a flakier

panel with a different damage and crack patterns and a higher rebound velocity. Perhaps,

regression analysis involving these parameters may yield improved results, but the

primary objective of the validation test is to show the difficulties in modeling impact tests

without resorting to an involved parameter calibration process.

97

The GTFC results show that the qualitatively crack pattern obtained from the FE simulation reasonably matches the experiment. In addition, the crack is a through crack similar to the experiment. The maximum out-of-plane displacement prediction agrees well with the experimentally obtained value though there is difference in the wavelength of the displacement profile. The rebound velocity it overestimated similar to the PFC results. It should be noted that the calibration of the input residual strength has been done with multiple objectives – matching crack pattern, out-of-plane displacement and rebound velocity, and it is very likely that decreasing the residual strengths in the tensile and the shear components can lead to a less stiff panel response.

4.3   GTFC Rate-Dependent Validation

4.3.1   Processing Rate Data

Careful processing of rate-dependent stress-strain data before these are used in finite element analysis is necessary to ensure that the data for various rates are used consistently in the constitutive model. Using the Kuhn-Tucker form of the loading/unloading conditions (Berstad et al., 1994) as applicable to the consistency method, it can be shown that as soon as visco-plastic yield criterion is satisfied (the viscous stress that is dependent only on plastic strain rates), there is plasticity. The strain rates that generate the viscous stress, create purely plastic strains above the *static* yield surface. In other words, a correct, tacit assumption is that the dynamic yield surface will never be below the yield surface at the same temperature.

Processing of the input stress-strain curves is illustrated here using Figure 34 as an example. Figure 34(a) shows the curves for the 2-direction tension component at three different strain rates (Deshpande et al., 2019; Khaled et al., 2017). The corresponding stress-effective plastic strain curves are shown in Figure 34(b). Care must be taken to avoid intersecting stress-effective plastic strain curves as intersecting curves will likely result in either inaccurate results or numerical instability. Often, intersecting curves result from selecting incorrect initial yield strain value.
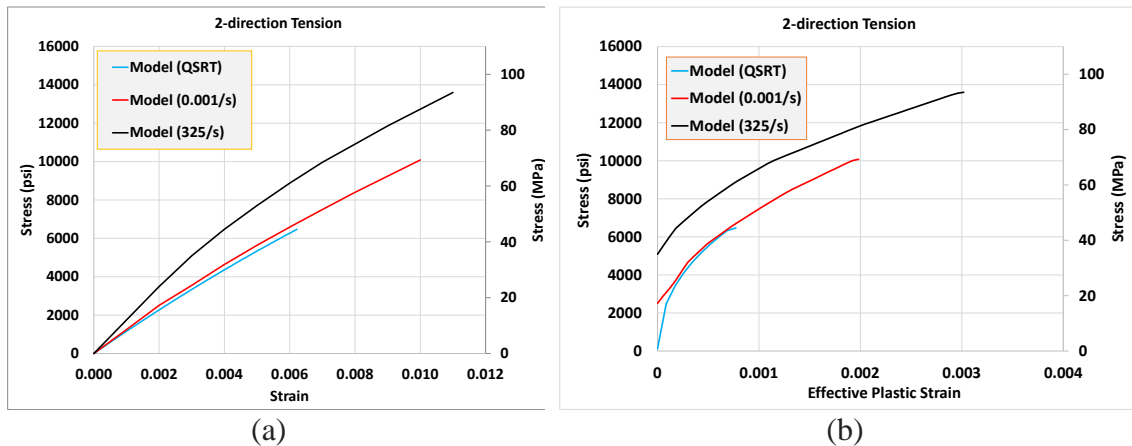
Figure 34. 2-Direction Tension Data for the T800-F3900 Composite: (a) Experimental Stress-Strain Curves (b) Effective Stress vs Effective Plastic Strain Curves Constructed from Data in (a)

Figure 35(a) shows the post-failure augmented stress-strain curves for 2-direction tension. The figure also shows the 2-direction tension effective damage parameter curve (see secondary axis). In the current implementation, for each of the twelve stress-strain components only a single effective damage parameter curve can be used. This implies that for a given component, the effective damage parameter curve must be compatible

99

with all the stress-strain curves. If there is no compatibility, there would be a numerical issue - plastic strain computed in the pre-processing step will turn out to be negative. The compatibility is maintained by making sure that all the stress-strain curves (3 in this case) have the same ultimate strain values. As can be seen in Figure 34(a), *Exp (325/s)* has the highest ultimate strain. So, the *Model (QS-RT)* and *Exp (0.001/s)* are modified to have an additional data point with a stress value equal to the respective peak stress and a strain value equal to the ultimate strain of the *Exp (325/s)* curve. The stress is gradually brought down to a residual strength of 30% of the respective peak stresses for all the 3 curves. The residual strength of 30% is a calibrated value obtained from the impact validation tests. Further explanation on the same is presented in the numerical results section. Since the plasticity algorithm requires a non-negative slope in the effective stress-effective plastic strain curve, the effective stress is kept constant as shown in Figure 35(b).

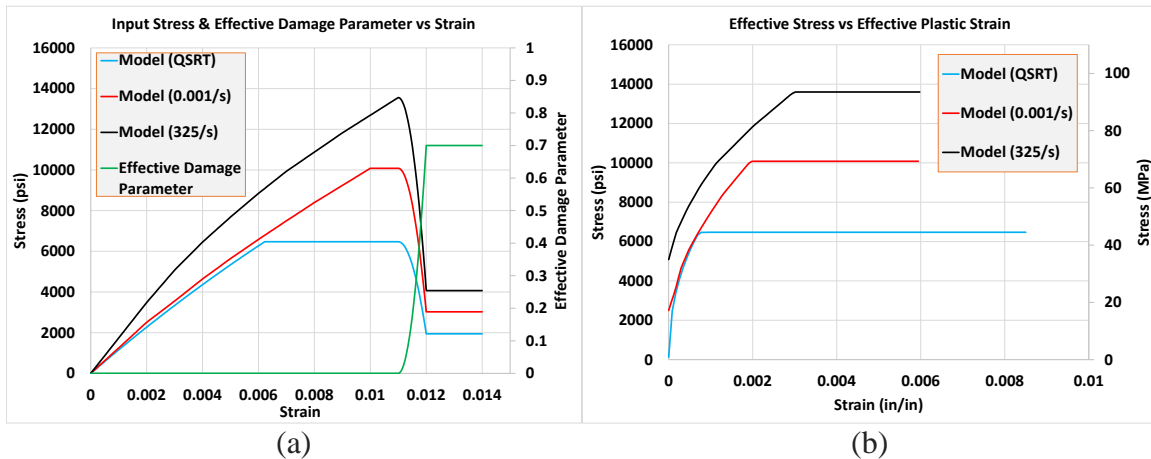(a)   (b)

Figure 35. 2-Direction Tension Data for T800/F3900 Composite: (a) Input Stress and Effective Damage Parameter vs Strain Curves (b) Effective Stress vs Effective Plastic Strain Curves Constructed from Data in (a)

4.3.2   Ballistic Impact Validation Test

The four highest speed tests discussed in the earlier section with additional stress-strain input at higher strain-rates are used to evaluate GTFC. The test cases are LVG1075, LVG1074, LVG1076 and LVG1063. These cases have been chosen since these have the highest impact energy and three out of the four are uncontained tests. The primary metric for comparison is the final projectile velocity (exit/rebound velocity).

Material Data: There are two material models - OEPDMM for the composite panel and MAT024 for the aluminum projectile. In addition to the QS-RT curves, the following stress-strain curves at room temperature are used: (a) 2-direction tension at 10^{-3}/s and 325/s, (b) 2-direction compression at 10^{-3}/s, 1/s and 813/s, and (c) 3-direction compression at 800/s (Deshpande et al., 2019). In addition: FILT=0.0 in Eq. 2.11 since no numerical instabilities are detected, all the components of decay constants in the $\boldsymbol{\beta}$ vector in Eq. 2.13 and 2.14 are taken as 0.001.

GTFC Data: All the compression residual strength parameters are equal to the respective peaks in the stress-strain input curves, $c_i^{RS} = 1.0, i = 4,5,6$. The residual strength used for the tension and the shear components for the in-plane components is assumed to be 30% whereas, it is assumed that this value is 12% for the out-of-plane components ($c_1^{RS} = 0.3$, $c_2^{RS} = 0.3$, $c_3^{RS} = 0.12$, $c_7^{RS} = 0.3$, $c_8^{RS} = 0.12$, $c_9^{RS} = 0.12$). In   the   absence   of experimental data, it is assumed that the two equivalent failure strains are equal ($\varepsilon_{IP^{FAIL}}^{eq} = \varepsilon_{OOP^{FAIL}}^{eq} = 0.80$) and are a constant function of the failure angle. The interaction

101

term, n is taken as 2 thereby coupling the in-plane and the out-of-plane states of stress that is expected in an impact event. These failure parameters are obtained after calibration, the objective of which is to reduce the error involved in the prediction of the projectile exit/rebound velocity.

FE Model: A number of impact models, the element aspect ratio, number of elements in the through thickness direction, hourglass control, and the element integration order are varied to gage the effect of each parameter on the maximum out-of-plane displacement and the time at which the maximum displacement occurred (Achstetter et al., 2019). These two computed values are compared against the experimental results. Based on the study, the following FE model parameters are selected for use in this section: (a) 8-node reduced integration hexahedral elements is used to model the panel and the projectile, (b) each ply in the panel is modeled using one element through the thickness, and (c) while the results are not sensitive to different hourglass control, viscous hourglass control (IHQ=1) led to low hourglass energy values and hence are used. The optimal mesh has a total of 99144 nodes, 91728 elements to model the panel, and 17040 elements to model the projectile. It should be noted that a coarser version of the mesh is used compared to the one used in Section 4.2.4 in order to reduce the simulation run time. Numerical experiments indicated that CZE layers do not affect the results and hence, are not used in the FE model.

The nodes at the location of the bolts are restrained in-plane (Figure 36(a)), and the nodes at the clamps are restrained in the out-of-plane direction (Figure 36(b)). Eroding single

surface (*CONTACT_ERODING_SINGLE_SURFACE) and eroding surface-to-surface (*CONTACT_ERODING_SURFACE_TO_SURFACE) control controls are used. The numerical examples use the deformation, damage and the failure sub-models in OEPDMM.

(a)   (b)
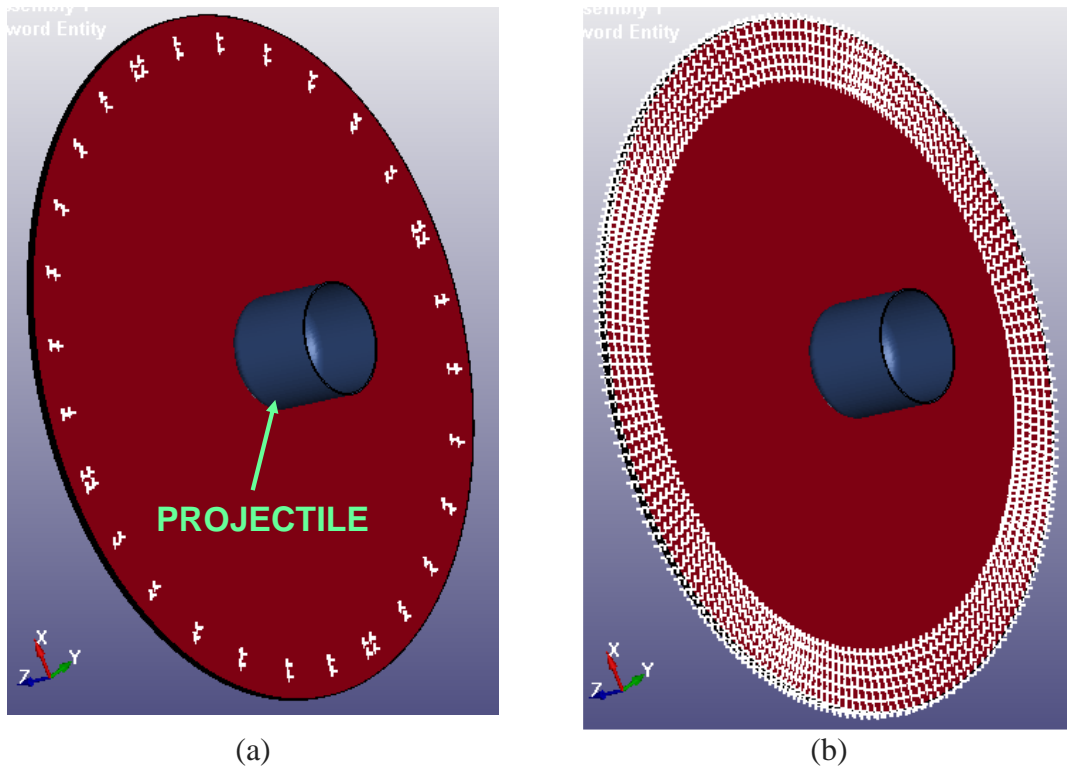
Figure 36. Nodes which have Translational Restraints: (a) In-Plane Displacement (b)

Out-Of-Plane Displacement

Results: The projectile exit/rebound velocity is used as the metric for the comparison of the experimental and the simulation results (Figure 37). The qualitative comparison of the crack patterns is shown in Figure 38. It must be noted that the crack patterns shown are captured at the last frame from each simulation corresponding to the last point in Figure

37. Table 8 shows the exit/rebound velocity error with respect to the experimental value. It also shows the normalized energy absorbed based on the kinetic energy and the respective error with respect to the experiment. Figure 39 shows e_1 and e_2 contours on the back side of the panel from the simulations. These images are captured at the same point of time for each of the test cases when e_1 and e_2 values are significantly large before a large through cracks are formed.

Figure 37. Comparison of Projectile Velocity for the Impact Tests

Discussions: A sensitivity analysis was carried out where the failure parameters- in-plane residual strength ($c_1^{RS} = c_2^{RS} = c_7^{RS}$), out-of-plane residual strength ($c_3^{RS} = c_8^{RS} = c_9^{RS}$) and

equivalent failure strain ($\varepsilon_{IP^{FAIL}}^{eq} = \varepsilon_{OOP^{FAIL}}^{eq}$) are taken as three parameters to be varied, and the exit/rebound project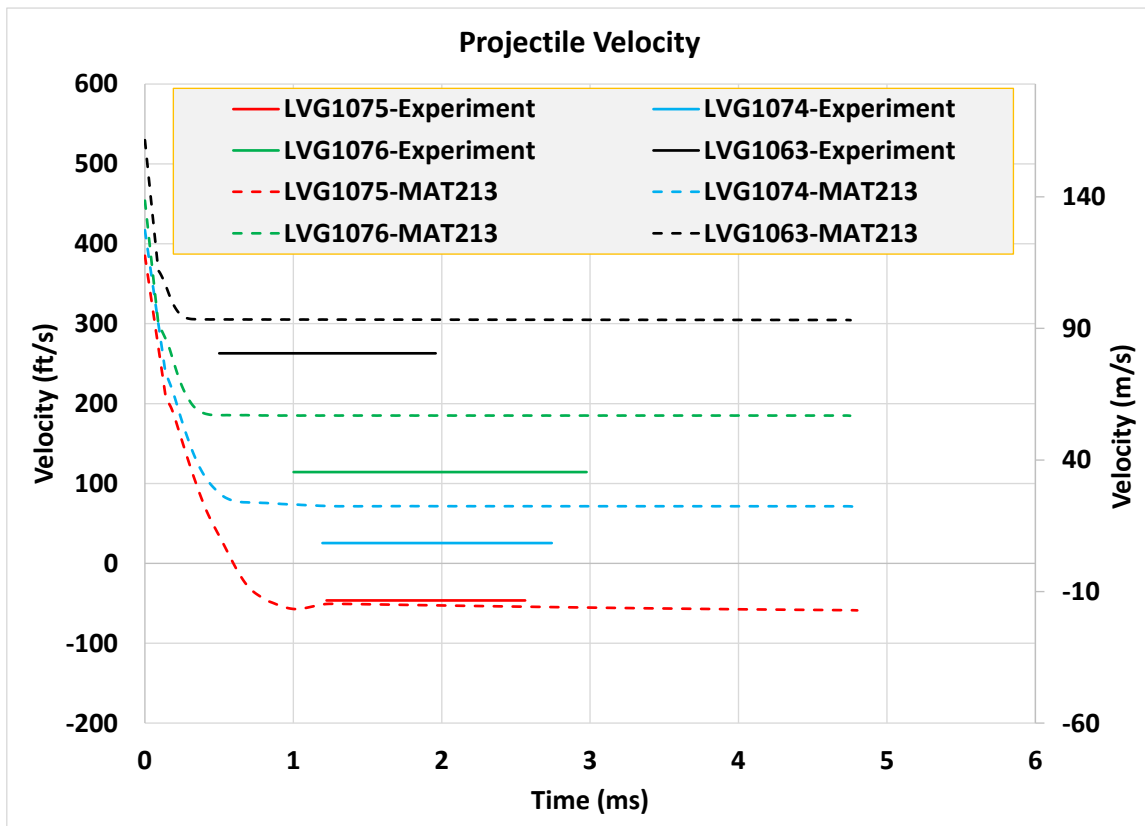ile velocities are monitored (results not shown here). It was observed that the out-of-plane residual strength is the most significant parameters which affects the projectile exit/rebound velocity. This is also evident from Figure 39 where it can be seen that e_2 values are higher than the corresponding e_1. This is because a projectile that is impacting perpendicular to the plate is likely to cause the through-thickness failure as the dominant mode of failure. In other words, increasing the out-of-plane residual strength makes the panel stiffer thereby decreasing the exit velocities or increasing the rebound velocities. The contained test (lowest projectile impact velocity) is chosen where an excess increase in the residual strength would cause the projectile to rebound with a much higher velocity. The predicted rebound velocity is very close to the experimentally obtained average rebound velocity with the use of appropriate failure parameters (parameters mentioned earlier). The projectile rebound velocity profile has a slight decrease in the slope with respect to time because there is a lot of rotation which is adding up to the out-of-plane velocity component. For the other test cases, the predictions made are on the conservative side – the projectile exit velocities are more than the respective experimentally obtained average exit velocities. This is desirable from a design point of view. The objective is to see whether the predictions have the same trend.

Table 8. Impact Validation Test Error Computation

Test	Impact Velocity (V_{IMP}) in ft/s (m/s)	Exit/Rebound Velocity (V) in ft/s (m/s)			Normalized Energy Absorbed $=\dfrac{V_{IMP}^2 - V^2}{V_{IMP}^2}$		
		Experiment	Simulation	Error	Experiment	Simulation	Error
LVG1063	530 (161.5)	262.9 (80.1)	306.0 (91.4)	16.6%	0.75	0.67	-8%
LVG1076	454 (138.4)	114.2 (34.8)	187.5 (45.7)	64.1%	0.94	0.83	-11%
LVG1074	417 (127.0)	25.4 (7.7)	71.8 (11.5)	182.4%	0.99	0.97	-2%
LVG1075	385 (117.0)	-46.4 (-14.14)	-58.8 (-17.9)	26.0%	0.99	0.98	-1%

As can be seen in Table 8, the error involved in the energy absorbed is close to or below 10% for all the test cases. On the other hand, the simulations do not yield crack patterns that match the experiments. There are a few major factors affecting this behavior. First, the mesh size affects the crack pattern since in the failure sub-model, there is no mesh regularization technique. Second, as discussed earlier, there is no rate data available for the 3-direction tension component or the shear components. Figure 40 shows the 1-3 shear strain-rate for all the different plies when the projectile makes contact with the panel for LVG1075 test. As can be seen, the 1-3 shear strain-rate magnitude is very high (in the order of 10^4) in some of the elements in the 0° ply. Figure 41 shows the plastic

multiplier contour at the same point of time as that of the contours shown in Figure 40. The plastic multiplier magnitudes in some of the elements (mostly at the center) are also in the order of 10^4 which is much higher than the input (of the order of 10^2). Having more rate dependent input stress-strain curve would probably help better predict the response of the impact test. Fourth, the boundary conditions used for these test cases seems to have over constrained the panel since the crack is not distributed over the surface area of the panel. Further investigation is under way to see the effect of the boundary conditions applied to the composite panel.
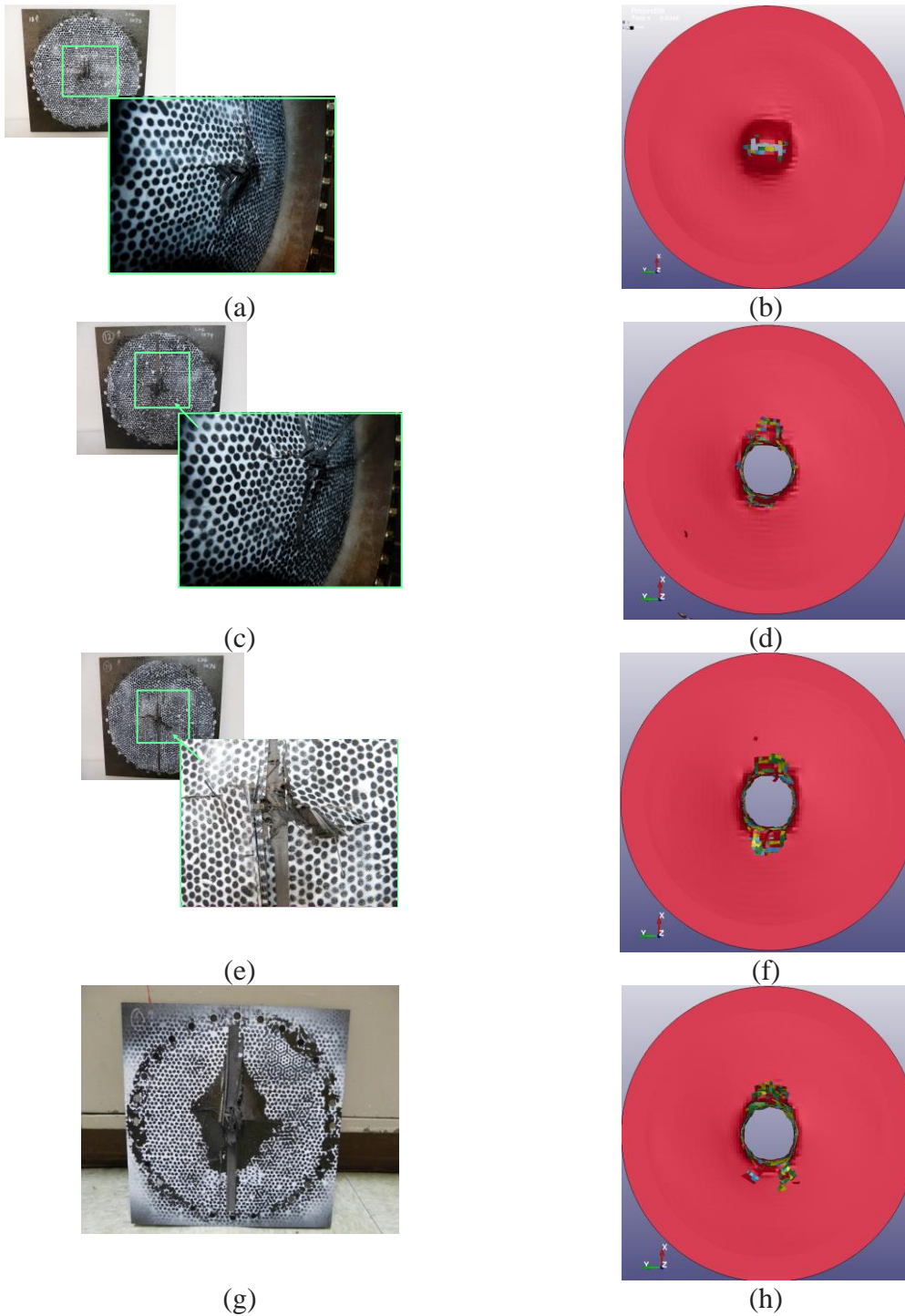
Figure 38. Back View of the Test Composite Panel After the Experiment for (a)

LVG1075 (c) LVG1074 (e) LVG1076 (g) LVG1063. Back View of the Last Frame of the

Panel from the Simulation for (b) LVG1075 (d) LVG1074 (f) LVG1076 (h) LVG1063
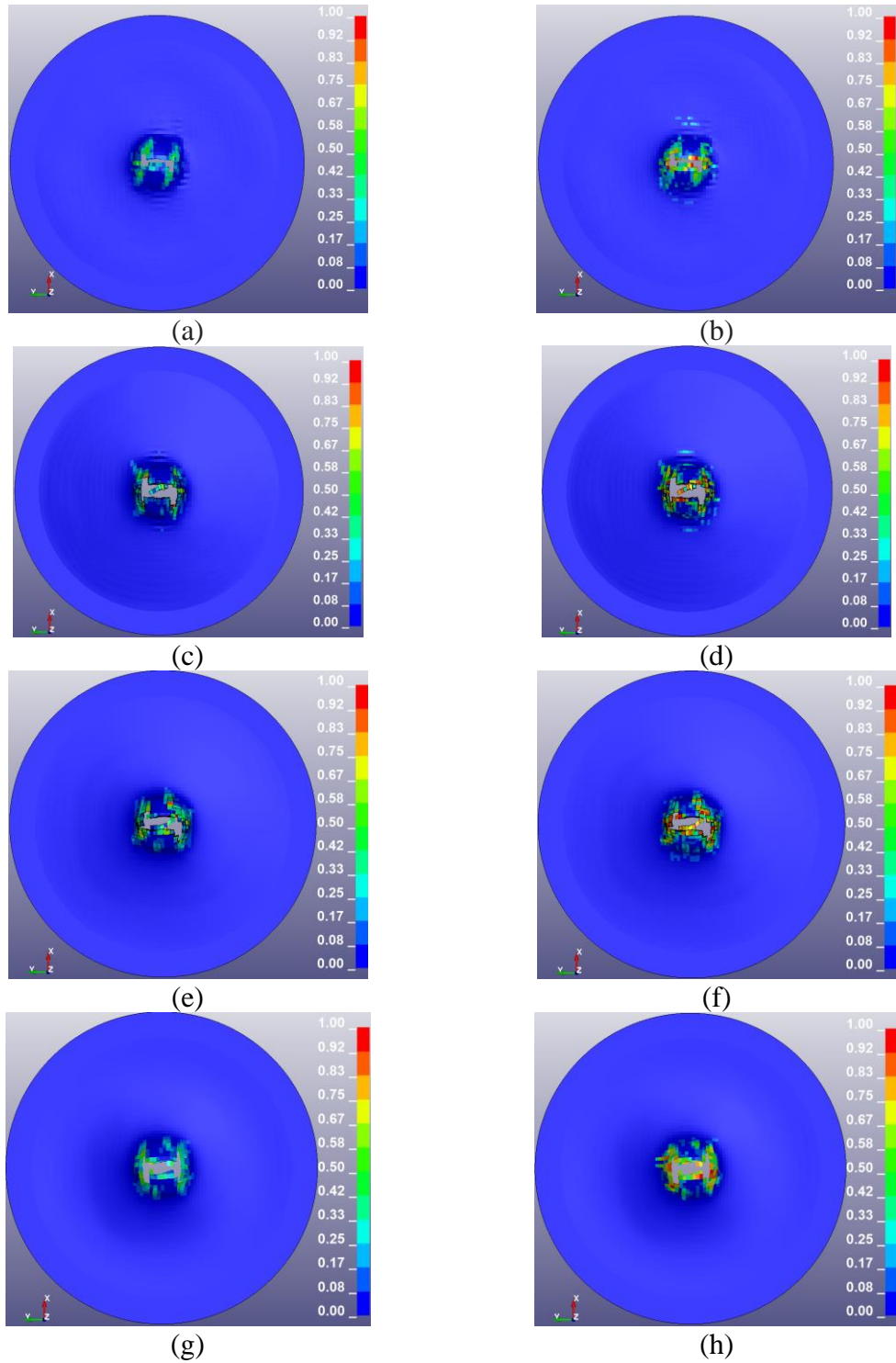
Figure 39. e_1 and e_2 Contours on the Back Side of the Panels from the Simulations

respectively, for (a)&(b) LVG1075 (c)&(d) LVG1074 (e)&(f) LVG1076 (g)&(h)

LVG1063
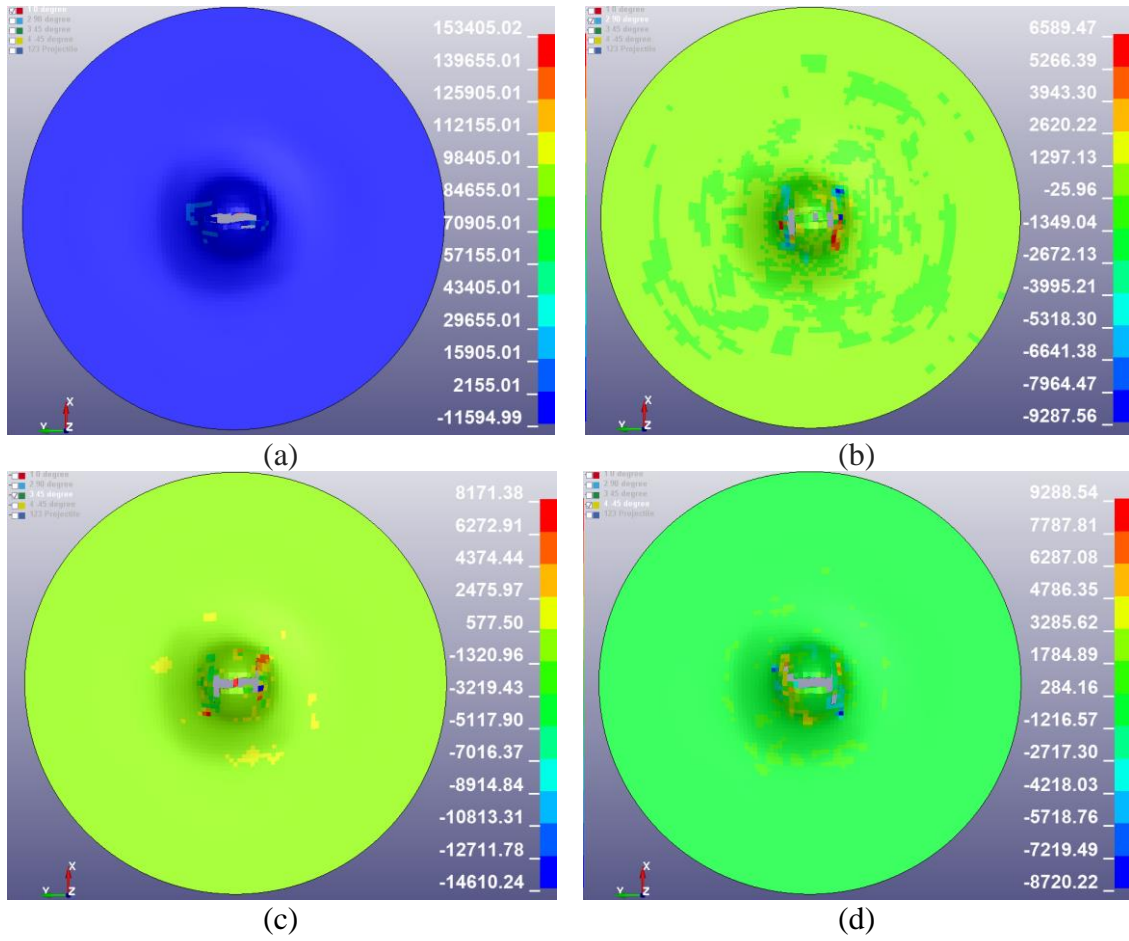
Figure 40. Shear Strain-Rate Contour in the 1-3 Plane from the LVG1075 Simulation for

(a) 0° Plies (b) 90° Plies (c) 45° Plies and (d) -45° Plies
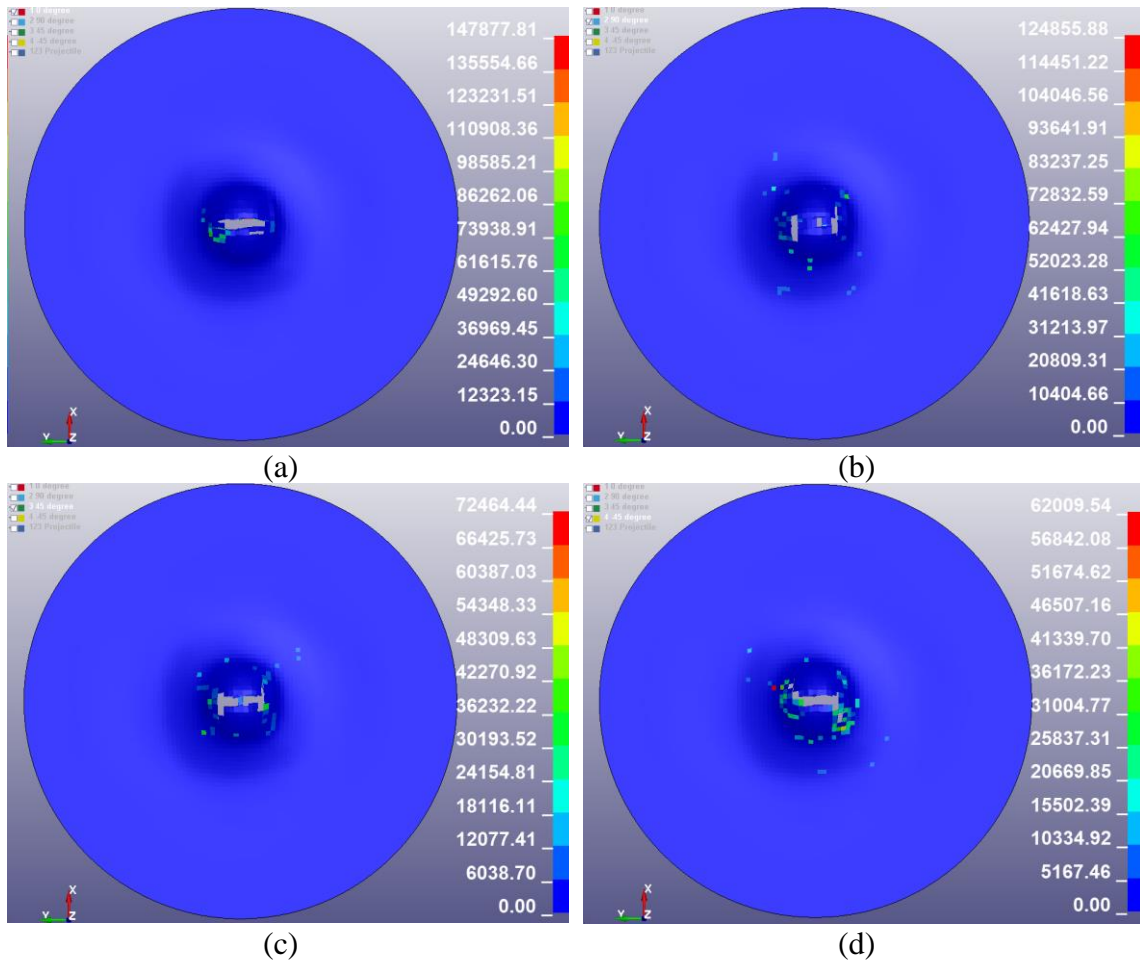
Figure 41. Plastic Multiplier Contour from the LVG1075 Simulation for (a) 0° Plies (b)

90° Plies (c) 45° Plies and (d) -45° Plies

5   CONCLUDING REMARKS

Accomplishments: The demands for accurately modeling composite structures subjected to quasi-static and especially, dynamic loading in the US aerospace industry led to the initial funding for the development of a new constitutive model in LS-DYNA in 2012. As a result, in about 8 years, good progress has been made by the FAA-NASA funded composites team. Some of the progress is as a result of the work done in this dissertation.

The following research objectives were identified at the beginning of the dissertation work.

1. Enhance OEPDMM deformation and damage sub-models to simulate rate dependent composite behavior.

2. Implement Puck Failure model and Generalized Tabulated Failure model.

3. Verify the developed capabilities via single and multiple element test cases.

4. Validate the developed capabilities using statically loaded structural test results from ASU, and impact test results from NASA-GRC.

Via the list presented below, an inventory is taken to show that the objectives have been met satisfactorily:

(1) Development of the theoretical details and implementation of visco-elastic-plastic formulation. This feature provides the capability to predict stress relaxation behavior of materials when using rate dependent input stress-strain data. Guidelines have been developed to ensure that experimental data are properly

processed for use by the algorithm. Single element verification tests have been carried out to demonstrate this feature.

(2) The algorithm involved in the computation of plastic multiplier has been upgraded with additional associated flow rule and radial return scheme. This plays a major role in avoiding error termination during a simulation caused by inability to an acceptable plastic multiplier. Furthermore, this has helped in reducing the simulation time required to complete an analysis since it has made it possible to use a larger time step without compromising on the stability and accuracy of an analysis.

(3) Other enhancements to the deformation sub-model include (i) automated modification of Poisson's ratio to ensure that orthotropic material property requirements are met, (ii) strain rate smoothing to avoid numerical instability which may arise due to sudden changes in strain rates, and (iii) modeling temperature rise in composites due to Taylor-Quinney effect.

(4) Two failure theories are now supported. The Puck Failure criteria has been adapted and implemented for use with the constitutive model. Improvements have been made to the post-peak behavior to yield a more controlled solution (Shyamsunder et al., 2020a). The new stress degradation model (Shyamsunder et al., 2020b) provides more freedom to dictate the post-peak behavior. This has resulted in an improved prediction for the staked-ply tension and compression validation tests under quasi-static loading compared to earlier results (Shyamsunder et al., 2020a). Linking the post-peak behavior to fracture energy makes the strength predictions less dependent on the finite element mesh as

evidenced from the convergence analyses. The impact test simulation required calibration of the post-peak residual damage parameters to obtain a reasonable prediction. The out-of-plane displacement is predicted very well for the first 1 ms following the impact. The rebound velocity is within 10% of the experimental result. However, the damage and crack patterns are different. The material behavior appears to be *flaky* in comparison to the test results.

(5) The Generalized Tabulated Failure model (GTFC) is a new failure criterion. It permits an arbitrary-shaped failure surface to be defined and used. In its current form, the failure surface is decomposed into in-plane and out-of-plane failure modes thereby making it suitable for modeling laminated unidirectional composites. The failure surfaces are used as an erosion criterion rather than for predicting failure onset. The post-peak behavior is predicted using the damage sub-model; stress components are degraded gradually to the respective residual strengths. The stacked-ply tension test results show the peak load to be slightly underpredicted, but the compressive test results are very close to the experimental results. Minimal calibration is done with the residual strength and equivalent failure strain values. Although, it has been found that GTFC is mesh size dependent, the strength of GTFC is demonstrated in the impact test simulation. The rebound velocity is within 10% of the experimental result. The crack pattern qualitatively matches the experimental results. The out-of-plane displacement is close to the first positive peak.

Additional four different ballistic impact test cases have been presented using GTFC with rate dependent input stress-strain curves. Out of these four, one of the tests is a contained test where the projectile does not go through the plate. A coarser mesh compared to the former impact test FE model has been used for this purpose to reduce the wall clock time of the simulation since the objective is to reduce the error in predicting the projectile exit/rebound velocity with respect to the experiment with a compromise on the predicted crack pattern. The procedure to use the stress-strain curve input available at different strain rates has been discussed in detail. The importance of carefully processing the rate dependent curves before using them as input to the material model has been highlighted. Sensitivity analysis showed that the out-of-plane residual strength plays the most significant role in the prediction of the projectile exit/rebound velocity. This has been used as the basis for calibration to obtain failure parameters which have been used uniformly for all the four test cases yielding results with reasonably good predictions. The error involved in the energy absorbed by the composite panel is less than 10% in all the four test cases, although the crack patterns could not be predicted. Further investigation into these test cases revealed that the rate involved in these test cases are extremely large compared to the rates at which the stress-strain curves have been specified. Analysis of the impact FE simulations show that the computed strain-rate values are very high (in the order of 10^3). These findings call for more rate dependent stress-strain curves to be used as input, especially in the shear components. This set of impact simulations are not carried out using PFC since the current implementation for PFC do not have the capability to incorporate rate dependent data.

Future Work: It is well understood that damage and failure of composite systems are driven by the composite architecture and the constituent materials, and that while multi-scale modeling may make the numerical model more predictive, the enormous computational expense makes this approach currently untenable. What is desirable from an analyst's viewpoint, is a reasonable and systematic approach that requires (a) input data that is largely experimental (physical and virtual) driven, (b) a small number of damage and failure-related parameters, and (c) an even smaller number of parameters that may require some tuning/calibration to yield consistent and somewhat conservative results. While the current implementation is a major improvement in capabilities to model composite structural systems, there are features that need to be developed and implemented. Some of the ongoing work as well as future work to overcome the limitations of the current implementation are discussed in the following paragraphs.

There is ample experimental evidence showing that for unidirectional carbon/epoxy composites the strength as well as the moduli in the in-plane shear and the transverse components increase with increase in strain-rate (Daniel et al., 2011). As discussed in Section 4.3.2, strain-rate values in the shear components are high in the impact simulations however, there is no shear stress-strain data available for higher rate. In such cases, synthetic stress-strain tabulated input at higher strain-rate can be used. These synthetic data can be generated using analytical expressions given in Daniel et al., 2011 (Daniel et al., 2011) as well as by using engineering judgement. In the current implementation, for a given rate and temperature, linear interpolation is carried out amongst the input stress-strain curves to obtain the moduli and the yield stress. Using a

logarithmic interpolation rather than the linear interpolation will give a more realistic values of moduli and yield stress for a given composite material into consideration involving high rate/temperature event such as an impact scenario (Park et al., 2020).

There is a need for both the PFC and the GTFC to be rate and temperature dependent. In order to make the PFC implementation rate and temperature dependent is rather straightforward; the strength parameters in the expression for IFF criteria (Eqs. 3.15 and 3.16) need to be functions of strain rate and temperature. This implies that the Master Fracture Body will change as a function of strain rate and temperature. This can be done either using an analytical expression similar to the one used in Daniel et al., 2011 (Daniel et al., 2011) for the strength values or to provide a tabulated strength values as a function of strain rate and/or temperature (Park et al., 2020). Another aspect from a modeling point of view is the mesh objectivity. The mesh size should not affect the erosion pattern of elements in an FE model. Although it has been shown using the stacked-ply static tests that PFC is mesh independent, further investigation needs to be done using impact tests with different mesh sizes. As for GTFC, even if there is a way out in using rate-dependent stress-strain curves as discussed earlier, this is not the best way since the user needs to modify the actual stress-strain input curve(s). The first step in making GTFC rate and temperature dependent is to make the damage sub-model rate and temperature dependent. This is required since GTFC relies on the damage sub-model for post-peak degradation behavior. For this purpose, the damage parameter curves - strain data set will be input into OEPDMM as a function of strain-rate and temperature. As for the element erosion criteria, this can also be input as a function of strain-rate and temperature.

117

In addition to the enhancements discussed earlier, the following features are worth exploring:

(1) The element erosion parameters can be defined as a function of the element characteristic length (Ansys-LST, 2018). In the case of GTFC, the erosion criteria (equivalent failure strain curves) can be defined as a function of the characteristic length of the elements so that the failure (erosion) is mesh size independent.

(2) Support for non-local averaging algorithm that prevents the damage/failure and crack pattern to be dependent on the mesh orientation (Forghani, 2011). In other words, the crack pattern or the damaged region should be the same in structured mesh compared to that of a non-structured mesh.

(3) Implementation of crashfront algorithm into OEPDMM would aid in simulating a crush test as evident from many of the composite material models discussed in Section 1.2.

(4) Support for implicit analysis where dynamic effects play a minor role in the behavior of the structure.

(5) Improving the computational throughput so as to cut down on the wall clock time. A second look at the overall algorithm is likely to identify computational bottlenecks.

All the proposed improvements which can be implemented in the future as well as with more experimental data at higher rate and temperature will help better predict the behavior of composites for a variety of loading condition. As one of the pioneers in composite modeling, Alfred Puck mentioned in (Knops, 2008) – "What I already know

for a long time, is: Modern composites are black and not easy to be looked through but they are not at all products of black magic! We can understand them if we carefully try to think about their internal construction. However, thinking alone is not enough, of equal importance are smart experiments."

REFERENCES

Achstetter, T. (2019). *Development of a Composite Material Shell-Element Model for Impact Applications.* Fairfax: PhD Disseration, George Mason University.

Achstetter, T., Park, C.-k., & Kan, C.-D. (2020). *Development of a tabulated material model for composite material failure, MAT213 Part 3: Implementation of probabilistic modeling capability in the tabulated composite failure model MAT213.* FAA, DOT/FAA/TC-19/50, P3.

Allen, D. H., Harris, C. E., & Groves, S. E. (1987). A thermomechanical constitutive theory for elastic compoistes with distributed damage - I. Theoretical development. *International Journal of Solids and Structures, 23*(9), 1301-1318.

Ambur, D. R., Jaunky, N., Lawson, R. E., & Knight Jr, N. F. (2001). Numerical Simulations for High-Energy Impact of Thin Plates. *Internatioan lJournal of Impact Engineering, 25*(7), 683-702.

Ansys-LST. (2018). *LS-DYNA Keyword user's Manual - Volume II Material Models.* Livermore, California: Livermore Software Technology Corporation.

Ansys-LST. (2020a). *ftp.lstc.com.* (Ansys) Retrieved September 4, 2020, from https://ftp.lstc.com/anonymous/outgoing/jday/faq/composite.models

Ansys-LST. (2020b). LS-DYNA R11.

AZO Materials. (2015). *azom.com.* Retrieved Spectember 6, 2020, from azom.com: https://www.azom.com/article.aspx?ArticleID=12194

Bazant, Z. P., & Oh, B. (1983). Crack band theory for fracture of concrete. *materials and Structures, 16*(3), 155-177.

Belyschko, T., Liu, W. K., & Moran, B. (2014). *Nonlinear finite elements for continua and structures.* Wiley.

Berstad, T., Hopperstad, O., & Langseth, M. (1994). Elasto-viscoplastic Constitutive Models in the Explicit Finite Element Code LS-DYNA3D. *Second LS-DYNA3D Conference .* San Francisco.

Bhatnagar, A. (2016). *Lightweight Ballistic Composites: Military and Law-Enforcement Applications.* London: Woodhead Publishing Series in Composites Science and Engineering.

Bogetti, T. A., Staniszewski, J., Burns, B. P., Hoppel, C. P., Gillespie Jr, J. W., & Tierney, J. (2012a). Predictign the nonlinear response and progressive failureof

composite laminates under triaxial loading: Correlation with experimental results. *Journal of Composite Materials, 47*(6-7), 793-804.

Bogetti, T. A., Staniszewski, J., Burns, B. P., Hoppel, C. P., Gillespie Jr, J. W., & Tierney, J. (2012b). Predicting the nonlinear response and progressive failure of composites laminates under tri-axial loading. *Journal of Composite Materials, 46*(19-20), 2443-2459.

Boutaous, A., Peseux, B., Gornet, L., & Belaidi, A. (2006). A new modeling of plasticity coupled with the damage and identification for carbon fiber compoiste laminates. *Composite Structures, 74*(1), 1-9.

Camanho, P. P. (2002). *web.fe.up.pt.* Retrieved December 13, 2018, from https://web.fe.up.pt/~stpinho/teaching/feup/y0506/fcriteria.pdf

Carrere, N., Laurin, F., & Maire, J.-F. (2012a). Micromechanical-based hybrid mesoscopic three-dimensional aproach for non-linear progressive failure analysis of composite structures-Part B: Comparison with experimental data. *Journal of Composite Materials, 47*(6-7), 743-762.

Carrere, N., Laurin, F., & Maire, J.-F. (2012b). Micromechanical-based hybrid mesoscopic 3D approach for non-linear progressive failure analysis of composite structures. *Journal of Composite Materials, 46*(19-20), 2389-2415.

Chang, F., & Chang, K. (1987a). Post-Failure Analysis of Bolted Compoistes Joints in Tension or SHear-out Mode Failure. *Journal of Composite Materials, 21*, 809-823.

Chang, F., & Chang, K. (1987b). A Progressive Dmage Model for Laminated Composites Containing Stress Concentration. *Journal of Composite Materials, 21*(9), 834-855.

Chen, H.-S., & Hwang, S.-F. (2009). A fatigue damage model for composite materials. *Polymer Compoistes, 30*(3), 301-308.

Chen, X. (2016). *Advanced Fibrous Compoiste Materials for Ballistic Protection.* London: Woodhead Publishing Series in Composites Science and Engineering.

Christensen, R., & Lonkar, K. (2016). *www.failurecriteria.com/.* Retrieved December 13, 2018, from https://www.failurecriteria.com/Media/First_Ply_Failure.pdf

Cuntze, R. (2012a). Comparison between experimental and theoretical results using Cuntze's "failure mode concept" model for composites under triaxial loadings-Part B of the second world-wide failure exercise. *Journal of Composite Materials, 47*(6-7), 893-924.

Cuntze, R. (2012b). The predictive capability of failure mode concept-based strength conditions for laminates composed of unidirectional laminae under static triaxial stress states. *Journal of Composite Materials, 46*(19-20), 2563-2594.

Daniel , I. M., Werner, B. T., & Fenner, J. S. (2011). Strain-rate-dependent failure criteria for composites. *Composites Science and Technology, 71*(3), 357-364.

Deshpande, Y., Yang, P., Seidt, J., & Gilat, A. (2019). Dynamic Mechanical Response of T800/F3900 Composite under Tensile and Compressive Loading. *Proceedings of the 2019 Annual Conference and Exposition on Experimental and Applied Mechanics.* Reno, NV.

Deuschle, H. M., & Kroplin, B.-H. (2012). Finite element implementation of Puck's failure theory for fiber-reinforced composites under three-dimensional stress. *Journal of Composite Materials, 46*(19-20), 2485-2513.

Deuschle, H. M., & Puck, A. (2012). Application of the Puck failure theory for fiber-reinforced composites under three-dimensional stress: Comparison with experimental results. *Journal of Composite Materials, 47*(6-7), 827-846.

Deushle, H. M. (2010). *3D Failure Analysis of UD Fiber Reinforced Composites: Puck's Theory within FEA.* PhD Disseration, Institute of Statics and Dynamics of Aerospace Structures, University of Stuttgart.

Doudican, B. M., Zand, B., Amaya, P., Butalia, T. S., Wolfe, W. E., & Schoeppner, G. A. (2012). Strain energy based failure criterion: Comparison of numerical predictions and experimnetal observations for symmetric composite laminates subjected to triaxial loading. *Journal of Composite Materials, 47*(6-7), 847-866.

DuBois, P., Feucht, M., Irsingler, J., & Erhart, T. (2017). Implementation of a VE-VP Material Law for the Simulation of Energy Absorbing Thermoplastic Components. *Eleventh European LS-DYNA Conference .* Salzburg.

Farren, W., & Taylor, G. (1925). The heat developed during plastic extension of metals. *Proceedings of The Royal Society A.* London, U.K.

Forghani, A. (2011). *A Non-local Approach to Simulation of Damage in Compoiste Structures.* Vancouver: PhD Disseration, The University of British Columbia.

Goldberg, R., Carney, K., DuBois, P., Hoffarth, C., Harrington, J., Rajan, S., & Blankenhorn, G. (2016). Development of an Orthotrpic Elasto-Plastic Generalized Composite Material Model Suitable for Impact Problems. *Journal of Aerospace Engineering, ASCE, 29*(4).

Goldberg, R., Carney, K., DuBois, P., Hoffarth, C., Khaled, B., Rajan, S., & Blankenhorn, G. (2018a). Analysis and Characterization of Damage Using a Generalized Composite Material Model Suitable for Impact Problems. *ASCE Journal of Aerospace Engineering*, DOI:10.1061/(ASCE)AS.1943-5525.0000854.

Goldberg, R., Carney, K., DuBois, P., Hoffarth, C., Khaled, B., Shyamsunder, L., . . . Blankenhorn, G. (2018b). Implementation of a Tabulated Failure Model into a Generalized Composite Material Model. *Journal of Composite Materials, 52*(25), 3445-3460.

Griffin, O. H., Kamat, M. P., & herakovich, C. T. (1981). Three-dimensional inelastic fninte element analysis of laminated composites. *Journal of Compoiste Materials, 15*, 543-560.

Harrington, J., Hoffarth, C., Rajan, S., Goldberg, R. K., Carney, K. S., DuBois, P., & Blankenhron, G. (2017). Using Virtual Tests to Complete the Description of a Three-Dimensional Orthotropic Material. *ASCE Journal of Aerospace Engineering*, DOI:10.1061/(ASCE)AS.1943-5525.0000737.

Hashin, Z. (1980). Failure Criteria for Unidirectional Fiber Composites. *Journal of Applied Mechanics, 47* (2), 329-334.

Hinton, M. (2011). Failure Criteria in Fiber Reinforced polymer Composites: Can any of the Predictive Theories be Trusted? *NAFEMS World Congress, 23rd-26th May.* Boston.

Hinton, M., Kaddour, A., & Soden, P. (2004). The world-wide failure exercise: Its origin, concept and content. In M. Hinton, A. Kaddour, & P. Soden, *Failure Criteria in Fibre Reinforced Polymer Composites: TheWorld-WideFailure Exercise* (pp. 2-28). Amsterdam: Elsevier.

Hoffarth, C. (2016). *A Generalized Orthotropic Elasto-Plastic Material Model for Impact Analysis.* Tempe, AZ. USA: PhD Dissertation, Arizona State university.

Hoffarth, C., Khaled, B., Shyamsunder, L., & Rajan, S. (2020). *Development of a Tabulated Material Model for COmposite Material Failure, MAT213, Part 1: Theory, Implementation, Verification & Validation.* FAA, DOT/FAA/TC-19/50, P1.

Hoffarth, C., Khaled, B., Shyamsunder, L., Rajan, S., Goldberg, R., Carney, K., . . . Blankenhorn, G. (2017). Verification and Validation of a Three-Dimensional Orthotropic Plasticity Constitutive Model Using a Unidirectional Composite. *Fibers, 5*(1), 1-13.

Hoffarth, C., Rajan, S., Goldberg, R., Revilock, D., Carney, K., DuBois, P., & Blankenhorn, G. (2016). Implementation and Validation of a Three-Dimensional Plasticity-Based Deformation Model for Orthotropic Composites. *Composites: A*, 336-350.

Holt, N. (2018). *Experimental and Simulation Validation Tests for MAT213.* Tempe: MS Thesis, School of Sustainable Engineering and the Built Environment, Arizona State University.

Huang, Y., Jin, C., & Ha, S. K. (2012a). Strength prediction of triaxially loaded composites usign a progressive damage model based on micromechanics of failure. *Journal of Composite Materials, 47*(6-7), 777-792.

Huang, Y., Xu, L., & Ha, S. K. (2012b). Prediction of three-dimensional composite laminate response using micromechanics of failure. *Journal of Composite Materials, 46*(19-20), 2431-2442.

Jelf, P., & Fleck, N. (1992). Compression Failure mechanisms in Unidirectional Composites. *Journal of Composite Materials, 26*(18), 2706-2726.

Johnston, J., Pereira, J., Ruggeri, C., & Roberts, G. (2017). High Speed Thermal Imaging on Ballistic Impact of Triaxially Braided Composites. *ASC 32nd Technical Conference.* West Lafayette.

Johnston, J., Pereira, J., Ruggeri, C., & Roberts, G. (2018). High-speed infrared thermal imaging during ballistic impact of triaxially braided composites. *Journal of Compoiste Materials, 52*(25), 3549-3562.

Kaddour, A., & Hinton, M. (2012). Benchmarking of Triaxial Failure Criteria for Composite Laminates: Comparison between models of "Part (A)' of 'WWFE-II'. *Journal of Composite Materials, 46*(19-20), 2593-2632.

Kaddour, A., & Hinton, M. (2018). Failure Cirteria for Composites, Refernece Module in Materials Sicence and Materials Engineering. Elsevier.

Kaddour, A., Hinton, M., Smith, P., & Li, S. (2013). The background to the third world-wide failure exercise. *Journal of Composite Materials, 47*(20-21), 2417-2426.

Khaled, B., Shyamsunder, L., Hoffarth, C., Rajan, S., Goldberg, R., Carney, K., . . . Blankenhorn, G. (2017). Experimental Characterization of Composites to Support an Orthotropic Plasticity Material Model. *Journal of Composite Materials*, DOI: 10.1177/0021998317733319.

Khaled, B., Shyamsunder, L., Hoffarth, C., Rajan, S., Goldberg, R., Carney, K., . . . Blankenhorn, G. (2018). Damage Characterization of Composites to Support an Orthotropic Plasticity Model. *Journal of Composite Materials, 53*(7), 941-967.

Khaled, B., Shyamsunder, L., Holt, N., Hoover, C., Rajan, S., & Blankenhorn, G. (2019). Enhancing the Predictive Capabilities of a Composite Plasticity Model using Cohesive Zone Modeling. *Composites Part A, 121*, 1-17.

Khaled, B., Shyamsunder, L., Schmidt, N., Hoffarth, C., & Rajan, S. (2020). *Development of a Tabulated material Model for Composite Material Failure, MAT213 Part 2: Experimental Tests to Characterize the behavior and Properties of T800-F3900 Today Composite* . Technical Report DOT/FAA/TC-19/50, P2.

Knass, W. G., & Gonzalez, L. (2001). *Global Failure Modes in Composite Structures.* NASA Grant NAG 1-1975.

Knops, M. (2008). *Analysis of Failure in Fiber Polymer Laminates - The Theory of Alfred Puck.* New York: Springer.

Kodagali, K., Tessema, A., & Kidane, A. (2017). Progressive failure analysis of a composite lamina using Puck Failure Criteria. *Thirty-Second Technical Conference, American Society for Composites.* West Lafayette, Indiana.

Konieczny, M. J. (2018). *Full-field strain and temperature measurement of epoxy residn PR-520 subjected to tensile loading at various strain rates.* Undergraduate Honors Thesis, The Ohio State University.

Lempriere, B. M. (1968). Poisson's Ratio in Orthotropic Materials. *American Institute of Aeronautics and Astronautics, 6*(11), 2226-2227.

Maimi, P., Camanho, P., Mayugo, J., & Davila, C. (2007a). A continuum damage model for composite laminates: Part I - Constitutive model. *Mechanics of Materials, 39*(10), 897-908.

Maimi, P., Camanho, P., Mayugo, J., & Davila, C. (2007b). A continuum damage model for composite laminates: Part II- Computational implementation and validation. *Mechanics of Materials, 39*(10), 909-919.

Matzenmiller, A., Lubliner, J., & Taylor, R. L. (1995). A Constitutive model for Anisotropic Damage in Fiber-Composites. *Mechanics of Materials, 20*, 125-152.

Melis, M., Pereira, M. J., Goldberg, R., & Rassaian, M. (2018). Dynamic Impact Testing and Model Development in Support of NASA's Advanced Compoistes Program. *AIAA Scitech Conference.* Kissimmee, FL.

Notta-Cuvier, D., Lauro, F., & Bennani, B. (2014). An original approach for mechanical modeling of short-fiber reinforced compoistes with complex distribution of fiber orientation. *Composites Part A, 62*, 60-66.

Park, C.-K., Kelly, C., DuBois, P., Cordasco, D., & Kan, C.-D. (2020). *Aluminum 2024-T351 Input Parameters for *MAT_224 in LS-DYNA*. FAA, DOT/FAA/TC-19/41, P1.

Petit, P. H., & Waddoups, M. E. (1969). A method of predicting the nonlinear behavior of laminated composites. *Journal of Composite Materials, 3*, 2-19.

Pindera, M. J., & Herakovich, C. T. (1983). An endochronic model for the response of unidirectional compoistes under off-axis tensile load. In: Hashin Z, Herakovich CT, editors. Mechanics of Composite Materials: Recent Advances, Proceedings IUTAM symposium of Mechanics of Composite Materials. . 367-381. Pergamon press.

Pinho, S., Darvizeh, R., Robinson, P., Schuecker, C., & Camanho, P. (2012). Material and structural response of polymer-matrix fiber-reinforced composites. *Journal of Composite Materials, 46*(19-20), 2313-2341.

Pinho, S., Iannucci, L., & Robinson, P. (2006a). Physically-based failure models and criteria for laminated fibre-reinforced composites with emphasis on fibre kinking: Part I: Development. *Composites Part A Applied Science and Manufacturing, 37*(1), 63-73.

Pinho, S., Iannucci, L., & Robinson, P. (2006b). Physically based failure models and criteria for laminated fibre-reinforced composites with emphasis on fibre kinking. Part II: FE implementation. *Composites Part A Applied Science and Manufacturing, 37*(5), 766-777.

Pinho, S., Robinson, P., & Iannucci, L. (2006c). Fracture Toughness of the Tensile and Compressive Fiber Failure Modes in Laminated Composites. *COmposite Science and Technology, 66*(13), 2069-2079.

Pinho, S., Vyas, G., & Robinson, P. (2013). Material and structural response of polymer-matrix fiber-reinforced composites: Part B. *Journal of Composite Materials, 47*(6-7), 679-696.

Puck, A., Kopp, J., & Knops, M. (2002). Cuidelines for the determination of the Parameters in Puck's Action Plane Strength Criterion. *Composite Science and Technology, 62*(3), 371-378.

Rajan, V. P., Shaw, J. H., Rossol, M. N., & Zok, F. W. (2014). An elastic-plastic constitutive model for ceramic composite laminates. *Composites Part A, 66*, 44-57.

Roberts, G. D., Revilock, D. M., Binienda, W. K., Nie, W. Z., Mackenzie, S. B., & Todd, K. B. (2002). *Impact Testing and Analysis of Composites for Aircraft Engine Fan Cases.* NASA/TM-2002-211493.

Rossi, T. A., Fayazbakhsh, K., & Fawaz, Z. (2020). Application of LS-DYNA Constitutive Material Model Laws to Simulate Low Velocity Impact Damage to Composite Plates. *ASCE Journal of Aerospace Engineering, 33*(6), DOI: 10.1061/(ASCE)AS.1943-5525.0001171.

Schweizerhof, K., Weimar, K., Munz, T., & Rottner, T. (1998). Crashworthiness Analysis with Enhanced Composite Material Models in LS-DYNA - Merits and Limits. *Fifth international LS-DYNA User's Conference.* Southfield, Michigan.

Shyamsunder, L., Khaled, B., & Rajan, S. (October 23, 2019). MAT-213 V1.3.5 Status. Tempe, Arizona: FAA Research Project Monthly Telecoference.

Shyamsunder, L., Khaled, B., Rajan, Rajan, S., Goldberg, R., Carney, K., . . . Blankenhorn, G. (2020a). Implementing Deformation, Damage and Failure in an Orthotropic Plastic Material Model. *Journal of Compoiste Materials, 54*(4), 463-484.

Shyamsunder, L., Khaled, B., Rajan, S., & Blankenhorn, G. (2020b). Improving Failure Sub-moldes in an Orthotropic Plasticity-based Material Model. *Submitted to Journal of Composite Materials*.

Stahlecker, Z. K., Mobasher, B., Rajan, S., & Pereira, M. J. (2009). Development of Reliable Modeling Methodologies for Engine Fan Blade Out Containment Analysis. Part II: Finite Element Analysis. *International Journal of Impact Engineering, 36*(3), 447-459.

Sun, C. T., & Chen, J. L. (1989). A simple flow rule for characterizing nonlinear behavior of fiber compoistes. *Journal of Composite Materials, 23*, 1009-1020.

Sun, C. T., Quinn, B. J., Tao, J., & Oplinger, D. W. (1996). *Comparative Evaluation of Failure Analysis Methods for Composite Laminates.* FAA, DOT/FAA/AR-95/109.

Taylor, G., & Quinney, H. (1934). The latent energy remaining in ametal after cold working. *Proceedings of The Royal Society A*. London.

Toray Carbon Fibers America. (2020). *www.toraycma.com*. Retrieved March 23, 2020.

Tsai, S., & Wu, E. (1971). A General Theory of Strength for Anisotropic Materials. *Jourmal of Composite Materials, 5*(1), 58-80.

Vaziri, R., Olson, M. D., & Anderson, D. L. (1991). Plasticity-based constitutive Model for fiber-reinforced compoiste laminates. *Journal of Composite Materials, 25*, 512-535.

Wang, W. M., Sluys, L. J., & Borst, R. D. (1997). Viscoplasticity for Instabilities due to Strain Softening and Strain-Rate Softening. *International Journal for Numerical Methods in Engineering, 40*, 3839-3864.

Wu, F., & Yao, W. (2010). A fatigue damage model of composite materials. *International Journal of Fatigue, 32*, 134-138.

Xiao, X. (2009). Modeling energy absorbtion with a damage mechanics based compoiste material model. *Journal of Composite Material, 43*(5), 427-444.

Yen, C. F. (2002). Ballistic Impact Modeling of Composite Materials. *Seventh International LS-DYNA users Conference.* Dearborn, MI.

Zand, B., Butalia, T. S., Wolfe, W. E., & Schoeppner, G. A. (2012). A Strain Energy based Failure Criterion for Nonlinear Analysis of Composite Laminates subjected to Triaxial Loading. *Journal of Composite Materials, 46*(19-20), 2515-2537.

Zhou, Y.-X., & Huang, Z.-M. (2012a). A bridging model prediction of the ultimate strength of composite laminates subjected to triaxial loads. *Journal of Composite Materials, 46*(19-20), 2343-2378.

Zhou, Y.-X., & Huang, Z.-M. (2012b). Correlation of the bridging model predictions for triaxial failure strengths of composites with experiments. *Journal of Composite Materials, 47*(6-7), 697-731.